3-21-2013

Metamaterial Structure Design Optimization: A Study of the Cylindrical Cloak

Jason V. Paul

Follow this and additional works at: https://scholar.afit.edu/etd

Part of the Electrical and Computer Engineering Commons, and the Other Materials Science and Engineering Commons

METAMATERIAL STRUCTURE DESIGN OPTIMIZATION: A STUDY OF THE

CYLINDRICAL CLOAK

DISSERTATION

Jason V. Paul, Maj, USAF

AFIT-ENG-DS-13-M-04

DEPARTMENT OF THE AIR FORCE
AIR UNIVERSITY

AIR FORCE INSTITUTE OF TECHNOLOGY

Wright-Patterson Air Force Base, Ohio

METAMATERIAL STRUCTURE DESIGN OPTIMIZATION: A STUDY OF THE

CYLINDRICAL CLOAK

DISSERTATION

Presented to the Faculty

Graduate School of Engineering and Management

Air Force Institute of Technology

Air University

Air Education and Training Command

in Partial Fulfillment of the Requirements for the

Degree of Doctor of Philosophy

Jason V. Paul, B.E.E.E. , M.S.E.E

Maj, USAF

March 2013
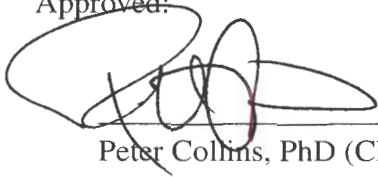
AFIT-ENG-DS-13-M-04

METAMATERIAL STRUCTURE DESIGN OPTIMIZATION: A STUDY OF THE CYLINDRICAL CLOAK

Jason V. Paul, B.E.E.E. , M.S.E.E
Maj, USAF

Approved:

_____

Peter Collins, PhD (Chairman)

25 FEB 2013

Date

_____

William Baker, PhD (Member)

25 Feb 2013

Date

_____

Ronald Coutu, Jr., PhD (Member)

25 Feb 13

Date

Accepted:

_____

Heidi R. Ries
Interim Dean, Graduate School of Engineering and Management

7 Mar 2013

Date

Abstract

Previously, Transformational Optics (TO) has been used as a foundation for designing cylindrical cloaks. The TO method uses a coordinate transform to dictate an anisotropic material parameter gradient in a cylinder coating that guides waves around the cylinder to reduce the Radar Cross Section (RCS). The problem is that the material parameters required for the TO cloak are not physically realizable and thus must be approximated. This problem is compounded by the fact that any approximation deviates from the ideal design and will allow fields to penetrate the cloak layer and interact with the object to be cloaked. Since the TO method does not account for this interaction, approximating the ideal TO parameters is doomed to suboptimal results.

However, through the use of a Green's function, an optimized isotropic cloaked cylinder can be designed in which all of the physics are accounted for. If the contribution due to the scatterer is 0, then the observer, regardless of position, will only observe the contribution due to the source and thus the object is cloaked from observation. The contribution due to the scatterer is then used as a cost functional with an optimization algorithm to find the optimal parameters of an isotropic cloaked cylinder. Although the material parameters in this design method can be fulfilled by any material, metamaterials are used to study their viability and assumptions in this application. This process culminates in the design, fabrication and measurements of a cloaked cylinder made of metamaterials that operate outside of their resonant bands. We show bistatic RCS reduction for nearly every angle along with monostatic RCS reduction for nearly every frequency in the range of 5GHz-15GHz. Most importantly, the experimental results validate the use of a Green's function based design approach and the implementation of metamaterials for normally incident energy.

Acknowledgments

To my advisor, Dr. Collins, thank you for the endless source of guidance and encouragement when things looked bleak - at least from my perspective. And to the committee members, thank you for lending your knowledge, wisdom and time to guide me along this path. I also want to recognize my fellow students, from which came insightful conversations and distraction when needed.

To all of you, this effort could not have been accomplished without you and you have my sincerest gratitude.

Jason V. Paul

Table of Contents

List of Figures

List of Tables

List of Abbreviations

METAMATERIAL STRUCTURE DESIGN OPTIMIZATION: A STUDY OF THE CYLINDRICAL CLOAK

I. Introduction

Since the advent of radar systems in WWII, engineers have sought ways to reduce an object's radar signature. This measure of an object's radar signature is referred to as its Radar Cross Section (RCS) which provides a metric to describe the amount of energy reflected from an object for a given incident and reflection angle. But before one can begin to reduce the RCS of an object, some knowledge of radar systems is needed.

The most common type of radar is a monostatic radar. The monostatic design has a colocated emitter and receiver. This type of radar is only capable of measuring the energy reflected directly back to the radar which is called the backscatter of an object. A bistatic radar is where the emitter and receiver are in separate locations and therefore is not limited to just the backscatter. This is illustrated in Figure 1.1. It is evident that the bistatic radar poses a much greater threat since it is typically not known *a priori* where the receiver is and therefore which angles of reflection will be the greatest threat.

In order to effectively reduce the RCS of an object, one must first make the assumption of the type of radar system. If the radar system is monostatic, then one is concerned with minimizing the backscatter of high risk incident angles. However, if the radar is a bistatic system, one is concerned with minimizing the reflection in every direction. Most efforts in RCS reduction assume a monostatic radar, and since most radar systems are this type, it is a valid assumption with the added bonus of simplifying the problem [11].
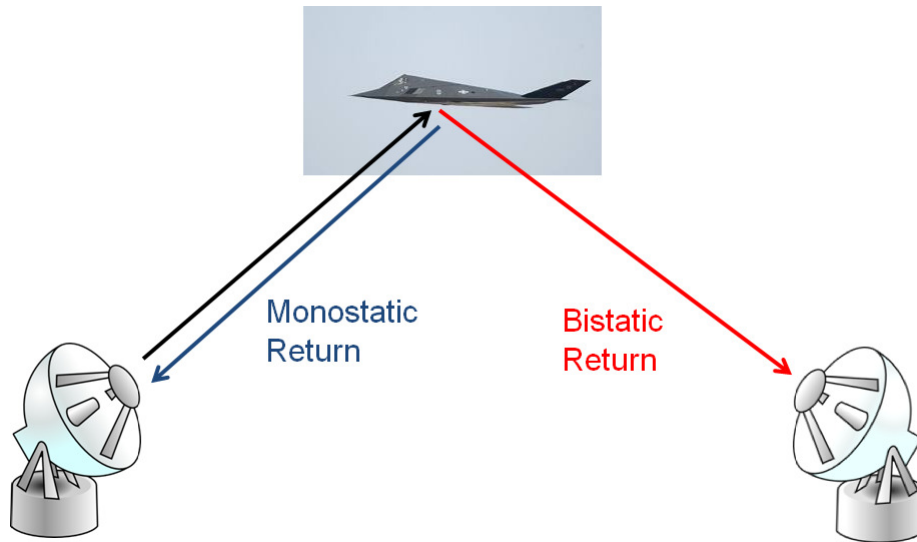
Figure 1.1: Monostatic and Bistatic Radar Setup

The most common passive RCS reduction techniques consist of shaping and using Radar Absorbing Material (RAM). While both of these techniques reduce RCS, they do so in different ways and are typically used in conjunction to mitigate the weaknesses of each other.

Shaping seeks to deflect the radar waves in a direction other than toward the receiver, thus depriving a monostatic radar of reflected energy. Surfaces perpendicular to a monostatic radar are replaced with angled surfaces to deflect the energy. This creates a tradeoff; a reduction in RCS for one incident angle comes with an increase at another incident angle. Due to this fact, RCS can only be reduced for certain incident angles. One must prioritize which incident angles to optimize while weighing the cost to other incident angles. Another consideration to shaping is how it will affect the operation of the object. For example, any change in the shape of an aircraft could affect flight characteristics, payload capacity or structural integrity. All of these factors must be taken into consideration when shaping is applied to fulfill the requirements of a system.

Since shaping can only reduce the RCS for certain angles, RAM is added to augment and mitigate the weaknesses of shaping alone. RAM absorbs incident radar energy and thereby attenuates any reflection. The absorption is due to the fact that RAM is made of lossy material. This loss transforms the incident energy into heat. Particles of iron compounds are sometimes added to a lossless matrix material to increase or customize loss. These suspensions can be sprayed onto a surface until the desired thickness is reached. However, there are some challenges with the use of RAM. While spraying RAM allows deposition into small areas that would not otherwise be coated, it is difficult to get homogeneous coverage with respect to the particle distribution and consistent thickness [11]. These coatings also create maintenance issues. These surfaces must be analyzed periodically with special equipment to insure the integrity of the RAM. Like shaping, RAM can also affect the operation of a system due to its weight. While thicker RAM does decrease RCS more, the weight can affect payload and flight characteristics.

1.1   Problem Statement

Even working in conjunction, shaping and RAM do not represent a comprehensive, all-angle solution to RCS reduction which is needed for the bistatic radar threat. However, recent advances in cloaking hold promise as a comprehensive solution for RCS reduction. The mechanism by which cloaking reduces RCS is completely different than the previously mentioned methods. Where shaping and RAM attempt to deflect and absorb radar energy, the purpose of the cloak is simply to guide incident energy, regardless of incident angle, around the object in question without disturbing the fields outside of the cloak. Like most implementations of RAM, the cloak is made of multiple layers of materials that are applied to an object. An ideal cloak will not perturb the fields outside the cloak so an observer will not detect any scattering from the cloaked object. Most importantly, cloaking could provide effective RCS reduction for both monostatic and bistatic radar.

As will be discussed at length in Chapter 2, Transformational Optics (TO) is used as a foundation for designing cylindrical cloaks. TO uses a coordinate transform to dictate an anisotropic material parameter gradient in a cylinder coating that guides waves around the cylinder to reduce the Radar Cross Section (RCS). The problem is that the material parameters required for the TO cloak are not physically realizable and thus must be approximated. This problem is compounded by the fact that any approximation deviates from the ideal design and will allow fields to penetrate the cloak layer and interact with the object to be cloaked. Since the TO method does not account for this interaction, approximating the ideal TO parameters is doomed to sub-optimal results.

This deficiency in a valid design process, in which all of the physics of the problem are taken into account to render an optimal cloaked cylinder, is the problem this effort addresses.

1.2 Research Goals and Assumptions

1.2.1 Goals.

The purpose of this research is to investigate and create a design process that will bridge the gap between the theoretical cloak and a manufacturable one. This research can be divided in to three main areas that will work together and provide a path to an optimal physical cloak.

First, we wish to derive a general cost function that will describe cloaking effectiveness for a given set of material parameters. There is currently no general expression that provides a measure of cloaking effectiveness for a given stratification profile. This portion of research centers around extracting the contribution due to the scatterer from a Green's function to be used as a cost function and exploiting recursive boundary conditions to create a general expression for an n-layered cylindrical cloak.

The second area of research is to implement this cost function with an optimization algorithm to explore the effectiveness of an isotropic cloak. This cost function will allow

the study of isotropic cloaks with large numbers of layers and variable layer thicknesses. This research will also serve as validation of the cost function.

The purpose of the third and last area of research is to implement the framework of the previous two sections in an effort to design and fabricate a physical cloak. The cost function will be used to optimize a cloak over a set of manufacturable material parameters provided by a metamaterial design process. Design verification is performed through computer simulation and experimental measurements in AFIT's indoor radar range.

1.2.2 Assumptions.

The cloaked cylinder design in this dissertation assumes normal plane wave TE_z incidence. Also, the first two research goals use a 2D model which implies a cylinder of infinite height and therefore edge effects of a cloaked cylinder of finite height are not addressed in the optimization process but may affect the measurements of the 3D structure. Furthermore, it is assumed the metamaterials used in the cylindrical cloak can fulfill the isotropic requirements of the optimization process. This is not exactly true and the validity of this assumption will be examined in Chapter 7.

1.3 Dissertation Organization

This dissertation is organized as follows. Chapter 2 and Chapter 3 cover the background of cylindrical cloaks and metamaterials respectively. Chapter 4 presents the derivation of a general cost function for optimizing cloaking effectiveness from a Green's function of an n-layered cylinder. Chapter 5 details the process of applying an optimization algorithm to the cost function to determine material parameter requirements for optimal cloaking. These efforts culminate with the design and fabrication of a metamaterial based cylindrical cloak presented in Chapter 6. The experimental measurements of this cloaked cylinder are presented in Chapter 7. Lastly, Chapter 8 concludes this dissertation with a summary of research contributions and thoughts for future research.

II. Cylindrical Cloak Background

Since TO was introduced in 1996 by Ward and Pendry [48], new structures have been imagined and designed to control electromagnetic fields. The TO method exploits the fact that Maxwell's equations are coordinate system invariant and simply amount to spatial restrictions on the fields [30]. However, the constitutive relations, which describe the interaction between the fields and a material, do not exhibit coordinate system invariance [30]. Ward and Pendry showed that transforming Maxwell's equations between coordinate systems can be manifested as an auxiliary material [48].

TO was initially developed to simplify computer programs that dealt with many coordinate systems but was later seen as a tool to force fields in a desired configuration. One can control the flow of the electromagnetic fields simply by warping the coordinate system. This new warped coordinate system is then manifested in material parameter requirements that are anisotropic and spatially varying. This method allows for theoretical insight into the control of fields but is not hospitable to physically realizing a design.

One such TO design is that of the cylindrical cloak introduced in 2006 by Pendry *et al* [28] and built the same year by Schurig *et al* [36]. In these efforts, the coordinate system is manipulated such that the cylinder is no longer part of the coordinate system and the incident fields flow around the cylinder as if it were not present. However, the coordinate transform process created a cloak material layer which is not manufacturable due, in part, to the spatially varying material parameter requirements. Additionally, the material parameters at the cylinder-cloak interface took on values of either 0 or ∞. These manufacturing challenges precipitated the need to approximate the ideal case.

In this chapter, we examine the formulation of the TO cloak material requirements and the research efforts aimed at approximating these requirements to create a more physically realizable set of material parameters.

2.1 TO Cylindrical Cloak

Originally, TO was conceived in an effort to avoid rewriting computer code when a change in the coordinate system occurred. In [48], Ward and Pendry showed that using a general coordinate transformation in Maxwell's equations equated to renormalizing the material parameters of the space in question. This meant that code could be written assuming Cartesian coordinates but could handle any coordinate system with a simple change to ϵ and μ. In this section, we show how the method in [48] can be used to design a cylindrical cloak. This method for designing a cylindrical cloak was first presented in 2006 by Pendry *et al* [28], later confirmed through computer simulation [8] and ray tracing [38]. This cloak design was also built that same year by Schurig *et al* [36].

2.1.1 TO Material Parameters.

The TO method to designing a cloak consists of deforming the coordinate system such that the origin point is expanded into a boundary around an area to be excluded from the coordinate system. In the case of the 2D cylindrical cloak, the origin is transformed into a circle such that the origin of the new coordinate system is the line bounding the circle and the area within the circle is not part of the new coordinate system. Since this area is not part of the new coordinate system, the fields will be forced to move around the area and therefore cloak any object contained within the area. This void in the coordinate system is sometimes referred to as the hidden region. For the cylindrical cloak, we wish to make this void area the size of our (PEC) cylinder but we also want to constrain the new warped coordinate system to limit the size of the required material with renormalized parameters. This material that is required by the coordinate transform is manifested as a coating around our PEC cylinder. Beginning with the warped coordinate transform, we use the equations from [30] to generate the material parameters required. The relevant geometry can be seen in Figure 2.1. Throughout this dissertation, the geometry consists of $a = 1\lambda$ and $b = 2\lambda$ unless otherwise specified.

7
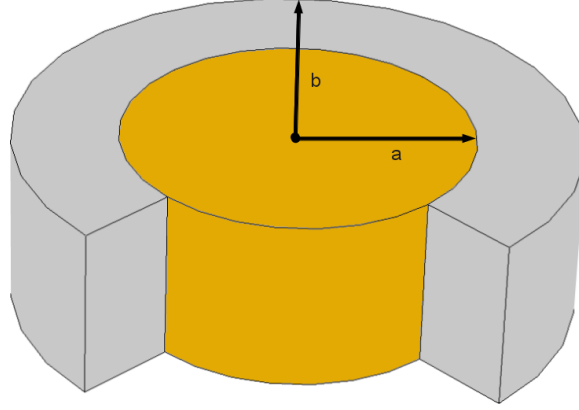
Figure 2.1: Cylindrical Cloak Geometry

The transform used in [36] to compress the coordinates within the cylinder into a layer surrounding the cylinder is

$$
\begin{aligned}
\rho' &= \frac{b-a}{b}\rho + a \\
\theta' &= \theta \\
z' &= z
\end{aligned}
\tag{2.1}
$$

where the $'$ denotes the new warped coordinates. A visual representation of the warping of the cylindrical coordinate system can be seen in Figure 2.2.

Next, since the TO method assumes a starting point of the Cartesian coordinates, the Cartesian coordinates can be expressed as cylindrical coordinates by Equation 2.2.

$$
\begin{aligned}
x &= \rho \cos\theta \\
y &= \rho \sin\theta \\
z &= z
\end{aligned}
\tag{2.2}
$$
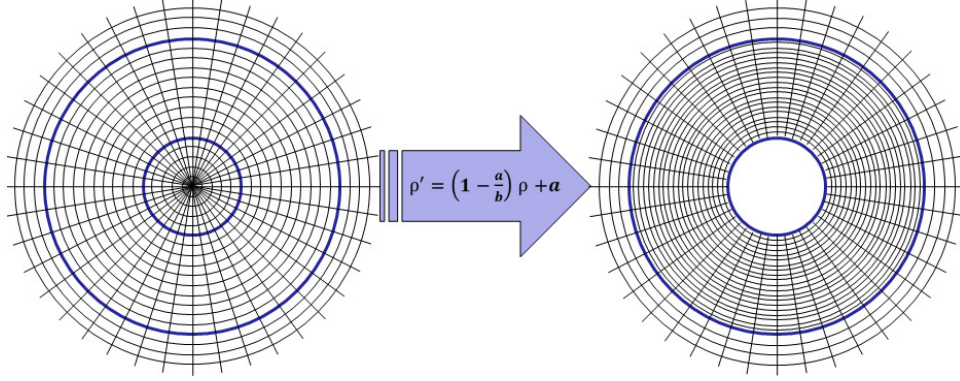
Figure 2.2: Graphical representation of the coordinate transform for a cylindrical cloak

Substituting Equation 2.1 into 2.2 we can express the transform from Cartesian coordinates to the new warped cylindrical coordinates as Equation 2.3.

$$
\begin{aligned}
x &= \frac{\rho' - a}{b - a} b \cos \theta' \\
y &= \frac{\rho' - a}{b - a} b \sin \theta' \\
z &= z'
\end{aligned}
\tag{2.3}
$$

Lastly, from [30], Equation 2.4 is used to apply the coordinate transform to transform the starting material (free space) to the material parameters that will force the fields into the required configuration.

$$
\left\{ \begin{array}{c} \epsilon' \\ \mu' \end{array} \right\} = \left| J^{-1} \right| J J^T \left\{ \begin{array}{c} \epsilon \\ \mu \end{array} \right\}
\tag{2.4}
$$

This formulation uses the Jacobian transformation matrices as seen in Equation 2.5,

9

$$J = \begin{bmatrix} \frac{\partial \rho'}{\partial x} & \frac{\partial \rho'}{\partial y} & \frac{\partial \rho'}{\partial z} \\[6pt] \frac{\partial \theta'}{\partial x} & \frac{\partial \theta'}{\partial y} & \frac{\partial \theta'}{\partial z} \\[6pt] \frac{\partial z'}{\partial x} & \frac{\partial z'}{\partial y} & \frac{\partial z'}{\partial z} \end{bmatrix} \qquad J^{-1} = \begin{bmatrix} \frac{\partial x}{\partial \rho'} & \frac{\partial x}{\partial \theta'} & \frac{\partial x}{\partial z'} \\[6pt] \frac{\partial y}{\partial \rho'} & \frac{\partial y}{\partial \theta'} & \frac{\partial y}{\partial z'} \\[6pt] \frac{\partial z}{\partial \rho'} & \frac{\partial z}{\partial \theta'} & \frac{\partial z}{\partial z'} \end{bmatrix} \qquad (2.5)$$

where the Jacobian matrix transformation (J) transforms from Cartesian to the warped cylindrical coordinates and the inverse Jacobian matrix transformation (J^{-1}) transforms from the warped cylindrical coordinates back to the Cartesian coordinates and $\left| J^{-1} \right| = |J|^{-1}$.

Using the warped coordinates expressed in Equation 2.3 with Equation 2.4 renders the ideal TO cylindrical cloak parameters from [36]. The complete derivation of these parameters is presented in Appendix C.

$$
\begin{aligned}
\mu_\rho, \epsilon_\rho &= \frac{\rho - a}{\rho} \\[6pt]
\mu_\theta, \epsilon_\theta &= \frac{\rho}{\rho - a} \\[6pt]
\mu_z, \epsilon_z &= \frac{\rho - a}{\rho} \left(\frac{b}{b - a} \right)^2
\end{aligned}
\qquad (2.6)
$$

A few observations can be made now that will be used later in this dissertation. Notice first, that the configuration of the desired fields is being dictated only through a change in the material parameters created by the coordinate transform. Specifically, boundary conditions are not a consideration. Second, note the dual nature of the material parameters, i.e. $\mu_\rho = \epsilon_\rho$. This indicates the cloaking mechanism is indifferent to incident polarization. These two points are intertwined and will be examined further in later chapters.

Simulated results of the ideal cloak with both Transverse Electric (TE) ($\vec{E}$ is in the $\hat{x}$ and $\hat{y}$ direction and also referred to as TE_z) and Transverse Magnetic (TM) ($\vec{H}$ is in the $\hat{x}$ and $\hat{y}$ direction and also referred to as TM_z) incidence can be seen in Figure 2.3; this figure shows the $x - y$ plane. Cloaking effectiveness is exhibited by the fields bending around the cylinder and the apparent lack of perturbation of the fields outside of the structure as

compared to the field pattern of a bare PEC cylinder seen in Figure 2.4. This is further exhibited by the bistatic Radar Echo Width (REW) seen in Figure 2.5. It i important to note at this point that, as seen in Equation 2.6, the TO cloak does not take incident field polarization into account. That is, the parameter values needed for TM incidence ($\epsilon_z, \mu_\rho, \mu_\theta$) are exact duals of those required for TE incidence ($\mu_z, \epsilon_\rho, \epsilon_\theta$). However, the simulations show a stark difference between the cloaking effectiveness between the two polarizations. This will be discussed further in Chapter 4.

At this point it is important to mention that, as was noted in [6, 8], the computer simulations of the ideal anisotropic TM and TE cloaks are less than ideal due to the discretization required and the singularities at the cylinder-cloak interface. These simulated ideal anisotropic cloaks implemented identical meshes with a Maximum Element Length (MEL) of $.05\lambda$. Even with identical meshes, the difference between the incident polarizations of the simulated ideal cloaks is stark. Not only does the TE cloak have much lower scattering than the TM cloak, but the shape of the REW is quite different. This could be due to the fact that waves are impinging the PEC in the simulation since the boundary condition at the PEC is polarization dependent. Additionally, TE and TM impingement upon a coated PEC cylinder excite very different azimuthal surface waves which do affect the REW [47].

The material requirements of Equation 2.6 state that the ideal cloak requires a single layer of spatially varying anisotropic parameters. Furthermore, when $\rho = a$ at the cylinder-cloak interface the material parameters in the $\hat{\rho}$ and $\hat{z}$ direction take on values of 0 while the parameters in the $\hat{\theta}$ direction are ∞. Due to these material requirements, the ideal TO cloak design dictated by Equation 2.6 is not manufacturable. The following sections serve as a summary detailing the different attempts to approximate the required cloaking material in an effort to make it more physically realizable.
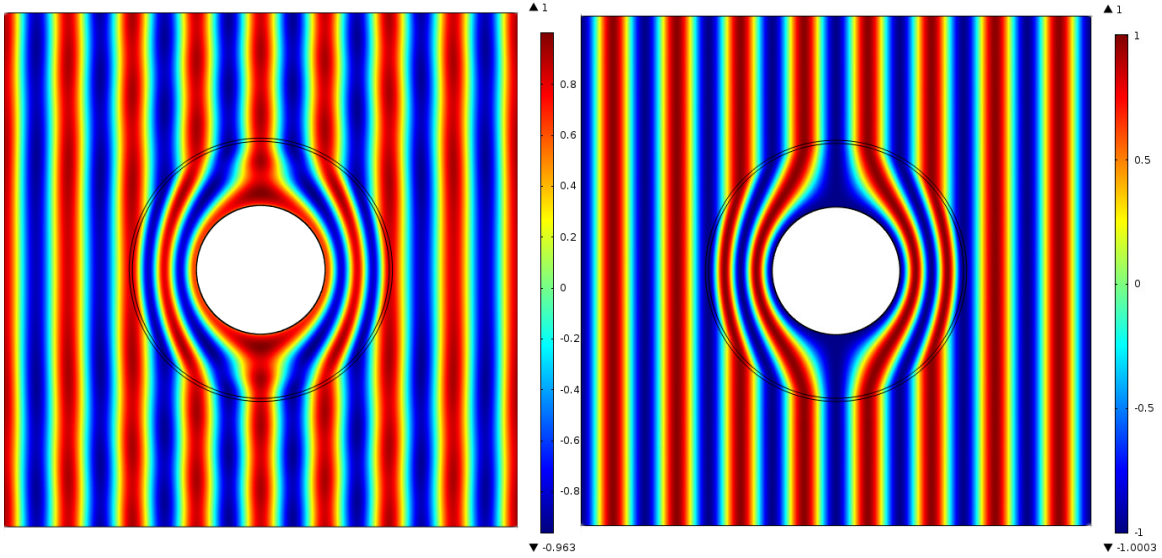
Figure 2.3: Normalized $\hat{z}$ directed fields of the ideal TO cloak for TM incidence(left) and TE incidence(right). The power flow is from left to right.
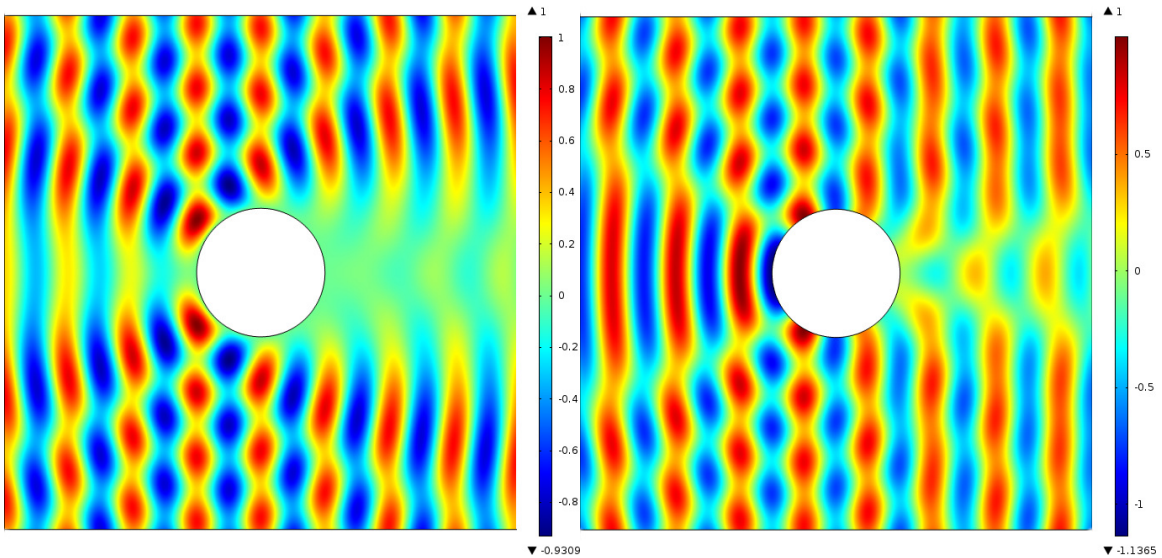
Figure 2.4: Normalized $\hat{z}$ directed fields for a bare PEC cylinder with TM incidence(left) and TE incidence(right). The power flow is from left to right.
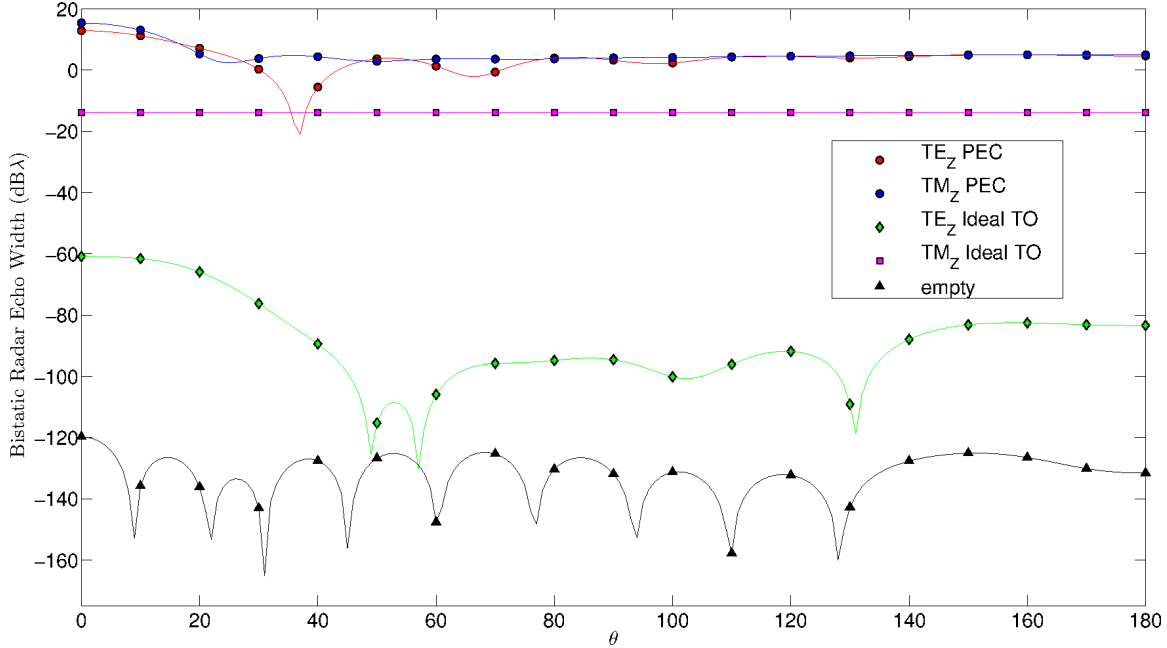
Figure 2.5: REW comparison between bare PEC cylinder and ideal TO cylindrical cloaks for TM and TE incidence.

2.2 TO Cylindrical Cloak Approximation

The manufacturing challenges inherent in the TO cloak design sparked further research into approximating the cloak material parameters. This section separates these approximations into two basic categories, anisotropic approximations (Section 2.2.1) and isotropic approximations (Section 2.2.2). Within these sections are also efforts to approximate the single cloak layer made of spatially varying material parameters into discrete layers of homogeneous material. Both material parameter and discrete homogeneous layer approximations of the TO design are required if a physical cloak is to be realized. The obvious problem here is that with two simultaneous approximations (material and geometry), the ideal cloak behavior becomes severely degraded. Optimization can be used to mitigate the degradation caused by these approximations; this topic is covered in Section 2.2.3.

13

2.2.1 Anisotropic Material Parameter Approximation.

The first approximation of the TO design is used in conjunction with the first manufactured cloak where Schurig *et al* created a simplified set of anisotropic parameters seen in Equation 2.10 [36]. First, we start with the wave equation in an anisotropic medium impinged by a TM field as seen in Equation 2.7.

$$\frac{1}{\epsilon_z \rho}\left[\frac{\partial}{\partial \rho}\left(\frac{\rho}{\mu_\theta}\frac{\partial E_z}{\partial \rho}\right)\right] + \frac{1}{\epsilon_z \rho^2}\frac{\partial}{\partial \theta}\left(\frac{1}{\mu_\rho}\frac{\partial E_z}{\partial \theta}\right) + k_0^2 E_z = 0 \qquad (2.7)$$

In [36], it was assumed that μ_θ was invariant and therefore could be removed from the differential operator. After factoring out the μ_θ term from the differential operator and substituting Equation 2.6 into Equation 2.7, the result is Equation 2.8.

$$\left(\frac{b-a}{b}\right)^2 \frac{\partial^2 E_z}{\partial \rho^2} + \left(\frac{b-a}{b}\right)^2 \frac{1}{\rho}\frac{\partial E_z}{\partial \rho} + \left(\frac{b-a}{b}\right)^2 \left(\frac{1}{\rho-a}\right)^2 \frac{\partial^2 E_z}{\partial \theta^2} + k_0^2 E_z = 0 \qquad (2.8)$$

Next we can solve for the simplified cloak parameters as seen in Equation 2.9.

$$\begin{aligned} \frac{1}{\epsilon_z \mu_\theta} &= \left(\frac{b-a}{b}\right)^2 \\ \frac{1}{\epsilon_z \mu_\rho} &= \left(\frac{b-a}{b}\right)^2 \left(\frac{\rho}{\rho-a}\right)^2 \end{aligned} \qquad (2.9)$$

Since μ_θ was assumed to be constant, we assign it a value of 1 and can solve Equation 2.9 to render to required parameters for the simplified cloak presented in [36].

$$\epsilon_z = \left(\frac{b}{b-a}\right)^2 \quad \mu_\rho = \left(\frac{\rho-a}{\rho}\right)^2 \quad \mu_\theta = 1 \qquad (2.10)$$

This allowed Schurig *et al* to design a cloak where ϵ_z and μ_θ are constant while μ_ρ is the only parameter that varies. This design was then implemented with discrete layers of metamaterials. It is difficult to tell exactly how well the physical cloak performed as compared to the bare PEC cylinder since no REW measurements were presented. As a

point of comparison, simulations of the simplified cloak for our geometry were conducted and are presented in Figure 2.6 and 2.7 . Note the degradation of cloaking effectiveness evidenced by the effects of constructive and destructive interference in the fields outside of the structure which is also seen in the REW measurement.
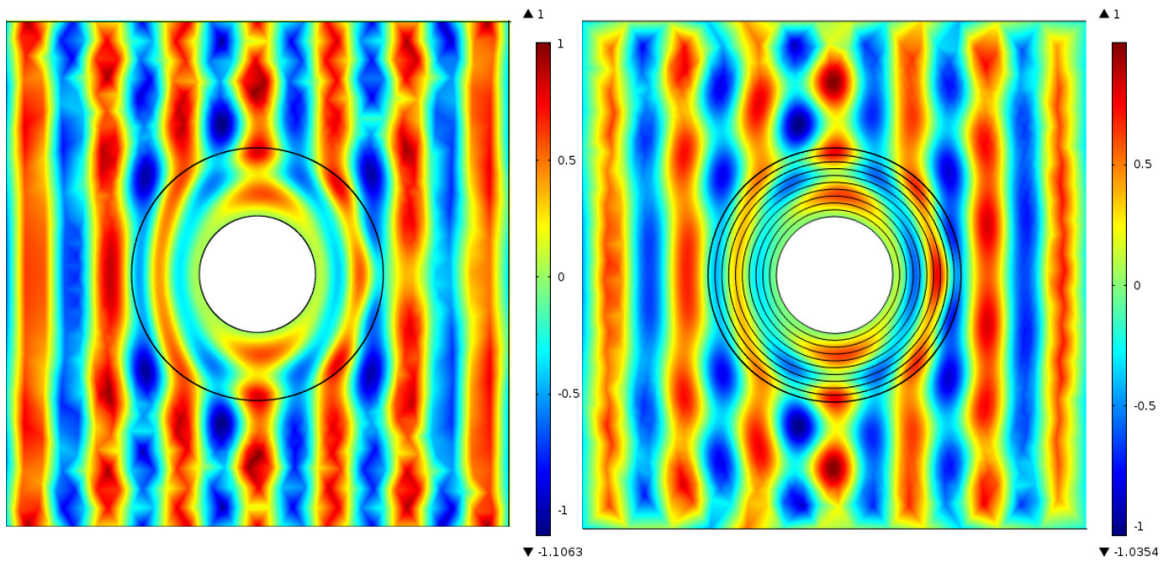
Figure 2.6: Field pattern of cloak made from continuous simplified parameters (left) and discrete layered approximation of the simplified parameters (right). Power flow is from left to right.

Yan *et al* showed that the assumption of a constant μ_θ allowed the zero order incident wave to penetrate and reflect through the cloak material [52]. Later, Yan et al increased the effectiveness of the simplified cloak by impedance matching the outer layer through manipulating the coordinate transform. This resulted in a new set of simplified material parameters as seen in Equation 2.11.
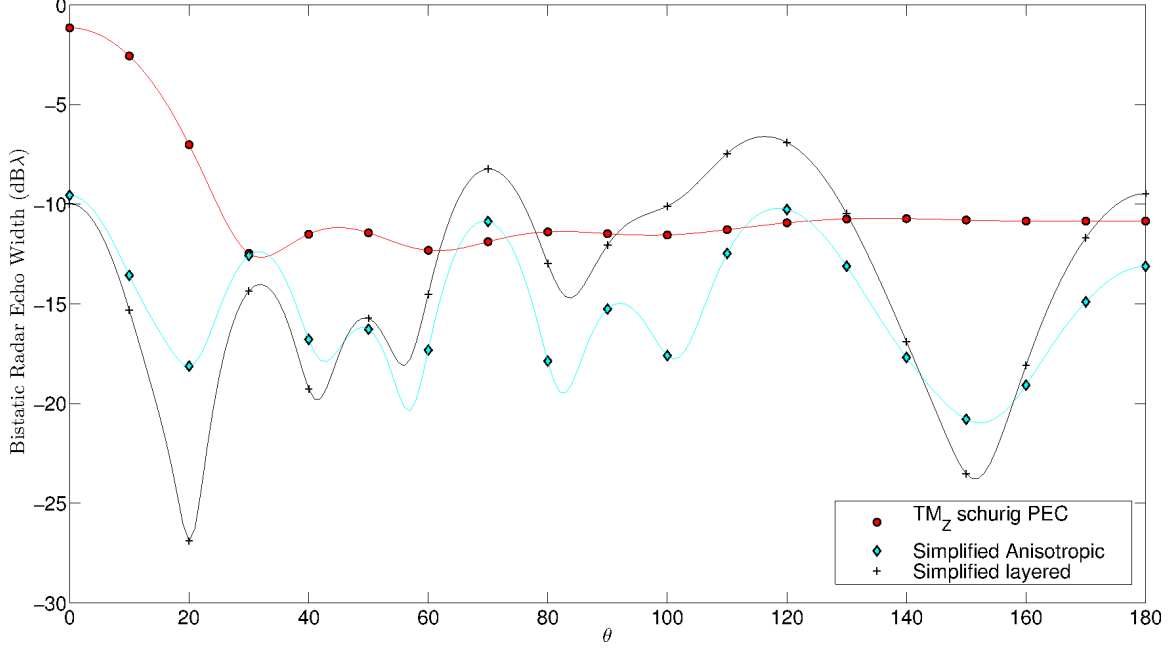
Figure 2.7: Comparison of simplified cloaks using geometry from [36]; $a = 27.1mm$, $b = 58.9mm$ and the frequency is 8.5GHz.

$$
\begin{aligned}
\mu_\rho, \epsilon_\rho &= \left(\frac{\rho - a}{\rho}\right)^2 \frac{b}{b - a} \\
\mu_\theta, \epsilon_\theta &= \frac{b}{b - a} \\
\mu_z, \epsilon_z &= \frac{b}{b - a}
\end{aligned}
\tag{2.11}
$$

This line of research was later expanded by Collins and McGuirk [6]. They presented a third constraint equation to the two in Equation 2.9 by not assuming a constant μ_θ. These new constraints still maintained the impedance matching at the outer layer. These constraint equations can be seen in Equation 2.12.

$$\frac{1}{\epsilon_z \mu_\theta} = \left(\frac{b-a}{b}\right)^2$$

$$\frac{1}{\epsilon_z \mu_\rho} = \left(\frac{b-a}{b}\right)^2 \left(\frac{\rho}{\rho-a}\right)^2$$

$$\frac{1}{\epsilon_z \mu_\theta}\frac{1}{\rho} - \frac{\mu_\theta'}{\epsilon_z \mu_\theta} = \frac{1}{\rho-a}\left(\frac{b-a}{\rho}\right)^2 \tag{2.12}$$

The notation $'$ indicates differentiation with respect to ρ. With a focus on fabrication, Collins and McGuirk decided not to solve the differential equation constraint in Equation 2.12 explicitly, but instead they chose to use a Taylor series approximation. Using the Taylor series approach allows a method to scale the material parameters by limiting the number of Taylor series coefficients. As the number of Taylor series coefficients tends toward ∞, we get the ideal TO cloak. They also showed that the simplified parameter set presented in [53] is the first term in the Taylor series approach.

Even with these different sets of simplified parameters, better cloaking performance required material parameters to approach the singularities at the cylinder-cloak interface. One could offset the cloak a small amount, δ, such that the inner cloak boundary is δ away from the cylinder boundary to alleviate this problem and approximate the ideal cloak [35]. Although this method did alleviate the problem at the interface, it also showed the cloak was sensitive to this change and created noticeable scattering. Researchers continued to look for a more refined method of approximating the anisotropic cloak with an eye towards manufacturability.

While the efforts mentioned above did simplify the original TO requirements by addressing the singularities at the cylinder-cloak interface and allowed a method of scaling the material parameters, the problem of anisotropy persists and therefore so do the challenges of a physically realizable design.

2.2.2   *Isotropic Material Parameter Approximation.*

The inherent problem with the previously mentioned TO approximations is that they still required anisotropic material parameters and therefore are not manufacturable. Other efforts focused on a cloak made of isotropic layers, these efforts use effective medium theory in order to accomplish this. Effective medium theory states that isotropic layers, sufficiently thin, can be modeled as a single anisotropic layer. Conversely, we can represent the single anisotropic layer of the ideal cloaked cylinder as many isotropic layers. This approximation gets closer to the ideal cloak as the number of layers goes to infinity [18].

In 2006, Wood *et al* used effective media theory to model 2 isotropic layers as a single anisotropic layer with Equation 2.13

$$
\begin{aligned}
\epsilon_\theta &= \frac{\epsilon_1 + \eta\epsilon_2}{1 + \eta} \\
\frac{1}{\epsilon_\rho} &= \frac{1}{1 + \eta}\left(\frac{1}{\epsilon_1} + \frac{\eta}{\epsilon_2}\right) \\
\eta &= \frac{t_2}{t_1}
\end{aligned}
\tag{2.13}
$$

where t_1, t_2 are the layer thicknesses [50]. This approximation allowed for a cloak made of discrete isotropic layers to approximate the anisotropic and spatially varying cloak material dictated by TO [9, 18, 31]. It is important to note that the anisotropic cloak must first be approximated into discrete layers, then each of these discrete layers can be modeled as 2 isotropic layers. This means that a 10 layer isotropic cloak is actually modeling a 5 layer anisotropic cloak. Generally, this is done by splitting up the cloak layer into layers of equal thickness and the ideal TO material parameters at the middle point of each layer are then assigned to that layer. This circumvents the problem of the singularities at $\rho = a$. Then we can apply Equation 2.13 to create 2 isotropic layers to model each of the anisotropic layers. Figure 2.8 shows the fields of the 10-layer effective medium approximation for our geometry and Figure 2.9 shows the corresponding REW comparison.
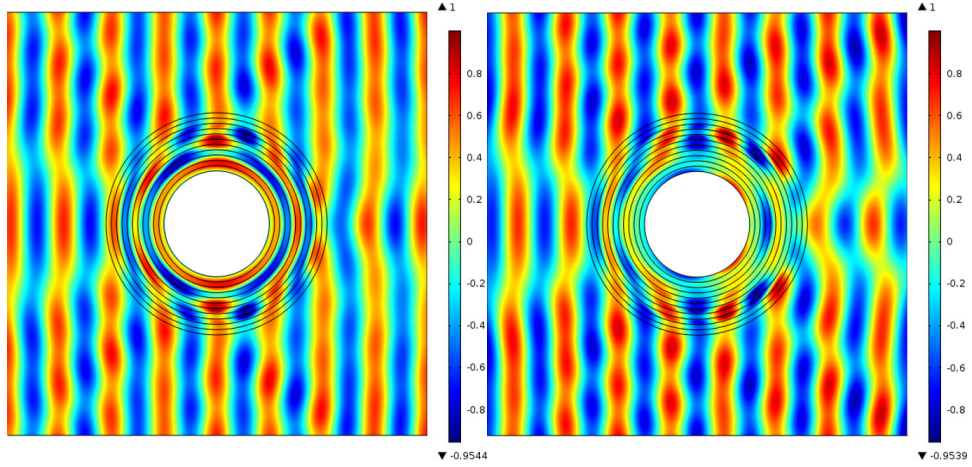
Figure 2.8: Normalized $\hat{z}$ directed fields of the effective medium isotropic approximated ideal cylindrical cloak with TM incidence(left) and TE incidence(right). The power flow is from left to right.
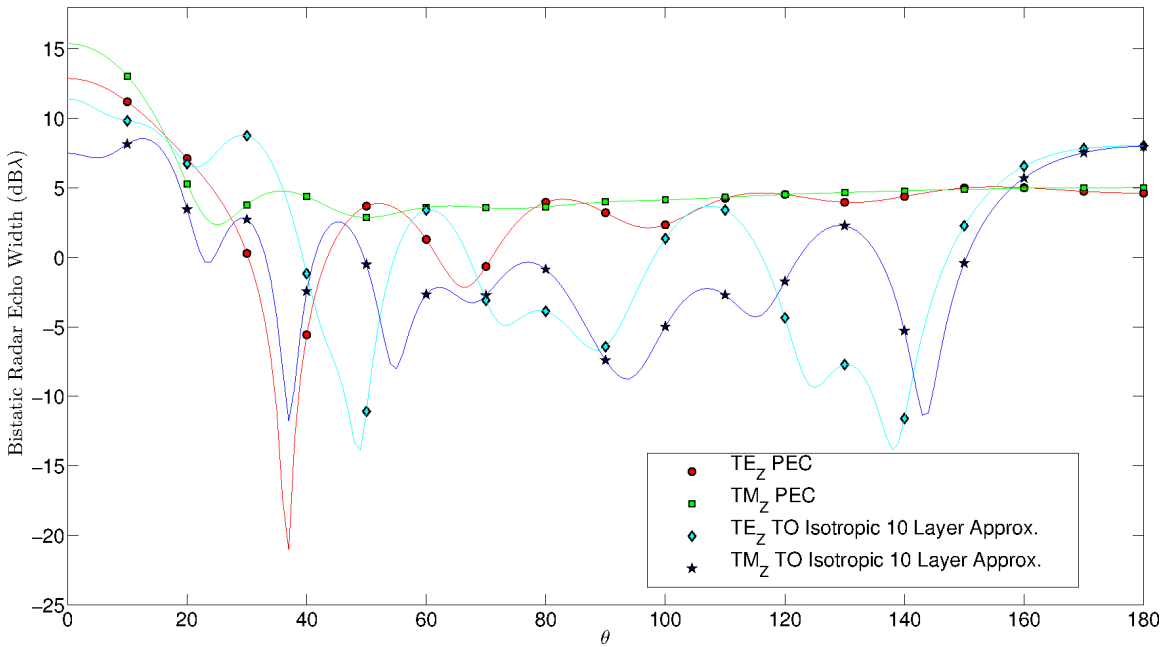
Figure 2.9: REW comparison of the effective medium isotropic approximation of the ideal TO cylindrical cloak.

19

Needless to say that even with effective medium approximations, the cloaking performance is still quite degraded from the ideal TO cloak. This spurred further research into manipulating the effective medium isotropic cloaks in the hopes of increasing cloaking effectiveness. In 2007, Huang *et al* showed that layer thicknesses of the effective medium layers could be manipulated in an effort to increase the performance of the effective medium isotropic cloak material dictated by Equation 2.13 [9]. In 2010, Qui *et al* experimented with reordering the effective medium isotropic layers [32]. They showed that by reordering the layers such that the index of refraction exhibits a smoother profile, decreasing as the layers get closer to the cylinder, one could increase the cloaking effectiveness over the effective medium approximation. One of the problems with using effective medium theory is that the more, and consequently thinner, layers used to approximate the anisotropy, the better the approximation. In [18], McGuirk *et al* had to use 5,000 isotropic layers to match the results of the anisotropic cloak layer using the same geometry as Figure 2.1. This creates its own manufacturing challenges.

In the efforts referenced above, approximations are used to achieve material parameters and a geometry that are more manufacturable than the original TO design. Approximating the TO cloak design in this manner is iterative and results in a brute force attempt to achieve both cloaking effectiveness and manufacturability. Instead, we turn to optimization techniques to provide an intelligent way of approximating the ideal TO design with the goal of finding a manufacturable design which optimizes cloaking effectiveness.

2.2.3   *Optimizing a Cylindrical Cloak.*

The previously mentioned efforts have attempted to find the best way of matching the material parameters dictated by TO with those that are physically realizable. The next three efforts implement an optimization approach [29, 51, 54] to this problem. The following optimization approaches assume a PEC cylinder interior with a non-ideal cloak material which will allow field penetration. Optimizing this type of structure will use the material

gradient but will also take into account the PEC boundary making this type cloak operate more like a waveguide than the traditional cloak.

In any optimization method, one derives a cost functional which provides a figure of merit for a given set of system parameters. The optimization algorithm will then search different combinations of the system parameters to either maximize or minimize the associated cost functional. In the case of the cylindrical cloak, we wish to have a cost functional which describes the amount of scattering due to the cloaked cylinder. The input of this cost functional consists of the material parameters and geometry of the cylindrical cloak. Since we are optimizing to create a more manufacturable cloak, a layered cylindrical cloak geometry is used.

The first use of optimization applied to the cylindrical cloak was by Popa and Cummer in 2009 [29]. In this effort, 3 layers of homogeneous anisotropic material is assumed. The equation for bistatic REW is used as the cost functional and is derived by expanding the fields and applying boundary conditions to get an expression for the scattered fields. Specifically, they optimized the REW for forward scatter (source and receiver are exactly opposite each other with the cloaked cylinder in the middle). They then used an optimization algorithm to find the anisotropic values which minimized their cost functional. A discretized approximation of the TO ideal cloak was used as an initial guess for the optimization algorithm. They showed that a 3 layer optimized cloak outperformed a 100 anisotropic layer approximation of the TO design. The approach in [51] is similar but used a 4 layer design and optimized over an average of the bistatic angles with similar results.

Later, in 2011, Zhenzhong *et al* applied optimization to a 6 layer isotropic cloak made of 2 types of non-magnetic materials [54]. They also implemented the REW equation as the cost functional by expanding the fields and enforcing boundary conditions. However, unlike [29], Zhenzhong *et al* summed the scattering width for every incident

21

angle. This cloak was optimized for the 2 alternating non-magnetic materials and the 6 layer thicknesses.

Note that in these examples one must either optimize for a single incident angle, which does not ensure all angle cloaking or engage in the computationally expensive operation of accounting for the REW of every incident angle. Secondly, the cost functionals derived in these examples are specific to the stratification profile and therefore, if the number of layers were to change, a new cost functional would need to be derived. It is also important to point out that although the conclusion is not drawn in these references, these types of optimization techniques are more effective than approximating the ideal TO method of cloaking a cylinder because they account for the inevitable field penetration and the subsequent PEC boundary condition.

2.3   Summary

TO has provided a clever way to control fields and imagine new structures. However, the material requirements for these structures are not manufacturable. Many attempts have been made to approximate the TO requirements for a cylindrical cloak but these simple approximations either degrade cloaking effectiveness or render material parameters that are not manufacturable. Furthermore, simply approximating the TO design is an iterative approach in that there is no direct correlation between the TO coordinate transform employed and cloaking performance. Optimization was later used in order to provide an intelligent way to optimize the TO cloak. To implement the optimization techniques, a cost functional is derived from expanding the fields and enforcing boundary conditions to get an expression that describes the scattering of the cloaked structure.

Optimization shows the most promise in being able to design a cloak with manufacturable parameters. However, these optimization techniques suffer from two main problems. First, the cost functional is specific to a stratification profile and therefore not general. Secondly, this cost functional must be optimized over every bistatic angle to

ensure the cylinder is cloaked from an observer regardless of position; this is very time consuming considering the optimization algorithm must compute this cost functional many times before finding a solution.

A general expression of a Green's function for an n-layered dielectric coated cylinder will be presented in Chapter 4. From this Green's function, a cost functional that is independent of incident angle is developed and used to optimize an isotropic approximation of the TO cloak in Chapter 5. Then in Chapter 6, the cost functional will be used to design and fabricate a metamaterial cylindrical cloak that is not based on TO. In the next Chapter, we will look at metamaterials and a design process which will provide the possible solutions that an optimization algorithm could search through to design a manufacturable cloak.

III.   Metamaterial Background

In Chapter 2 some of the challenges of designing a cloak with material parameters that are physically realizable was discussed. The most promising approach is to use an optimization technique to search through possible realizable material parameters to find the combination that results in optimal cloaking. While optimization seems the best choice to loosen the constraints on the TO ideal cloak design, it is also prudent to increase granularity of the material parameters that can be physically realized so that we can approach the problem from both sides.

The somewhat recent development of metamaterials could be the solution to expanding the possibilities of manufacturable material parameters. In essence, metamaterials are made of cells of small metallic structures (much smaller than the wavelength) which are somewhat analogous to the atomic structure of a material found in nature. These metamaterial cells resonate through the field coupling within each cell and through field coupling between neighboring cells. In the end, the material parameters of this metamaterial can be tailored through the geometric features of the metallic structure that makes up the unit cell. In this effort, we limit ourselves to metamaterial cells that consist of metallic traces on a PCB (PCB) substrate.

In this Chapter, we will discuss how traditional materials are characterized since this method will also be applied to metamaterials. Furthermore, we will also discuss size constraints of the metamaterial cells and how the material parameters of these metamaterials can be extracted and modeled. Lastly, we will discuss a design process which incorporates a resonance model which allows us to create a pool of possible material parameters and their corresponding metamaterial cell geometry. In Chapter 6, it is through this pool of achievable material parameters that we will use an optimization algorithm to search through to design an optimized cylindrical cloak consisting of metamaterials.

3.1 Material Characterization

In essence, the material characterization parameters of electric permittivity (ϵ) and magnetic permeability (μ) are simply the macroscopic averages of the microscopic effects produced by the interaction between time harmonic fields and the atomic structure of a material [2]. When an atom comes into contact with an electric field, the nucleus and the electron become displaced, creating a dipole. Macroscopically, all of the dipoles of the material are then accounted for by an electric polarization vector. The electric permittivity is then introduced to account for the electric polarization vector. Likewise, the permeability of a magnetic material, subject to a magnetic field, is an average of the many magnetic polarization vectors caused by the orbiting and spinning of the electrons. The movement of an electron constitutes a current, so this motion can be modeled as current carrying loops.

Metamaterials seek to replicate these microscopic models which form the basis of material characterization. To achieve permittivity, we achieve the dipole by ensuring the electric field crosses two metal plates and thus incurring opposite charges on each plate. To achieve permeability, we ensure the magnetic field is perpendicular to a wire loop and thereby inducing a current in the loop. These metallic structures have inherent resistances, inductances and capacitances and therefore they will resonate at a specific frequency. When these metallic structures are impinged by an electromagnetic wave with the same frequency as their own resonant frequency, the electric polarization vector or magnetic polarization vector exhibits this resonance and therefore so does the material parameter.

So, with metamaterials we seek to create a material made of small metallic structures that will mimic the atomic modeling of traditional materials when an electromagnetic field is present. The question then becomes one of size constraints. At what point can we average the reactions of all of the metamaterial unit cells as atoms of a material instead of accounting for them as individual scatterers?

3.2 Metamaterial Introduction

Creating artificial parameters is not a new idea. In 1946 Kock described a method of designing periodic structures to create a microwave lens [12]. In this effort periodic plates are formed in an array. The idea of creating an artificial permittivity was shown again in 1962 when Rotman showed that either a rodded structure or parallel plate guide could be used to create an effective permittivity [34]. The idea of rodded structures was furthered in [27] where 3D lattices of thin metal wires were created to render a negative permittivity.

In 1999, Pendry *et al* explained how an effective magnetism could be achieved from microstructures built of conducting sheets [26]. The periodic lattice of these microstructures would later be known as metamaterials and the microstructures themselves known as metamaterial cells. These metamaterial cells contain internal capacitances and inductances which lead to the resonance exhibited in the material parameters. The metamaterial cells presented in [26] were made of Dual Split Ring Resonators (DSRR) as seen in Figure 3.1. The cells would be impinged by a field where the magnetic field component is only in the $\hat{z}$ direction (TE_z). The magnetic field then induces a current along the rings which would resonate at a frequency dictated by the internal capacitances (at the ring splits and space between the rings) and inductances (distances along the metallic path). This is analogous to the microscopic current carrying loop model of traditional materials.

In the hope that one could easily custom design material parameters, this research sparked great interest in the scientific community which resulted in the quickly expanding area of metamaterials. What followed were many efforts to further refine and add rigor to the analysis of metamaterial constraints and material parameter extraction which are discussed in the following sections.
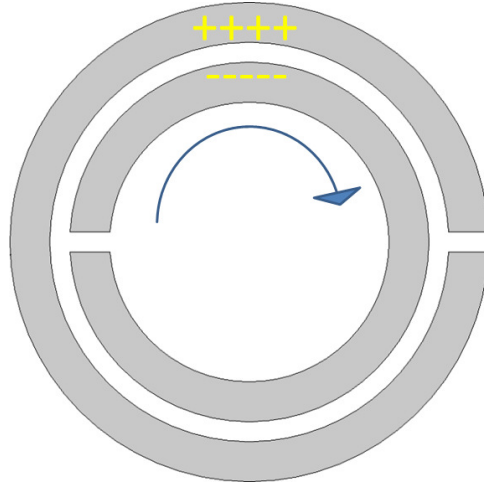
Figure 3.1: DSRR metamaterial cell, the current flow (arrow) is induced by the magnetic field perpendicular to the face of the DSRR and the coupling $(+,-)$ caused by the vertical electric field.

3.3 Material Parameters from Metamaterials

One of the biggest questions in metamaterials is whether material parameters could be used to characterize metamaterials in the same way as traditional materials. While both metamaterials and traditional materials are made of reoccurring structures consisting of metamaterial cells or atoms/molecules respectively, the size difference in their unit cells is quite stark. This creates a challenge when considering the averaging of the individual unit cell responses of a metamaterial. In this section we will discuss metamaterial size constraints for homogenization and the process of material parameter characterization.

3.3.1 Material Parameter Extraction.

In order to extract meaningful material parameters from metamaterials, we first need to know the size limitations of the metamaterial cells such that, from a macroscopic point of view, the metamaterial can be considered a homogeneous material. It is typically accepted that a metamaterial cell must adhere to the following constraint

$$.01 < \frac{a}{\lambda} < .2 \tag{3.1}$$

where a is the distance across the unit cell [40]. This constraint allows us to use the same homogenization techniques used in traditional methods which result in a material parameter characterization of a material. Experimental data agrees with this [37].

Extracting constitutive parameters of metamaterials through reflection and transmission data has been researched extensively [3, 4, 14, 16, 41, 45]. A comprehensive review of this topic can found in [39]. To determine the constitutive parameters of a material, we interrogate it with an incident field and measure the reflection and transmission of the incident field. If we know the polarization of the incident field (which one should in an experimental situation) we can use the measured reflection data (S11) and the measured transmission data (S21) to determine the material parameters of the sample.

The first effort to measure metamaterials experimentally was performed in 2002 by Smith *et al* [41]. This method is based on the well known Nicolson-Ross-Weir technique [20, 49] . As given in [41], the relationship between S11, S21, effective index of refraction (n), effective impedance (η), effective permittivity and permeability is given as

$$
\begin{aligned}
\cos(nk_0d) &= \frac{1}{2T}(1 - R^2 + T^2) \\
\eta &= \sqrt{\frac{(1+T) - T^2}{(1-R)^2 - T^2}} \\
\epsilon &= \frac{n}{\eta} \\
\mu &= n\eta \\
R &= S11 \\
T &= S21e^{-jk_0d}
\end{aligned}
\tag{3.2}
$$

where $k_0 = \omega \sqrt{\mu_0 \epsilon_0}$ and d is the distance across the unit cell in the direction of wave propagation. However, there are some ambiguities in Equation 3.2. Specifically, the correct

sign must be determined for both η and n and the equation for n has the added complexity of choosing the correct branch. To determine the proper signs we can apply the passivity constraints seen in Equation 3.3.

$$
\begin{aligned}
Re(\eta) &> 0 \\
Im(n) &< 0
\end{aligned}
\tag{3.3}
$$

This still leaves choosing the correct branch cut determine the real part of n as seen in Equation 3.4

$$
Re(n) = \pm Re\left(\frac{\cos^{-1}\left(\frac{\left[1-\left(R^2-T^2\right)\right]}{2T}\right)}{k_0 d}\right) + \frac{2\pi m}{k_0 d}
\tag{3.4}
$$

where m is an integer. While the sign of the real part of n is determined by the passivity constraints, the correct branches can be identified by measuring multiple thicknesses of the metamaterial and choosing the branches that yield consistent results for all thicknesses [41]. This method creates the overhead of simulating or measuring multiple samples but later in 2010, Szabó *et al* used the Kramers-Kronig relation to determine the appropriate branch and thereby eliminating the need for multiple sample thicknesses [45]. This method is used for extracting metamaterial parameters in this dissertation.

In the next sections, examples of electrically and magnetically resonant metamaterial unit cells are presented. The electrically resonant cells resonate due to the coupling of the electric field and is manifested as a resonant permittivity. The magnetically resonant cells resonate due to the coupling of the magnetic field resulting in a resonant permeability.

3.3.2 *Electrically Resonant.*

Analogous to how permittivity is determined in a traditional material, permittivity in a metamaterial is the result of the many dipoles created in the individual metamaterial unit cells. This occurs when the electric field is perpendicular to at least two separated

plates. This forces the plates to become polarized and energy is stored as is the case with a capacitor. When the electric field polarization switches, the stored energy discharges creating a source in the circuit. The metamaterial unit cell is made of metallic traces which have an inductance as well as a resistance. In the end, the metamaterial unit cell works like RLC circuit.

Consider the Electric-LC (ELC) metamaterial unit cell in Figure 3.2 which was presented in [37]. The electric field couples across the parallel surfaces in the middle of the cell to create a dipole. When the polarization of the electric field switches, the stored energy is discharged through the structure as the parallel surfaces reverse polarity. The extracted material parameters for a bulk metamaterial made of this structure can be seen in Figure 3.3.
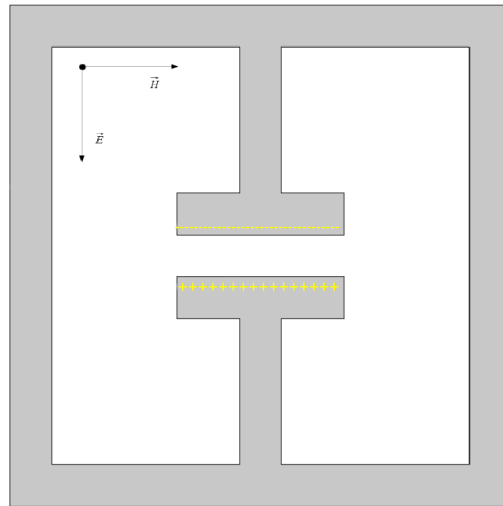
Figure 3.2: Snapshot in time of an ELC metamaterial cell where the incident electric field is creating a dipole across the parallel traces.
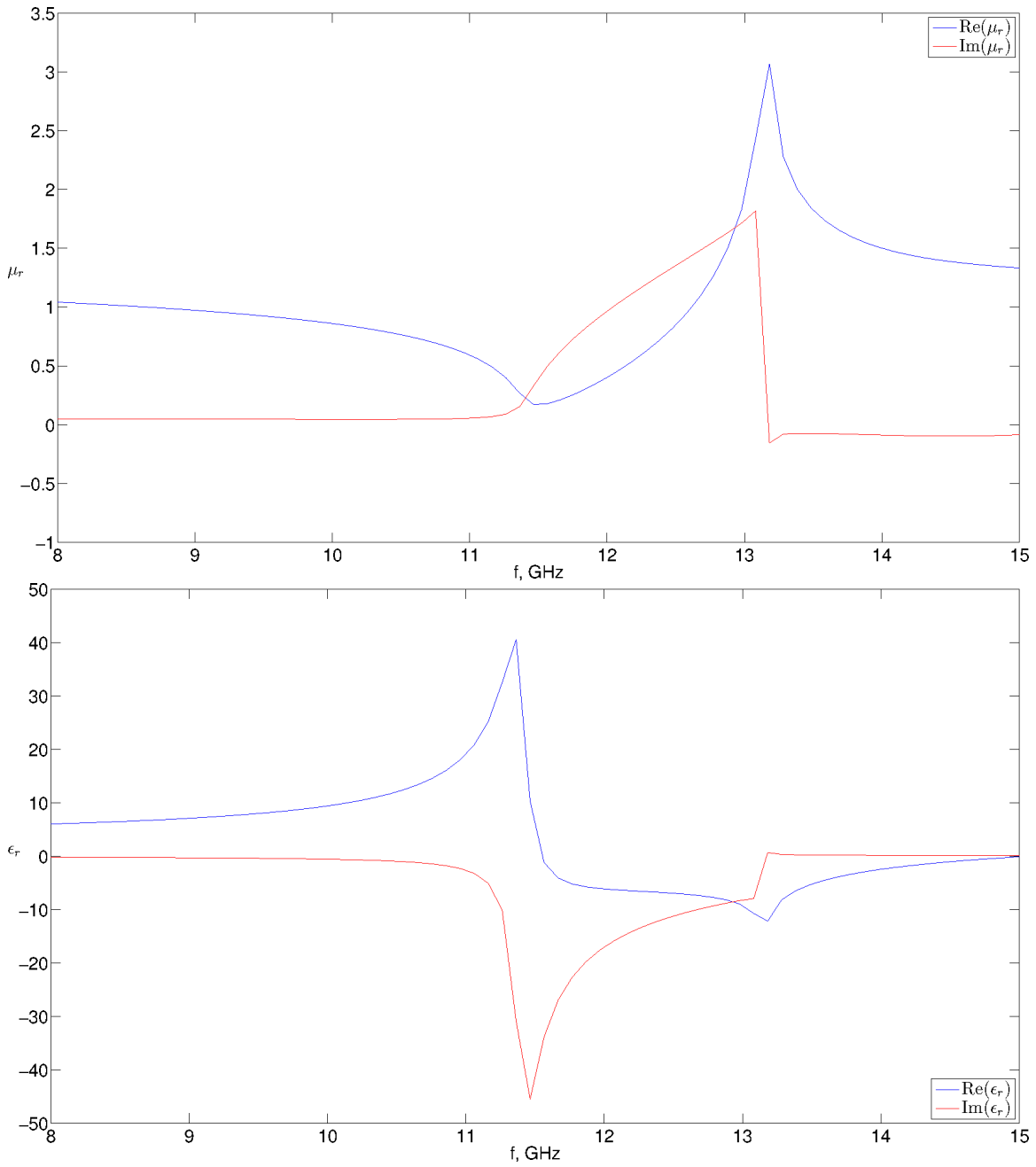
Figure 3.3: Extracted material parameters of an ELC

3.3.3   *Magnetically Resonant.*

As is the case with the electrically resonant structure, a magnetically resonant metamaterial unit cell can be thought of as an RLC circuit except the current is induced as

a result of the magnetic field. A Single Split Ring Resonator (SSRR) with the incident field configuration seen in Figure 3.4 is an example of a magnetically resonant cell. With this unit cell, the magnetic field induces a circulating current into the metal traces which cause the resonance of the RLC circuit. The extracted material parameters of a bulk metamaterial made of this structure can be seen in Figure 3.5.
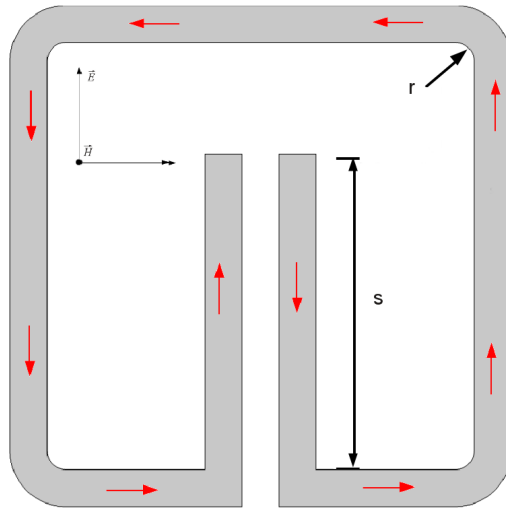
Figure 3.4: Snapshot in time of split ring resonator and the current induced by the magnetic field as red arrows.
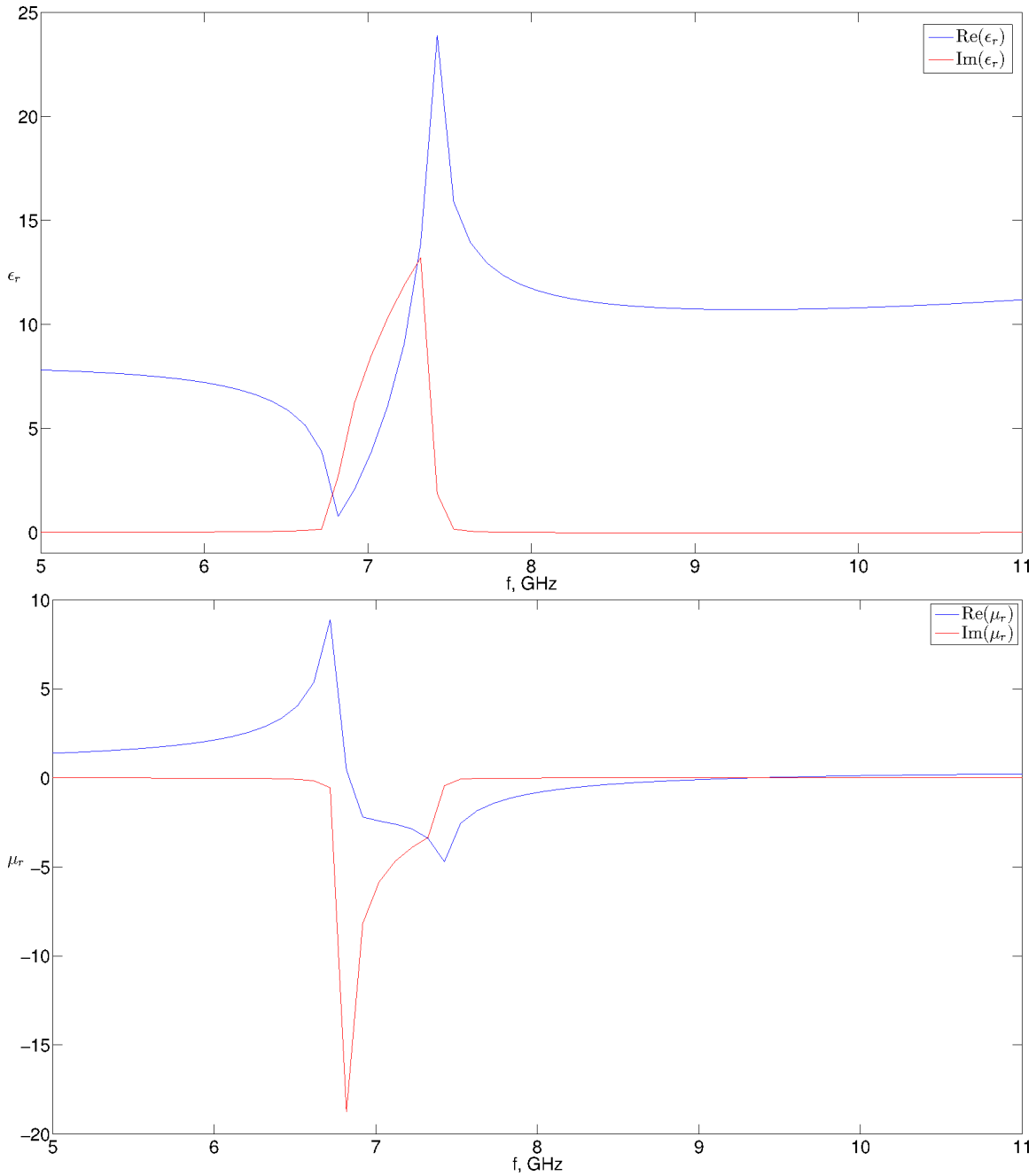
Figure 3.5: Extracted material parameters of an SSRR.

3.4 Modeling Metamaterials

Since we homogenize and ascribe material parameters to metamaterials like we do traditional materials, it makes sense that we would also use the same models we ascribe to

33

traditional materials to predict material parameters in the presence of a time harmonic field. Specifically, we will use the same spring-mass Lorentz models that are used in traditional materials to model the movement of an electron around the nucleus in the presence of a time harmonic field. However, as we will discuss, metamaterials require more complexity in modeling.

The parameters of an electrically or magnetically resonant metamaterial cell can be modeled by the Lorentz form in Equation 3.5

$$
\begin{aligned}
\epsilon_{lorentz}(f) &= \epsilon_b \left(1 - \frac{F_\epsilon f^2}{f^2 - f_{o\epsilon}^2 - j\gamma_\epsilon f} \right) \\
\mu_{lorentz}(f) &= \mu_b \left(1 - \frac{F_\mu f^2}{f^2 - f_{o\mu}^2 - j\gamma_\mu f} \right)
\end{aligned}
\tag{3.5}
$$

where $F_\epsilon, F_\mu, f_{o\epsilon}, f_{o\mu}$ relate to the resonant frequency,$\gamma_\epsilon, \gamma_\mu$ are terms to account for loss and ϵ_b, μ_b represent the background permittivity and permeability [46].

It is important to note the Lorentz model, based on a spring-mass system, does not take into account neighbor to neighbor interactions, what is termed 'spatial dispersion' in [15]. In [15],a Finite Difference Time Domain (FDTD) analysis was performed to average the fields over a slab of metamaterial in an effort to determine how the model must be modified to account for the neighbor to neighbor interactions that are noticeable in metamaterials. This averaging technique was then manipulated to account for both spatial dispersion and multiple resonances in [46] and modified parameters were introduced. The relationship between the extracted material parameters and the modified material parameters can be seen in Equation 3.6 for electric resonant cells and in Equation 3.7 for magnetically resonant cells.

$$\epsilon_{r_{electric}} \quad = \quad \epsilon_m \frac{\frac{nk_0d}{2}}{\tan\left(\frac{nk_0d}{2}\right)}$$

$$\mu_{r_{electric}} \quad = \quad \mu_m \frac{\frac{nk_0d}{2}}{\sin\left(\frac{nk_0d}{2}\right)\cos\left(\frac{nk_0d}{2}\right)} \tag{3.6}$$

$$\epsilon_{r_{magnetic}} \quad = \quad \epsilon_m \frac{\frac{nk_0d}{2}}{\sin\left(\frac{nk_0d}{2}\right)\cos\left(\frac{nk_0d}{2}\right)}$$

$$\mu_{r_{magnetic}} \quad = \quad \mu_m \frac{\frac{nk_0d}{2}}{\tan\left(\frac{nk_0d}{2}\right)} \tag{3.7}$$

With these equations, the modified resonant parameters can be modeled by the Lorentz model. The extracted modified parameters of our example ELC and SSRR metamaterials can be seen in Figures 3.6 and 3.7
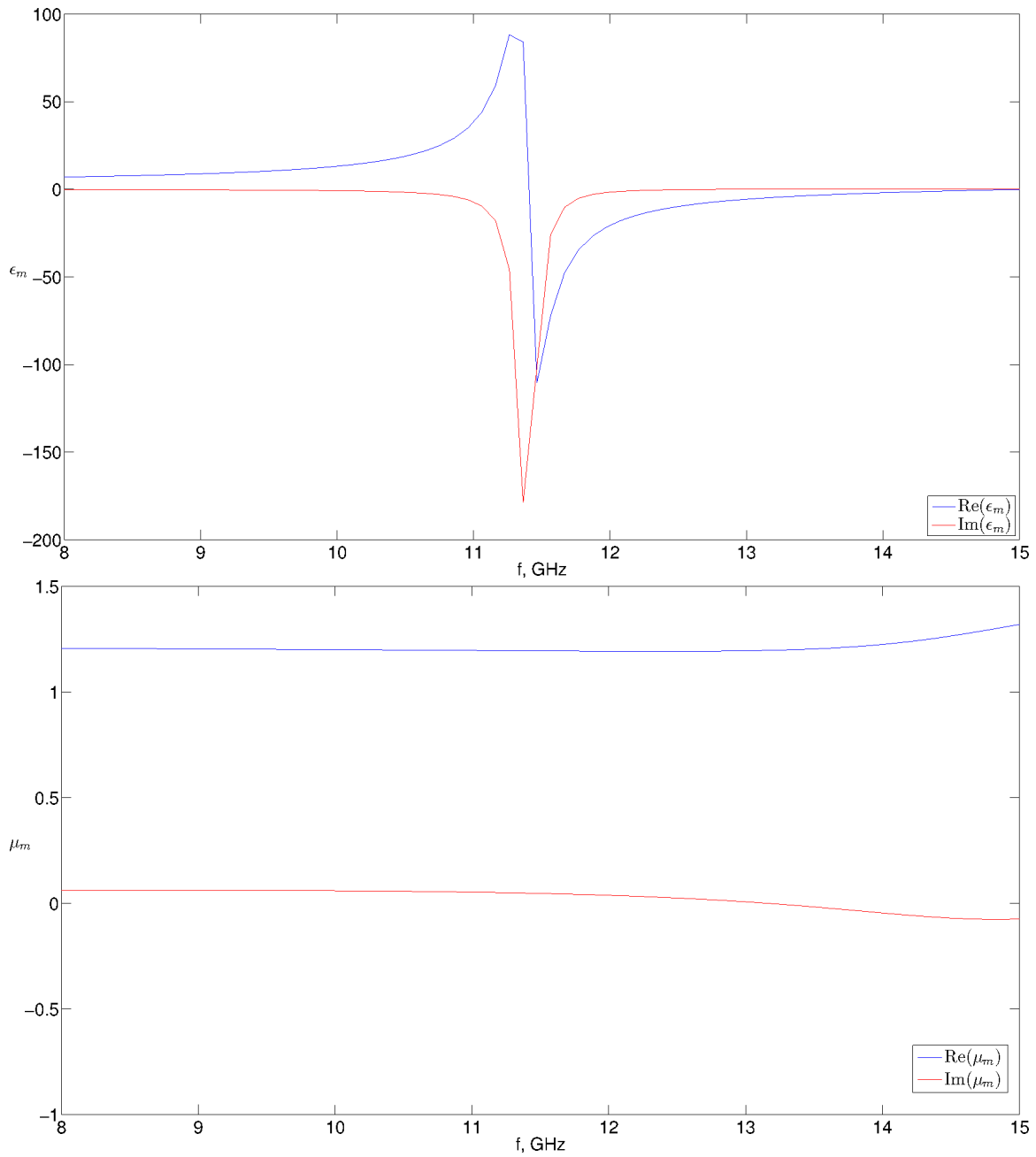
Figure 3.6: ELC Modified Parameters
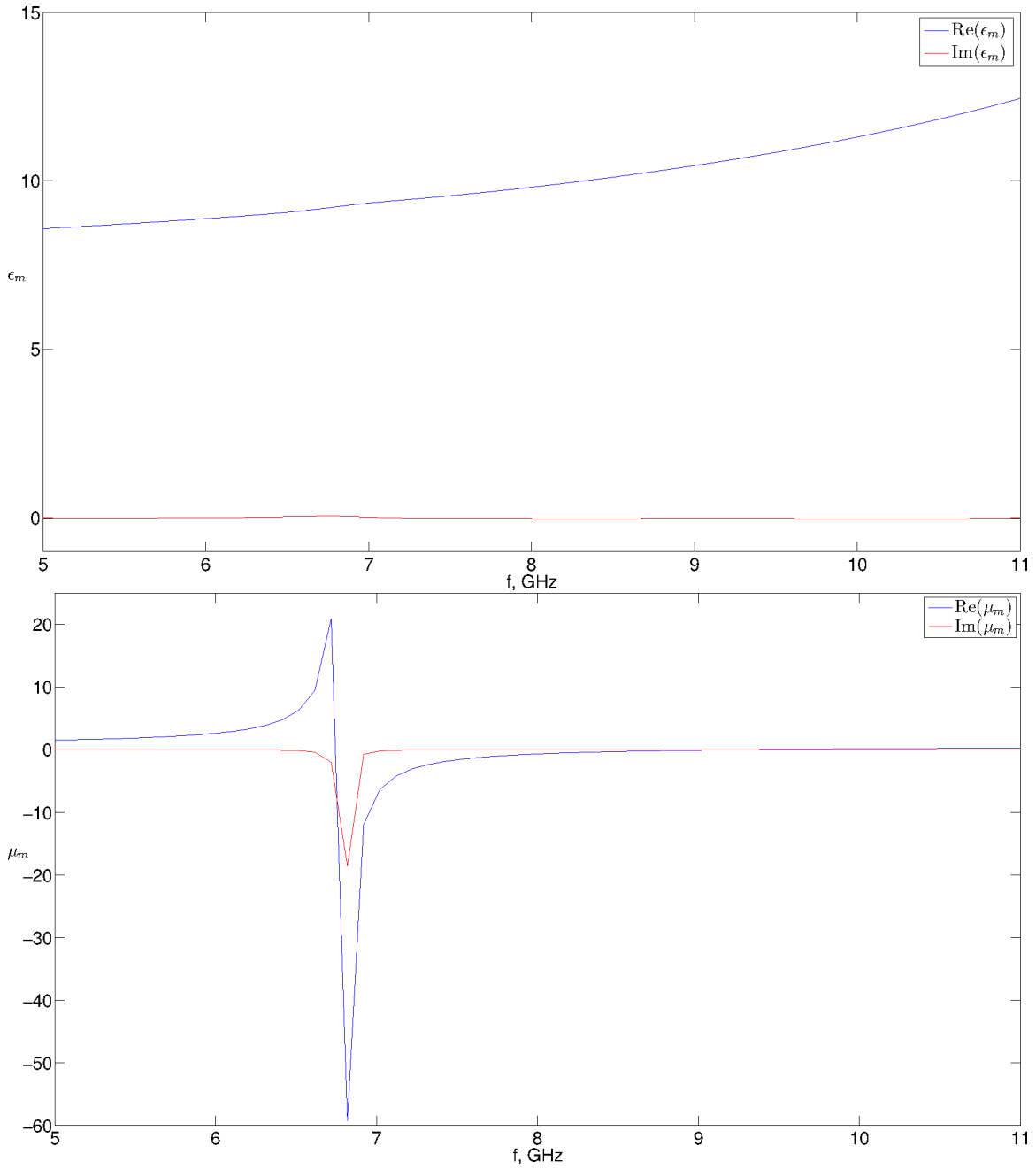
Figure 3.7: SSRR Modified Parameters

In the next section we will show how each of the variables of the Lorentz model in Equation 3.5 are estimated, then expanded into a geometric series which results in a relationship between the material parameters and the unit cell geometry of a metamaterial.

3.5   Design Process

The design process described in this section was first presented in [46] and it creates a searchable database of material parameters and associated metamaterial unit cell geometries. It would be infeasible to run computer simulations for every possible geometric combination to create this database. However, a mathematical relationship between the geometry of a metamaterial unit cell and the resultant bulk material parameters would allow a relatively simple method of accomplishing this. Once a relationship is established, we can use the maximum precision of the target fabrication method to determine all geometric combinations that can be fabricated, rendering material parameters that are physically realizable.

In this design process, we select a metamaterial unit cell and simulate a finite set of geometric variations, then extract the material parameters. For each of these cells, we wish to find the variables in the Lorentz model which accurately describe material parameters of a metamaterial made of the unit cell. Once we have the Lorentz variables for each of the simulated geometries, we can expand these variables into a geometric series so that each variable of the Lorentz model becomes a function of the geometry.

In Chapter 6 we will use this set of achievable material parameters to constrain an optimization algorithm to design an optimal cloak that can be manufactured.

3.5.1   *Model Estimation of the Resonant Material Parameter.*

Previously, we discussed that the extracted material parameters of a metamaterial can be modeled with the Lorentz model through the use of the modified parameters which remove the effects of spatial dispersion. Once the modified parameters are extracted, we can estimate the variables of the Lorentz model. This variable estimation is done through curve fitting using the built in toolbox in MATLAB.

Using the extracted permeability from our example SSRR, we estimate the variables of the Lorentz model that accurately describe the behavior of the modified permeability as

seen in Figure 3.8. It is evident in this figure that the Lorentz model does a good job of describing the behavior of the resonant material parameter. The next section details how we can model the non-resonant material parameter.
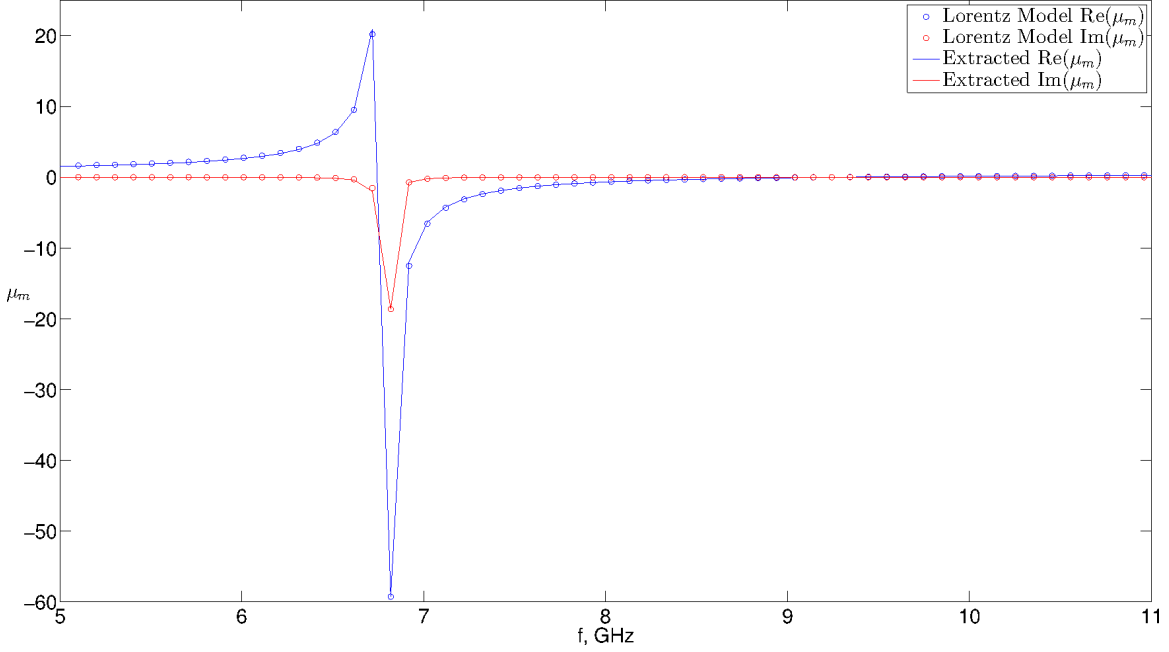
Figure 3.8: Extracted and modeled modified permeability of an SSRR based metamaterial.

3.5.2 *Modeling non-Resonant Material Parameters.*

As seen in Figure 3.7, the modified permittivity is not very dispersive. Therefore, we can simply model the behavior with a frequency series expansion as seen in Equation 3.8

$$\epsilon_m \approx c_0 f + c_1 f^2 + c_2 f^3 \ldots c_{n-1} f^n \tag{3.8}$$

where f is the frequency and the coefficients are the variables of the model that need to be estimated for an accurate description of ϵ_m. The extracted and model description of permittivity of an SSRR can be seen in Figure 3.9.
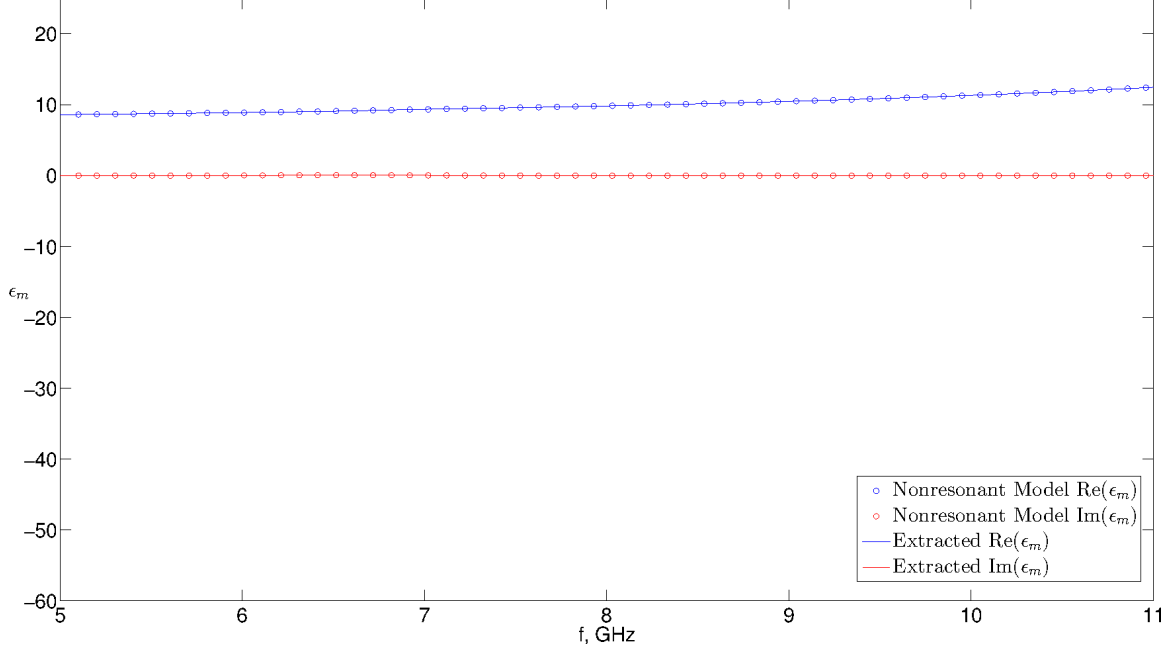
Figure 3.9: Extracted and modeled modified permittivity of an SSRR based metamaterial.

This model can also be used to describe the non-resonant regions of the resonant parameter where dispersion is not very pronounced.

3.5.3 Geometric Series Expansion of Model Variables.

Once we have extracted and modeled the modified material parameters of each of the geometric combinations of metamaterial cells that were simulated, we formulate a relationship between the extracted values and the geometry. This relationship is created by expanding the variables of the models in Equations 3.5 and 3.8 of each of the simulated metamaterials into a geometric series. Using the geometry of the SSRR in Figure 3.4, the geometric series would take the form of Equation 3.9.

$$F_\mu \approx A_0 + A_1 s + A_2 r + A_3 s^2 + A_4 r^2 \dots \tag{3.9}$$

This is done for each of the model variables and the coefficients are estimated to describe the behavior of the variable across the simulated metamaterial geometric combinations.

Once the coefficients are known, we can substitute any geometric value to get the estimated variable and in turn, the estimated material parameter.

3.5.4 Calculating All Manufacturable Material Parameters.

Now that we have an approximate relationship between the geometry and material parameters of a metamaterial, we can create a set of material parameters that can be fabricated. The main constraint in this portion of the design process is to determine the maximum precision of our fabrication process so we can create a distribution of discrete geometries that will be used to calculate the associated material parameters. This portion of the process will provide the modified parameters and corresponding geometries, but the effective parameters are needed. The expressions in Equation 3.10 can be used in conjunction with the passivity constraints of Equation 3.3 and the Kramers-Kronig relation to extract the index of refraction and impedance which can then render the effective material parameters.

$$
\begin{aligned}
\tan\left(\frac{nk_0 d}{2}\right) &= \frac{k_0 d}{2}\sqrt{\mu_m \epsilon_m} \\
\eta &= \sqrt{\frac{\mu_m}{\epsilon_m}}
\end{aligned}
\tag{3.10}
$$

3.6 Design Process Example

As an example to demonstrate and to examine the accuracy of this design process, we use the SSRR unit cell with the geometry seen in Figure 3.10; this example mirrors that in [46]. We choose the dimensions of s and r to vary for the initial simulation step. The different combinations can be seen in Table 3.1. Each of these geometric combinations are simulated and the material parameters extracted. We estimate the model parameters of the resonant model in Equation 3.5 to model the permeability and the non-resonant model in Equation 3.8 to model the permittivity of each simulated geometric combination. Next, these model parameters are expanded as a geometric series, as seen

in Equation 3.9, and the coefficients are solved. Once these coefficients are known, any geometric combination can be used to estimate the associated material parameters. In this example, the material parameters are estimated for every geometric combination within the ranges $s = .1mm - 1.5mm$, $r = .1mm - .3mm$ with a step size of $.01mm$. This process results in 2,961 estimated material parameters and their associated geometric combination of s and r.
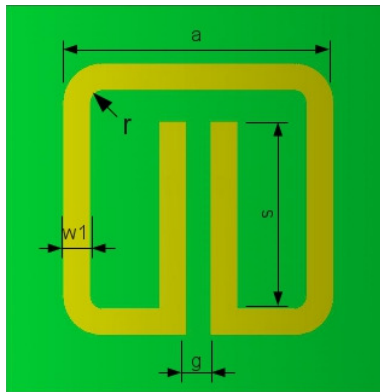
Figure 3.10: Square SSRR unit cell geometry on a 3mm x 3mm PCB substrate with the following static dimensions: a=2.5mm, g=w1=.2mm

In an effort to validate this process and determine accuracy, a set of design process results are compared to simulation results at 10GHz. We use the arbitrarily chosen 16 cells in Table 3.2 for verification of the process. The comparison between the design process material parameters and those simulated are shown in Figure 3.11.

Cell	s(mm)	r(mm)
1	.1	.1
2	.1	.17
3	.1	.25
4	.1	.3
5	.75	.1
6	.75	.17
7	.75	.25
8	.75	.3

Cell	s(mm)	r(mm)
9	1.25	.1
10	1.25	.17
11	1.25	.25
12	1.25	.3
13	1.5	.1
14	1.5	.17
15	1.5	.25
16	1.5	.3

Table 3.1: Design process SSRR geometric combinations.

Cell	s(mm)	r(mm)
1	.3	.12
2	.3	.19
3	.3	.23
4	.3	.27
5	.5	.12
6	.5	.19
7	.5	.23
8	.5	.27

Cell	s(mm)	r(mm)
9	1.13	.12
10	1.13	.19
11	1.13	.23
12	1.13	.27
13	1.41	.12
14	1.41	.19
15	1.41	.23
16	1.41	.27

Table 3.2: Validation SSRR geometric combinations
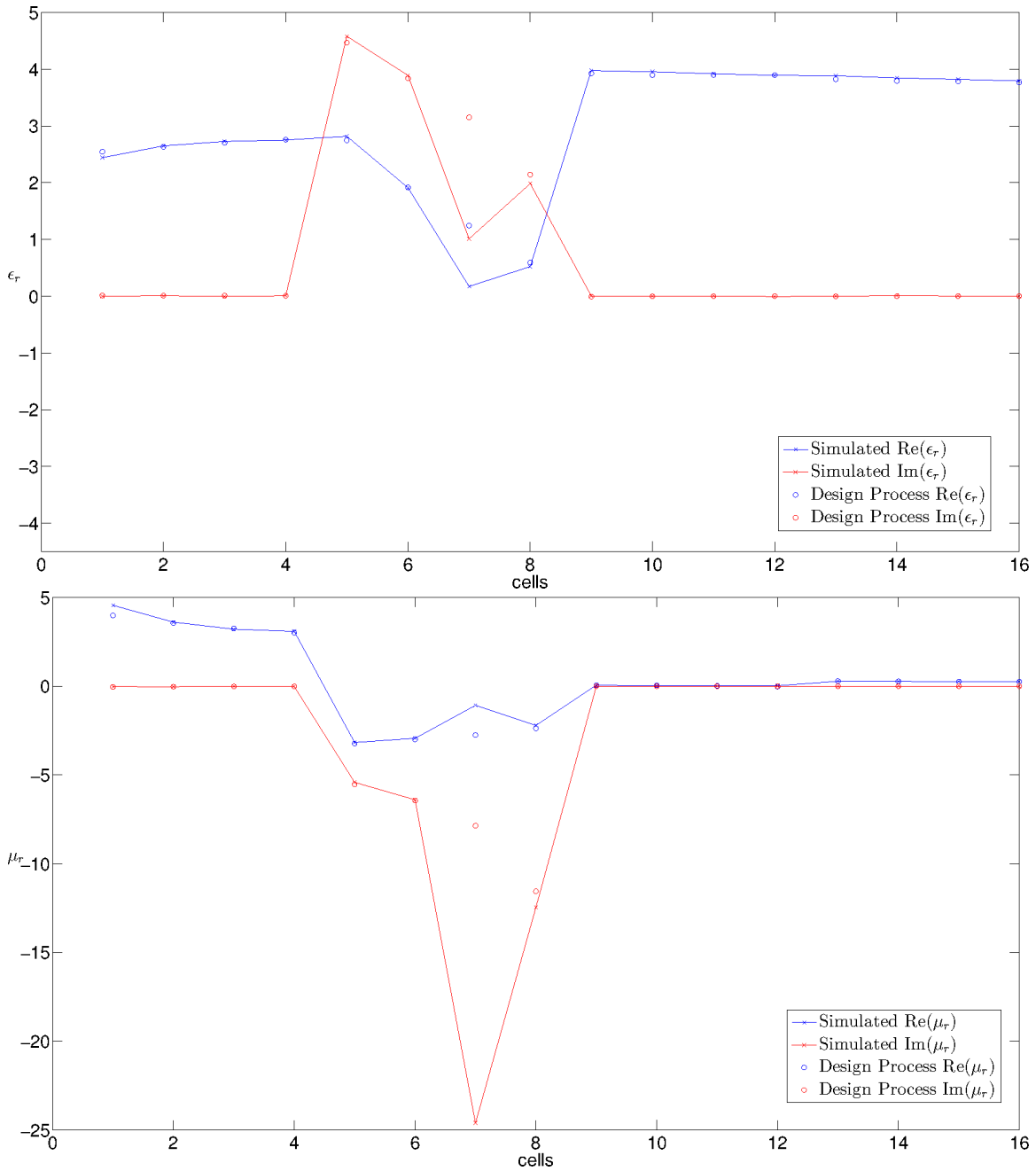
Figure 3.11: Metamaterial design process verification. The x's show the simulation results for the given cell at 10GHz and the o's show the design process results for a cell of the same geometry.

From the validation data, it is evident that the design process was accurate for most of the validation cell geometries, but error is especially evident in Cell 7. The error seen in Cell 7 is due to the fact that Cell 7 resonates at 10GHz. The region of resonance is small, so even a small deviation in the model could render large deviation in the material parameters. In the end, this design process will give good estimations of the material parameters that can be rendered by a metamaterial geometry, but these values will need to be validated through simulation before finalizing any design.

3.7 Summary

In this chapter we discussed the method and validity of assigning material parameters to bulk metamaterials. We also discussed modeling and a design process which provides the relationship between the metamaterial unit cell and the bulk metamaterial material parameters. Using this relationship between the geometry and material parameters of a metamaterial, we can create a set of achievable material parameters and the associated geometric combination. This set of manufacturable material parameters will be used in conjunction with an optimization algorithm to design and fabricate an optimal cylindrical cloak consisting of metamaterial layers in Chapter 6.

IV.   A Green's Function Approach to Cloaking

In Chapter 2, we noted that current research was not amenable to designing a physically realizable cloak. Specifically, the TO process is iterative and does not account for the field penetration that is inherent in any approximation. Furthermore, the efforts in optimization, which do account for field penetration, were not general nor efficient. The goal of this chapter is to develop a general, efficient Green's function based expression to provide the link between cloak geometry/material parameters and cloaking effectiveness. This expression could then be used as a cost functional for optimizing a cloak of any stratification profile and provide insight to the scattering mechanisms.

Previous efforts in optimization derived an expression for the scattered fields of a cloaked cylinder, then implemented this expression as a cost functional to minimize scattering. However, to ensure the reduction in scattering was due to cloaking requires the cost functional to account for all observation angles. This angle dependency makes this type of cost functional very inefficient, especially for stratification profiles made of many layers. The solution to this problem is to use a Green's function development to derive the cost functional which is inherently observation angle independent. The development presented here is taken from the publication which was a result of this research [25].

A Green's function provides the unitary response of a system. For the case of an n-layered coated cylinder illuminated by an infinite line source, the Green's function provides the contribution of the line source and the contribution of the scatterer as observed at a given location. If one could design an n-layered cylindrical coating where the contribution due to the scatterer is 0, the result would be a cylindrical cloak. This is because the observer, regardless of position (outside the cloak) and incident angle, will only observe the response due to the source with no evidence of the scatterer. Therefore, the expression for the contribution due to the scatterer can then be used as a cost functional to optimize a cloak

design. This also means that this cost functional will be angle independent and therefore more efficient than accounting for every angle as is seen in literature [51, 54].

Furthermore, the Green's function contains information about the fields within the cloak layer. Of particular interested are the excited surface waves that move in an azimuthal direction along the PEC cylinder, sometimes referred to as creeping waves [19, 23, 43]. These waves are of interest because they are dependent upon the material coating parameters/thicknesses and can have a non-negligible affect on the scattering of a coated cylinder [47].

The Green's function of an n-layered coated cylinder presented in [17, 18] uses a matrix formulation to enforce continuity of the tangential fields. However, for our purposes a matrix formulation is not adequate for two reasons. First, certain geometry and material parameter combinations could create a singular matrix that could hinder the convergence of an optimal solution by the optimization algorithm. Secondly, the propagation constants of the excited azimuthal surface waves correspond to the poles in the Green's function and therefore, access to the denominator is required.

The goal of this section is to create an algebraic expression for the response due to the scatterer for a general stratification profile. The derivation is presented and the duplication of results in literature is presented as validating cases. The expressions derived in this chapter will be used in Chapter 5 to design an optimal isotropic cloak and in Chapter 6 to design and later fabricate an optimal metamaterial cylindrical cloak.

4.1   A Green's Function for an n-Layered PEC Cylinder

The Green's function is presented in [18] and the full derivation can be seen in Appendix B. The relevant geometry is shown in Figure 4.1 and it is important to note that this Green's function assumes that the source and observer will always be outside the stratified media.
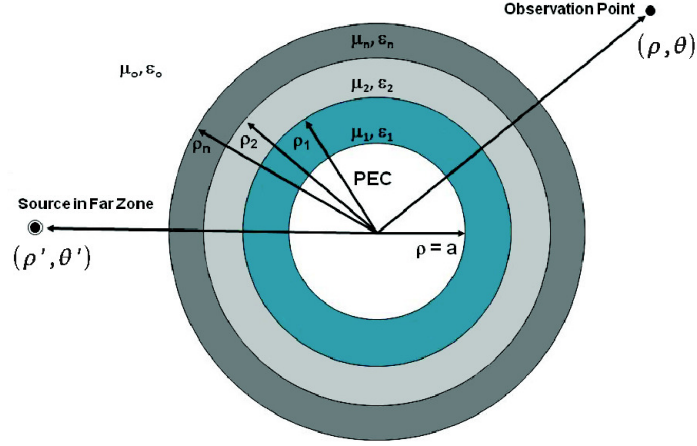
Figure 4.1: n-layered Dielectric Coated PEC Cylinder Geometry [18]

The Green's function is given as (4.1)

$$G = -\frac{j}{4} \sum_{\nu=0}^{\infty} \frac{\epsilon_\nu}{A_\nu^{n+1}} \cos\left[\nu\left(\theta - \theta'\right)\right] \left[A_\nu^{n+1} J_\nu\left(k_0\rho_n\right) + B_\nu^{n+1} H_\nu^{(2)}\left(k_0\rho_n\right)\right] H_\nu^{(2)}\left(k_0\rho'\right) \quad (4.1)$$

$$A_\nu^{n+1} = 1$$

$$B_\nu^1 = -A_\nu^1 K_\nu$$

where ϵ_ν is the Neumann number, $K_\nu = \frac{J_\nu'(k_1 a)}{H_\nu'^{(2)}(k_1 a)}$ for TE incidence and $K_\nu = \frac{J_\nu(k_1 a)}{H_\nu^{(2)}(k_1 a)}$ for TM incidence. There are n layers in this geometry and the superscript of the A_ν^i, B_ν^i variables denotes the associated i^{th} layer. The A_ν^{n+1}, B_ν^{n+1} variables correspond with the free space region outside of the layered cylinder and B_ν^{n+1} is solved through the coefficients A_ν^i, B_ν^i by enforcing continuity boundary conditions of the tangential fields at the layer interfaces. These boundary conditions are

$$\left. E_z \right|_{\rho-} = \left. E_z \right|_{\rho+} \tag{4.2}$$

$$\frac{1}{\mu^-} \frac{\partial}{\partial \rho} \left. E_z \right|_{\rho-} = \frac{1}{\mu^+} \frac{\partial}{\partial \rho} \left. E_z \right|_{\rho+} \tag{4.3}$$

for the TM case and

$$\left. H_z \right|_{\rho-} = \left. H_z \right|_{\rho+} \tag{4.4}$$

$$\frac{1}{\epsilon^-} \frac{\partial}{\partial \rho} \left. H_z \right|_{\rho-} = \frac{1}{\epsilon^+} \frac{\partial}{\partial \rho} \left. H_z \right|_{\rho+} \tag{4.5}$$

for the TE case [5].

In order to solve for A_ν^i, B_ν^i coefficients, boundary conditions are enforced at each interface as seen in Equation (4.6), where $'$ denotes differentiation with respect to the argument of the Bessel function. This results in a system of equations which can be represented as a matrix equation [17], however our goal is an algebraic representation because a matrix representation may become singular through the optimization process.

$$A_\nu^1 \left[J_\nu(k_1\rho_1) - K_\nu H_\nu^{(2)}(k_1\rho_1) \right] = A_\nu^2 J_\nu(k_2\rho_1) + B_\nu^2 H_\nu^{(2)}(k_2\rho_1)$$

$$A_\nu^1 \frac{\kappa_2}{k_1} \left(J_\nu'(k_1\rho_1) - K_\nu H_\nu^{'(2)}(k_1\rho_1) \right) = \frac{\kappa_1}{k_2} \left(A_\nu^2 J_\nu'(k_2\rho_1) + B_\nu^2 H_\nu^{'(2)}(k_2\rho_1) \right)$$

$$A_\nu^2 J_\nu(k_2\rho_2) + B_\nu^2 H_\nu^{(2)}(k_2\rho_2) = A_\nu^3 J_\nu(k_3\rho_2) + B_\nu^3 H_\nu^{(2)}(k_3\rho_2)$$

$$\frac{\kappa_3}{k_2} \left(A_\nu^2 J_\nu'(k_2\rho_2) + B_\nu^2 H_\nu^{'(2)}(k_2\rho_2) \right) = \frac{\kappa_2}{k_3} \left(A_\nu^3 J_\nu'(k_3\rho_2) + B_\nu^3 H_\nu^{'(2)}(k_3\rho_2) \right)$$

$$\vdots$$

$$A_\nu^n J_\nu(k_n\rho_n) + B_\nu^n H_\nu^{(2)}(k_n\rho_n) = J_\nu(k_0\rho_n) + B_\nu^{n+1} H_\nu^{(2)}(k_0\rho_n)$$

$$\frac{1}{k_n} \left(A_\nu^n J_\nu'(k_n\rho_n) + B_\nu^n H_\nu^{'(2)}(k_n\rho_n) \right) = \frac{\kappa_n}{k_0} \left(J_\nu'(k_0\rho_n) + B_\nu^{n+1} H_\nu^{'(2)}(k_0\rho_n) \right) \qquad (4.6)$$

$$\kappa = \begin{cases} \epsilon_r = \frac{\epsilon}{\epsilon_0} & TE \\ \mu_r = \frac{\mu}{\mu_0} & TM \end{cases}$$

4.1.1 Calculating Bessel Functions.

Most efforts in literature have relied on asymptotic forms to calculate the Bessel functions, namely the Debye/Watson [19, 43] or Olver [21, 22, 43, 44] approximations. Accurately calculating the Bessel functions is critical when dealing with a stratified media since any error will be compounded and become greater as the number of layers increases. A numerical approach from [13] was implemented in this effort since it is valid everywhere and claims an error of less than 6.24×10^{-14} in Wronskian tests. Furthermore, this numerical approach is valid for complex mode and argument.

4.1.2   Solving for the Scatterer Contribution.

The Green's function presented in Equation (4.1) is made up of two portions, the response due to the incident field and the response due to the scattered field as seen in Equation (4.7).

$$G_{total} = G_{incident} + G_{scattered} \tag{4.7}$$

The scatterer contribution of the Green's function can be written as

$$G_{scattered} \quad = \quad -\frac{j}{4} \sum_{\nu=0}^{\infty} \epsilon_{\nu} \cos\left[\nu\left(\theta - \theta'\right)\right] B_{\nu}^{n+1} H_{\nu}^{(2)}\left(k_0 \rho_n\right) H_{\nu}^{(2)}\left(k_0 \rho'\right). \tag{4.8}$$

It is apparent from Equation (4.8) that B_{ν}^{n+1} is the angle independent portion of the scatterer contribution which accounts for the layers and material parameters. A general algebraic expression for B_{ν}^{n+1} can yield both a scattering cost functional and the associated azimuthal wave propagation constants. Due to the recursive nature of the boundary conditions in Equation (4.6), a general expression for A_{ν}^{1} of any stratification profile can be derived which can then be used to solve for B_{ν}^{n+1}.

To solve for A_{ν}^{1} in Equation (4.6), begin with the boundary conditions of the inner layer then work towards outer layer until there is a system of 2 equations where A_{ν}^{1} is a function of B_{ν}^{n+1}. This system of equations can then be used to solve for an expression for A_{ν}^{1} and therefore B_{ν}^{n+1}.

To simplify this process, the variables in Equation (4.9) are introduced. These variables are derived from the boundary conditions at the nth layer and free space junction. The ν subscript is used in these variables to denote the dependency on the mode.

$$
\begin{aligned}
D_\nu &= \frac{\pi \rho_n k_n}{j2} \left[\frac{\kappa_n}{k_0} H_\nu^{'(2)}(k_0\rho_n) H_\nu^{(2)}(k_n\rho_n) - \frac{1}{k_n} H_\nu^{'(2)}(k_n\rho_n) H_\nu^{(2)}(k_0\rho_n) \right] \\
E_\nu &= \frac{\pi \rho_n k_n}{j2} \left[\frac{\kappa_n}{k_0} J_\nu^{'}(k_0\rho_n) H_\nu^{(2)}(k_n\rho_n) - \frac{1}{k_n} H_\nu^{'(2)}(k_n\rho_n) J_\nu(k_0\rho_n) \right] \\
F_\nu &= \frac{\pi \rho_n k_n}{j2} \left[\frac{1}{k_n} J_\nu^{'}(k_n\rho_n) H_\nu^{(2)}(k_0\rho_n) - \frac{\kappa_n}{k_0} H_\nu^{'(2)}(k_0\rho_n) J_\nu(k_n\rho_n) \right] \\
G_\nu &= \frac{\pi \rho_n k_n}{j2} \left[\frac{1}{k_n} J_\nu^{'}(k_n\rho_n) J_\nu(k_0\rho_n) - \frac{\kappa_n}{k_0} J_\nu^{'}(k_0\rho_n) J_\nu(k_n\rho_n) \right]
\end{aligned}
\tag{4.9}
$$

This allows us to express the boundary conditions of the last layer from Equation (4.6) in the compact form of Equation (4.10).

$$
\begin{aligned}
A_\nu^n &= B_\nu^{n+1} D_\nu + E_\nu \\
B_\nu^n &= B_\nu^{n+1} F_\nu + G_\nu
\end{aligned}
\tag{4.10}
$$

Next, Equation (4.11) shows the variables which which account for the boundary conditions of the intermediate layers $1 < i < n$, where i is the index that refers to the intermediate layer under examination.

$$
\begin{aligned}
X_\nu^i &= \frac{\pi k_i \rho_i}{j2\kappa_{i+1}} \left[\frac{\kappa_i}{k_{i+1}} H_\nu^{'(2)}(k_{i+1}\rho_i) H_\nu^{(2)}(k_i\rho_i) - \frac{\kappa_{i+1}}{k_i} H_\nu^{(2)}(k_{i+1}\rho_i) H_\nu^{'(2)}(k_i\rho_i) \right] \\
Y_\nu^i &= \frac{\pi k_i \rho_i}{j2\kappa_{i+1}} \left[\frac{\kappa_i}{k_{i+1}} H_\nu^{(2)}(k_i\rho_i) J_\nu^{'}(k_{i+1}\rho_i) - \frac{\kappa_{i+1}}{k_i} J_\nu(k_{i+1}\rho_i) H_\nu^{'(2)}(k_i\rho_i) \right] \\
R_\nu^i &= \frac{\pi k_i \rho_i}{j2\kappa_{i+1}} \left[\frac{\kappa_{i+1}}{k_i} J_\nu(k_{i+1}\rho_i) J_\nu^{'}(k_i\rho_i) - \frac{\kappa_i}{k_{i+1}} J_\nu^{'}(k_{i+1}\rho_i) J_\nu(k_i\rho_i) \right] \\
S_\nu^i &= \frac{\pi k_i \rho_i}{j2\kappa_{i+1}} \left[\frac{\kappa_{i+1}}{k_i} H_\nu^{(2)}(k_{i+1}\rho_i) J_\nu^{'}(k_i\rho_i) - \frac{\kappa_i}{k_{i+1}} J_\nu(k_{i+1}\rho_i) H_\nu^{'(2)}(k_{i+1}\rho_i) \right]
\end{aligned}
\tag{4.11}
$$

This leads to the general form of the ith intermediate boundary conditions as seen in Equation (4.12).

$$
\begin{aligned}
A_\nu^i &= A_\nu^{i+1} Y_\nu^i + B_\nu^{i+1} X_\nu^i \\
B_\nu^i &= A_\nu^{i+1} R_\nu^i + B_\nu^{i+1} S_\nu^i
\end{aligned}
\tag{4.12}
$$

52

Finally, the process is repeated to get A_v^1 from the boundary conditions at the junction between the first and second layers as seen in Equations (4.13), (4.14) and (4.15). The P_v, Q_v variables are derived from the boundary between the first layer and the PEC boundary.

$$
\begin{aligned}
z_n &= j2\kappa_1 \\
z_d &= \pi k_2 \rho_1 \left[\kappa_2 H_v^{(2)}(k_2\rho_1) Q_v - \frac{\kappa_1}{k_2} H_v'^{(2)}(k_2\rho_1) P_v \right] \\
w_n &= j2\kappa_1 \\
w_d &= \pi k_2 \rho_1 \left[\frac{\kappa_1}{k_2} J_v'(k_2\rho_1) P_v - \kappa_2 J_v(k_2\rho_1) Q_v \right]
\end{aligned}
\tag{4.13}
$$

$$
\begin{aligned}
P_v &= J_v(k_1\rho_1) - K_v H_v^{(2)}(k_1\rho_1) \\
Q_v &= \frac{1}{k_1} \left[J_v'(k_1\rho_1) - K_v H_v'^{(2)}(k_1\rho_1) \right]
\end{aligned}
\tag{4.14}
$$

$$
\begin{aligned}
Z &= \frac{z_n}{z_d} \\
W &= \frac{w_n}{w_d}
\end{aligned}
\tag{4.15}
$$

The system of equations for A_v^1 are expressed as Equations (4.16) and (4.17).

$$
A_v^1 = A_v^2 Z \tag{4.16}
$$

$$
A_v^1 = B_v^2 W \tag{4.17}
$$

While the inner and outer boundary conditions in Equations (4.16), (4.17), (4.10) are static in nature, Equation (4.12), containing the intermediate boundary conditions, is dependent upon the number of layers. In an effort to automatically generate expressions A_v^2, B_v^2 of (4.16), (4.17) for any given stratification profile, the recursive nature of the intermediate boundary conditions are leveraged. This can best be seen in the tree diagram

53

shown in Figure 4.2 which is generated from the intermediate boundary condition $A_\nu^2 = A_\nu^3 Y_\nu^2 + B_\nu^3 X_\nu^2$ and substituting every subsequent intermediate boundary condition equation of a 5 layer coated cylinder.

$$A_\nu^2$$

$$Y_\nu^2 \qquad X_\nu^2$$

$$Y_\nu^3 \quad X_\nu^3 \qquad R_\nu^3 \quad S_\nu^3$$

$$Y_\nu^4 \quad X_\nu^4 R_\nu^4 \quad S_\nu^4 Y_\nu^4 \quad X_\nu^4 R_\nu^4 \quad S_\nu^4$$
$$(T) \quad (M) \ (T) \quad (M)(T) \quad (M) \ (T) \quad (M)$$
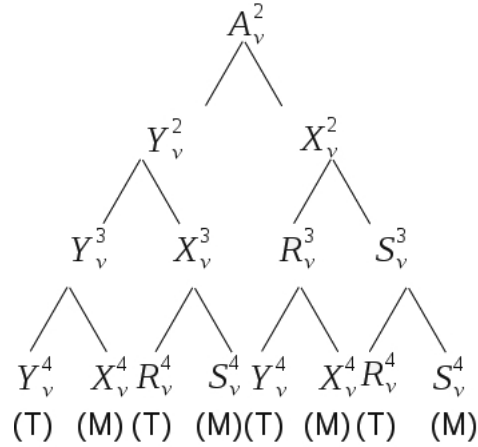
Figure 4.2: Substitution tree of a 5 layer dielectric coated cylinder created by solving for A_ν^2 with the intermediate boundary conditions.

The variables T and M account for the intermediate boundary conditions and are made of the product of the variables along the path from the bottom to the top of the tree. Likewise, a tree generated from the boundary condition $B_\nu^2 = A_\nu^3 R_\nu^2 + B_\nu^3 S_\nu^2$ will generate the variables L and M. The tree diagram is especially helpful in generating the values of T, M, L, N in code.

The variables $T_\nu^n, M_\nu^n, L_\nu^n, N_\nu^n$ are specified as being made of a summation of 2^{n-2} products of $n - 2$ variables. For instance, the expressions for the 5 layered cylinder can be generated from Figure 4.2 and can be seen in Equation (4.18).

54

$$
\begin{aligned}
T_\nu^5 &= Y_\nu^2 Y_\nu^3 Y_\nu^4 + Y_\nu^2 X_\nu^3 R_\nu^4 + X_\nu^2 R_\nu^3 Y_\nu^4 + X_\nu^2 S_\nu^3 R_\nu^4 \\
M_\nu^5 &= Y_\nu^2 Y_\nu^3 X_\nu^4 + Y_\nu^2 X_\nu^3 S_\nu^4 + X_\nu^2 R_\nu^3 X_\nu^4 + X_\nu^2 S_\nu^3 S_\nu^4 \\
L_\nu^5 &= R_\nu^2 Y_\nu^3 Y_\nu^4 + R_\nu^2 X_\nu^3 R_\nu^4 + S_\nu^2 R_\nu^3 Y_\nu^4 + S_\nu^2 S_\nu^3 R_\nu^4 \\
N_\nu^5 &= R_\nu^2 Y_\nu^3 X_\nu^4 + R_\nu^2 X_\nu^3 S_\nu^4 + S_\nu^2 R_\nu^3 X_\nu^4 + S_\nu^2 S_\nu^3 S_\nu^4
\end{aligned}
\tag{4.18}
$$

The superscript and subscript to denote the dependence on the number of layers and order of the Bessel functions respectively. With Equation (4.18), the system of boundary condition equations in (4.10) and (4.12) can be solved to get general expressions of A_ν^2 and B_ν^2 in terms of B_ν^{n+1} as seen in (4.19).

$$
\begin{aligned}
A_\nu^2 &= \left(B_\nu^{n+1} D_\nu + E_\nu \right) T_\nu^n + \left(B_\nu^{n+1} F_\nu + G_\nu \right) M_\nu^n \\
B_\nu^2 &= \left(B_\nu^{n+1} D_\nu + E_\nu \right) L_\nu^n + \left(B_\nu^{n+1} F_\nu + G_\nu \right) N_\nu^n
\end{aligned}
\tag{4.19}
$$

Then, substituting the general form of (4.19) into (4.16) and (4.17) renders a system of 2 equations where A_ν^1 is in terms of B_ν^{n+1}. Due to the form of the boundary conditions, the solution is split into 3 cases: $n = 1, n = 2, n > 2$.

The single layer case can be seen in Equation (4.20) and is identical to the single layer case in literature [24].

$$
B_\nu^2 = \frac{\kappa_1 J_\nu' (k_0 \rho_1) P_\nu - k_0 J_\nu (k_0 \rho_1) Q_\nu}{k_0 H_\nu^{(2)} (k_0 \rho_1) Q_\nu - \kappa_1 H_\nu'^{(2)} (k_0 \rho_1) P_\nu}
\tag{4.20}
$$

The double layer case can be seen in Equation (4.21).

$$
B_\nu^3 = \frac{z_d G_\nu - w_d E_\nu}{w_d D_\nu - z_d F_\nu}
\tag{4.21}
$$

Finally, the expression for the $n > 2$ case can be seen in Equation (4.22).

$$
B_\nu^{n+1} = \frac{z_d \left(E_\nu L_\nu^n + G_\nu N_\nu^n \right) - w_d \left(E_\nu T_\nu^n + G_\nu M_\nu^n \right)}{w_d \left(D_\nu T_\nu^n + F_\nu M_\nu^n \right) - z_d \left(D_\nu L_\nu^n + F_\nu N_\nu^n \right)}
\tag{4.22}
$$

4.1.3 Cost Functional.

As was mentioned earlier, B_ν^{n+1} can be used as an angle independent measure of the contribution energy due to the scatterer for the νth mode in Equation 4.8. Specifically, B_ν^{n+1} is a function of frequency, layer thickness and material parameters. In this dissertation, the free variables are restricted to the layer thicknesses and material parameters at a fixed frequency. The goal of the optimization algorithm is to minimize the cost functional as

$$\min\left\{\sum_{\nu=0}^{\infty}\left|B_\nu^{n+1}(Q)\right| : Q \in \Lambda\right\} \tag{4.23}$$

where Λ is the set of possible solutions. This set of solutions can either be continuous as is the case in Chapter 5 or discrete as is the case in Chapter 6. Constraints must be placed on the optimization algorithm to ensure the solution will be contained within the set Λ. This is particularly important in Chapter 6 where Λ is made of discrete values.

4.2 Validation and Solving for the Azimuthal Surface Wave Propagation Constants

While these general expressions could be used to optimize a cloaked cylinder, they can also be used to study the excited azimuthal surface waves which are central to the study of radiation properties of conformal antennas and scattering of a coated cylinder [1, 19, 24, 43, 44, 47]. The propagation constants of excited azimuthal surface waves correspond with the complex mode ν that causes a pole in B_ν^{n+1}. A pole in a Green's function denotes a source; in this case an impressed current which is associated with an excited surface wave. In this section, some results in literature are duplicated as a way of validating the expressions derived in this chapter. This comparison allows validation of the denominator of our expression. The entire expression was also validated with the results from the matrix formulation from [17].

4.2.1 Method.

The secant method is used, along with an initial guess, to search for the complex roots of the denominator of Equations (4.20), (4.21) and (4.22). Solving for the poles of a

given mode for an n-layer coated cylinder is an incremental process. To ensure the correct pole is identified, the pole of the bare PEC cylinder is solved first. Then, the thickness is incrementally increased, solving for the root at each increment. The subsequent root serves as the initial guess for the next incremental thickness in an effort to track along the same mode. This process can be done for any mode with the first mode associated with the propagation constant that has the smallest imaginary portion (less loss).

4.2.2 Validation Results.

Validation of Equations (4.20), (4.21) and (4.22) were accomplished in two ways. First, multiple test cases are compared using the algebraic expression in Equation (4.22) with the result of the matrix formulation in [17]. Secondly, azimuthal propagation constants of test cases in literature are duplicated.

While the main purpose of this section is to validate the expressions derived in this chapter, the study of azimuthal surface waves may have role to play in optimizing cloaked cylinders. As mentioned earlier, the excited azimuthal surface waves can have a non-negligible affect on the scattering of a coated cylinder. In, [47], it was shown that azimuthal surface waves have a non-negligible contribution to backscatter which is further enhanced as attenuation of the propagation constants is reduced. The azimuthal propagation constant can be expressed as $v = v' - jv''$ where v' is the phase velocity and v'' is the attenuation rate or loss. In literature, it has been shown that the loss in these propagation constants is dependent upon the incident polarization, material parameters of the coating, the size of the structure and the thickness/number of the coatings [1, 19, 23, 24, 43, 44, 47].

In Figure 4.3, a 2 layer structure is assumed. The first layer is held constant at a thickness of $.05\lambda$ and the outer layer thickness increments are plotted with the corresponding real portion of the propagation constant on the x axis and the imaginary portion on the y axis. The results in this data illustrate how the change in layer thickness and material parameters can affect the loss of the propagation constants. Figure 4.4

shows a single layer coated cylinder with incremental thicknesses and corresponding azimuthal propagation constants. The data exhibits excellent agreement between with those in literature. To date, only single and double layer azimuthal wave results have been published. To test the multilayer portion of the general expression, multiple layers were used to make up the single and double layer as a self-validation. Further validation results can be seen in [25].
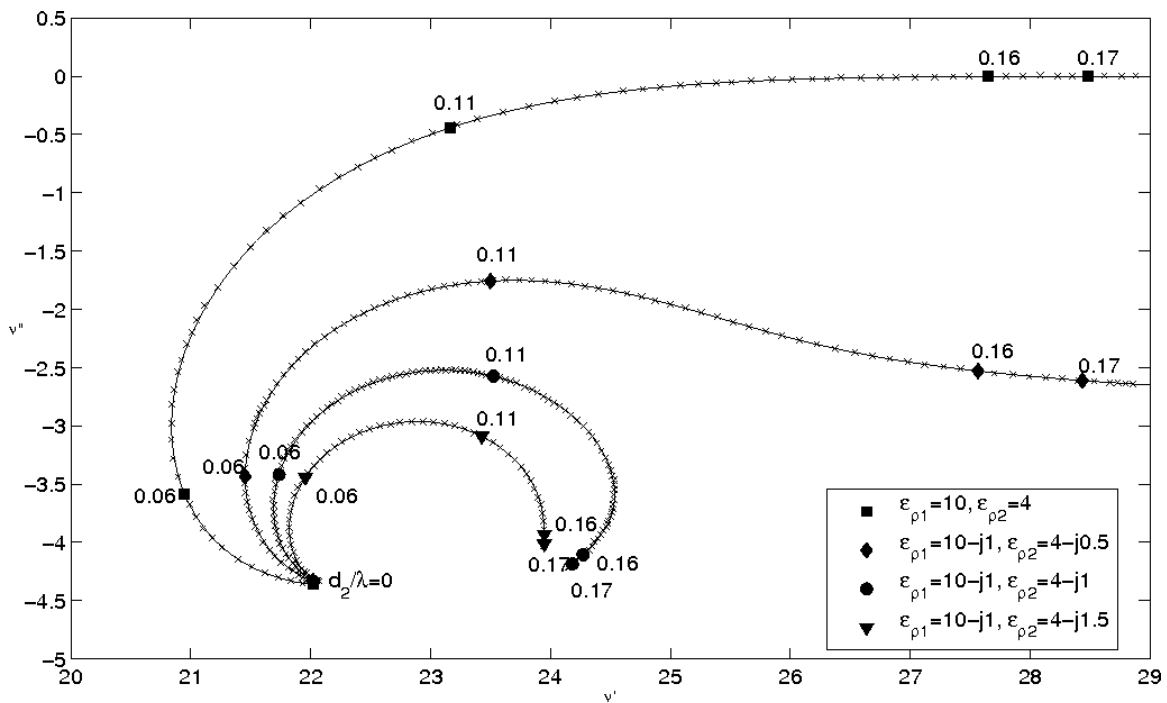
Figure 4.3: TM incidence of 2 layer coated cylinder where $a = 3.1331\lambda$, $\rho_1 = .05\lambda$ and ρ_2 is varied from 0 to $.17\lambda$. The solid lines with dots is our data while the x's signify the data extrapolated from [43].
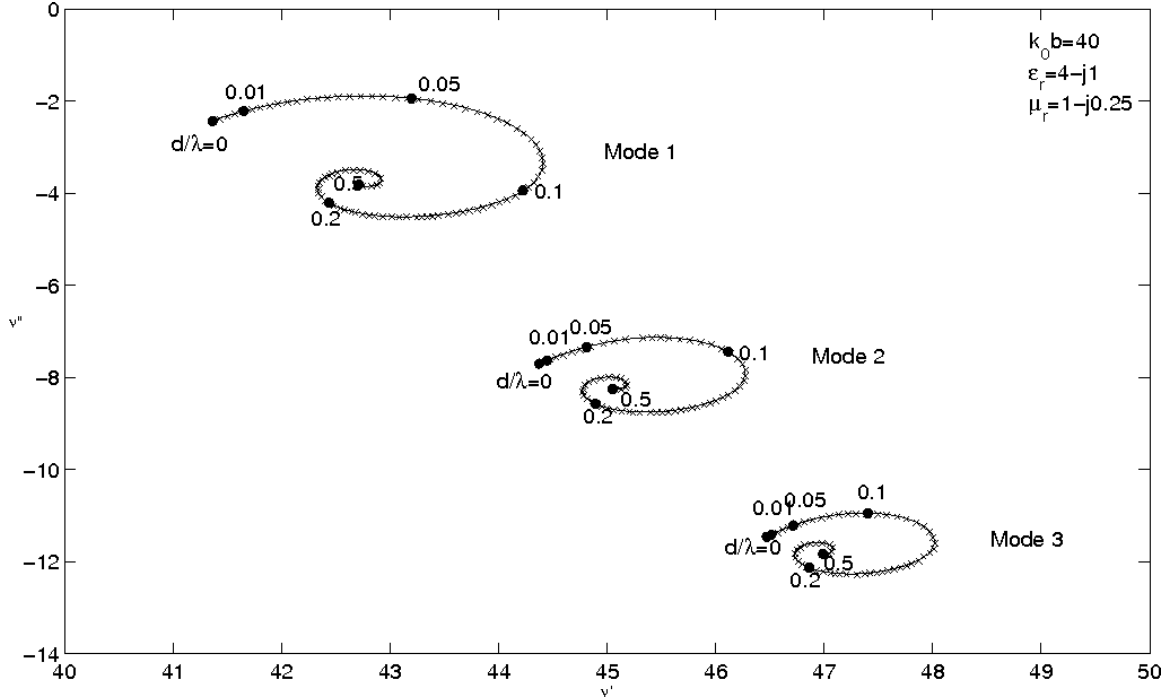
Figure 4.4: TE incidence of 1 layer coated cylinder with $k_0 b = 40$ and $\epsilon_r = 4 - j1$, $\mu_r = 1 - j0.25$. These results show the azimuthal propagation constants with varying thickness of the coating. The solid line with dots is our data while the x's represent the data extrapolated from [44].

4.3   Summary

In this Chapter, an algebraic expression was derived for the contribution due to the scatterer from the Green's function of an n-layered PEC cylinder from [18]. This algebraic expression can be used as a cost functional for optimizing a cylindrical cloak design or to solve for the azimuthal surface wave propagation constants for an n-layered cylinder. In the next chapter, this general expression is used as a cost functional to design and simulate an optimized cloak made from many isotropic layers.

V.   Optimizing a Cloaked Cylinder

In the previous chapter, a cost function for describing the scattering of an n-layered coated PEC cylinder was derived. In this chapter, that cost function will be validated by implementing it to design and study optimized n-layered isotropic cloaked cylinders. While the ideal TO cloak guides waves around a cloaked region solely through a continuous material parameter gradient, the cloaks in this chapter are optimized using the Green's function which accounts for the material parameters, discrete layer thicknesses and the PEC boundary condition at the cloak-cylinder interface. Since the structures in this chapter use the inner PEC boundary condition to cloak, they are more like waveguides than 'traditional' TO cloaks which do not.

The results of optimized cloaked cylinders comprised of 10, 20 and 30 equal thickness layers are presented for both TE and TM cases. In these cases, the geometry is static and only the material parameters are optimized. Additionally, a 10 layer cloak is optimized for the layer thicknesses and material parameters for the TE and TM case.

5.1   Method

In Section 5.2.1, the Nelder-Mead simplex search method implemented in MATLAB is used to perform an unconstrained optimization of the material parameters, assuming layers of equal thickness. This method requires an initial guess and the results are dependent upon this guess. The TO effective medium approximated isotropic values discussed in Chapter 2 serve as the initial guess.

In Section 5.2.2, the cloaked cylinder is optimized for material parameters in addition to individual layer thicknesses. The constrained active-set optimization algorithm implemented in MATLAB is used to ensure valid layer thicknesses (ie $\rho_1 < \rho_2$). The initial guess in this section is made of the optimized results from the previous optimized cloaks

in Section 5.2.1. Regardless of the number of parameters, the optimization algorithm for all test cases in this chapter run until the change in the cost functional is less than 10^{-6}, which is quite small considering the cost functional result for the bare PEC cylinder is $\sum_{\nu=0}^{\infty} \left| B_{\nu}^{n+1} \right| \approx 4.4$.

5.2 Results

In this section, the results for TE and TM incidence are presented for the different optimization test cases. The results of the ideal anisotropic TO cloak, 10 layer TO effective medium isotropic approximation and optimized cloak are compared. To verify this optimization design method, the optimized cloaked cylinders were simulated in COMSOL, a Finite Element Method(FEM) based commercial Computational ElectroMagnetic (CEM) software package.

5.2.1 Optimizing Material Parameters.

In this section, the PEC cylinder radius is $a = 1\lambda$. The outer radius of the entire structure is $b = 2\lambda$ and all of the layers are of equal thickness. The REW simulation data can be seen in Figures 5.1 and 5.2. It is evident that optimizing a cloak with more layers does not change the REW significantly and the performance of the optimized TE and TM cloaks are somewhat comparable in contrast to the simulated ideal TO cloaks. It is also noted that the 10 layer optimized TM cloak can achieve better cloaking performance than the simulated TM ideal anisotropic TO cloak, but the same is not true for the TE case; this will be discussed later in Section 5.2.3. The optimized material parameters were omitted here for brevity, but can be seen in Tables A.1, A.2, and A.3 in Appendix A.
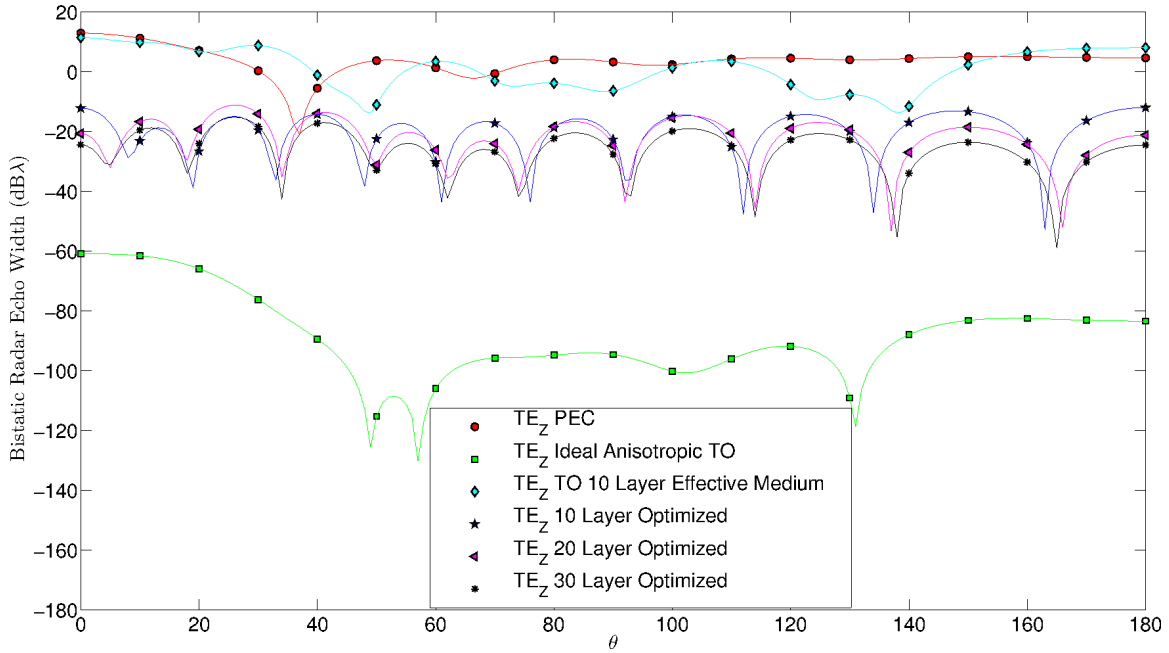
Figure 5.1: REW comparison with TE_z incidence.
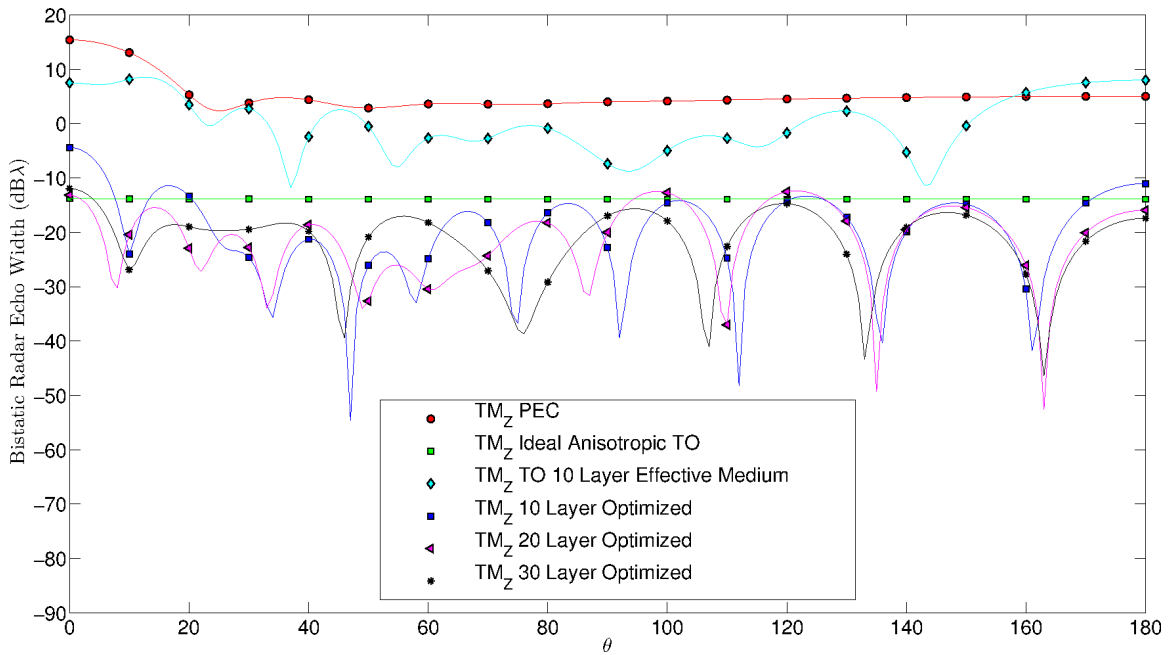
Figure 5.2: REW comparison with TM_z incidence.

5.2.2 *Optimizing Material Parameters and Layer Thicknesses.*

In this next test case, the effects of optimizing material parameters in conjunction with layer thicknesses are studied. The PEC cylinder radius is maintained at $a = 1\lambda$, then the individual layer material parameters and thicknesses are optimized. The sum of the layer thicknesses will dictate the outer radius, b. The initial guess for the test structures in this section is made of the 10 layer geometry and optimized material parameters of Section 5.2.1.

As in the previous section, the optimization results in Tables 5.1 and 5.2 show that the geometry and material parameters for optimal cloaking are quite different between the TE and TM cases. The simulation field patterns can be seen in Figure 5.3 and the corresponding REW plots can be seen in Figures 5.4 and 5.5. These results indicate that optimizing both material parameters and layer thicknesses renders more effective cloaks than through just material parameters alone.

This is expected as demonstrated by the system of equations that are used to solve for the coefficients of the Green's function in Equation 4.6. For convenience, the first and second layer expressions can be seen in Equation 5.1.

$$
\begin{aligned}
A_\nu^1 \left[J_\nu \left(k_1 \rho_1 \right) - K_\nu H_\nu^{(2)} \left(k_1 \rho_1 \right) \right] &= A_\nu^2 J_\nu \left(k_2 \rho_1 \right) + B_\nu^2 H_\nu^{(2)} \left(k_2 \rho_1 \right) \\
A_\nu^1 \frac{\kappa_2}{k_1} \left(J_\nu' \left(k_1 \rho_1 \right) - K_\nu H_\nu^{'(2)} \left(k_1 \rho_1 \right) \right) &= \frac{\kappa_1}{k_2} \left(A_\nu^2 J_\nu' \left(k_2 \rho_1 \right) + B_\nu^2 H_\nu^{'(2)} \left(k_2 \rho_1 \right) \right)
\end{aligned} \tag{5.1}
$$

When only the material parameters are optimized, only a portion of the Bessel function argument and the term $\frac{\kappa_{i+1}}{k_i}$ can be manipulated. However, when layer thickness is added as a free variable, the Bessel function argument can be manipulated somewhat independently to the term $\frac{\kappa_{i+1}}{k_i}$. It is this additional fine tuning to the Bessel function argument that results in more optimal cloaks.

Layer	ϵ_r	μ_r	$\rho(\lambda)$
1	13.2151	0.3580	1.0809
2	0.0165	0.5227	1.0948
3	7.6057	0.5209	1.1826
4	0.1134	2.0364	1.2721
5	5.2840	1.6437	1.3499
6	0.1119	1.7774	1.3973
7	5.3018	1.6098	1.5120
8	0.1134	1.5120	1.5434
9	3.4234	2.0896	1.6009
10	0.5826	0.8274	1.6492

Table 5.1: Optimized material parameters and layer thicknesses for a 10 layer isotropic cloak with TE_z incidence and fixed inner radius $a = 1\lambda$. The outer radius is $b = \rho_{10} = 1.6492\lambda$.

Layer	ϵ_r	μ_r	$\rho(\lambda)$
1	1.0028	6.6475	1.1002
2	1.1884	0.0226	1.1392
3	0.9212	8.6933	1.2481
4	0.9577	0.1493	1.3287
5	1.6500	4.3149	1.4287
6	2.7566	0.0745	1.4908
7	3.0754	4.2868	1.5786
8	1.2093	0.0410	1.5941
9	2.9656	3.1757	1.6625
10	0.2619	0.6178	1.7166

Table 5.2: Optimized material parameters and layer thicknesses for a 10 layer isotropic cloak with TM_z incidence and fixed inner radius $a = 1\lambda$. The outer radius is $b = \rho_{10} = 1.7166\lambda$.
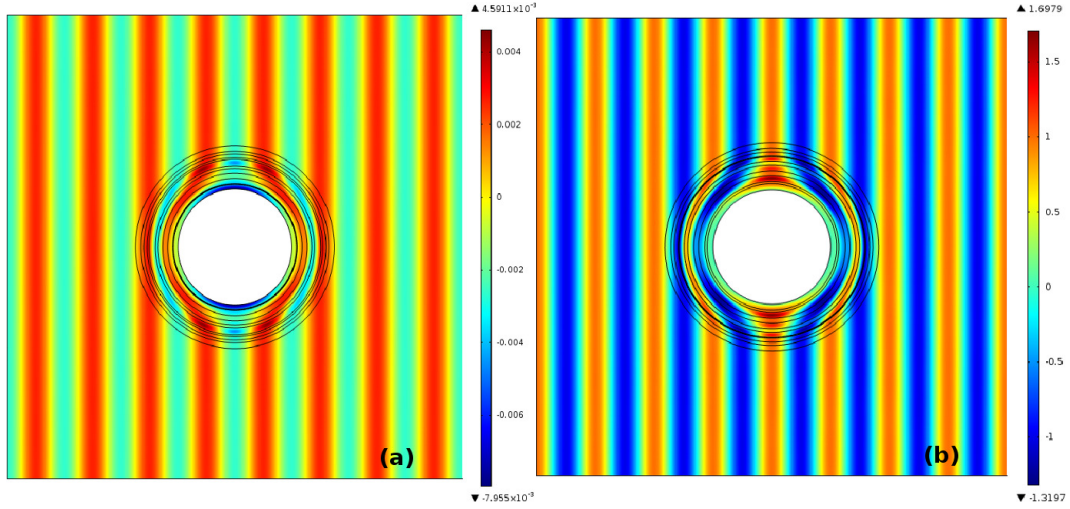
Figure 5.3: $\hat{z}$ directed fields for (a) TE_z and (b) TM_z cloaks with optimal material parameters and layer thicknesses. Power flow is from left to right.
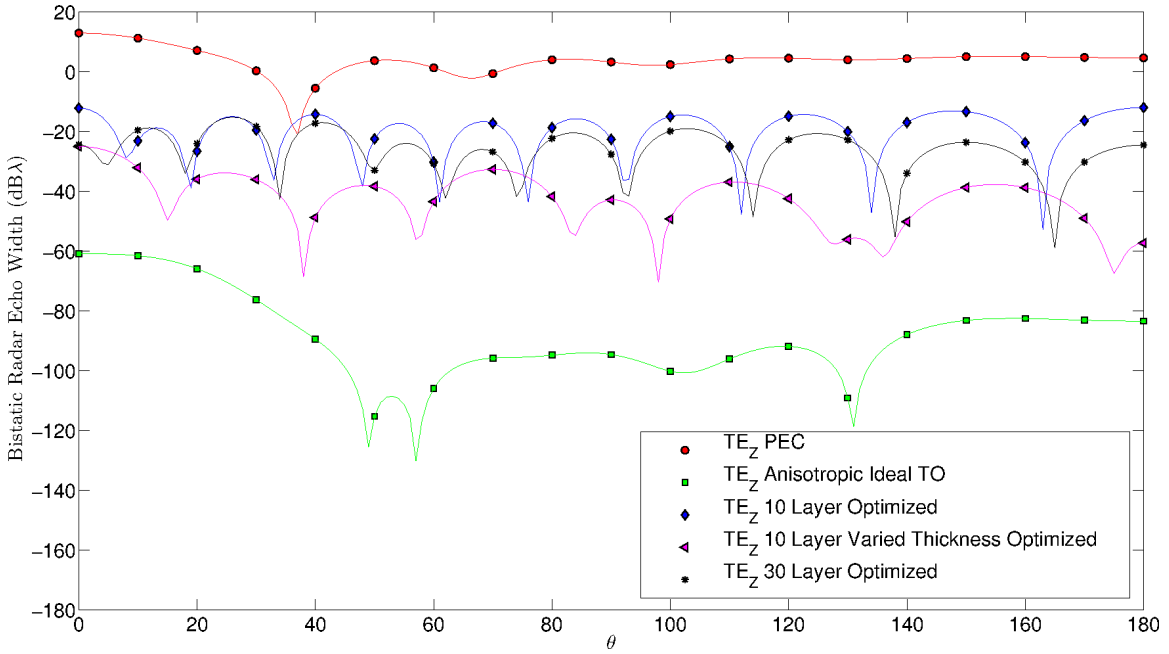
Figure 5.4: REW Comparison between fixed geometry optimized cloaks and a 10 layer cloak with optimized material parameters and geometry for TE_z incidence.

66
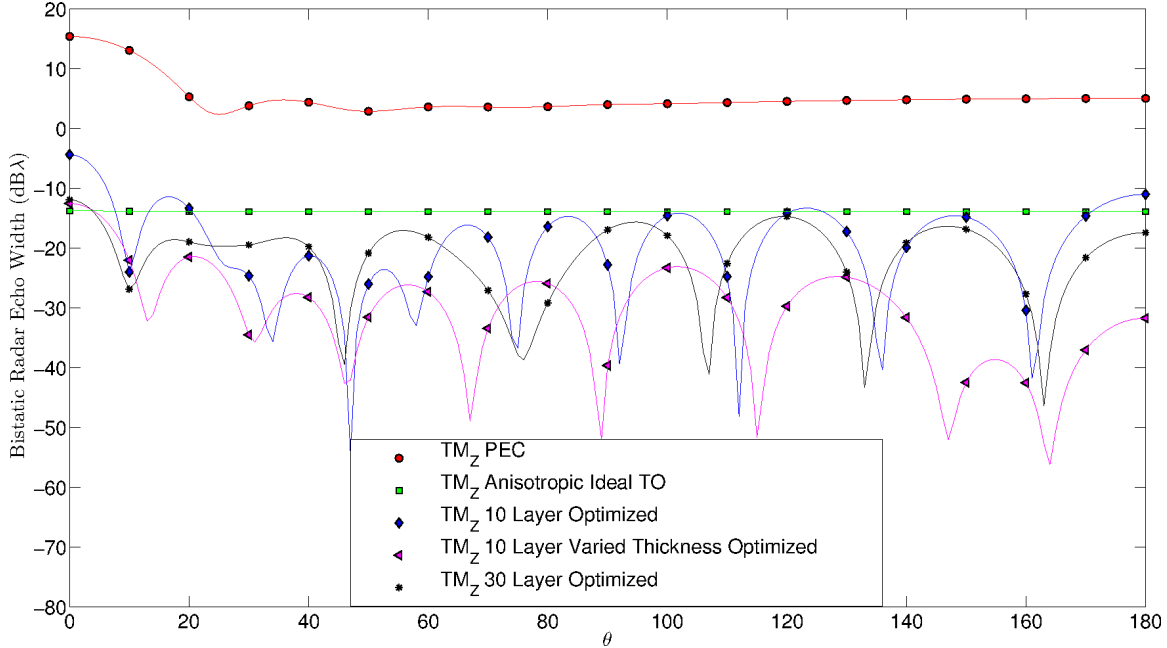
Figure 5.5: REW Comparison between fixed geometry optimized cloaks and a 10 layer cloak with optimized material parameters and geometry for TE_z incidence.

5.2.3 *Further Discussion.*

It is apparent that through optimizing large sets of cylindrical cloak parameters, bistatic scattering behavior of optimized cloaks can potentially rival that of the simulated ideal TO cloaks. It should be reiterated that the simulated ideal TO cloaks do not perform ideally due to the discretization however, the simulated results do allow a case for comparison.

A few observations can be made from the results of the optimized cloaks. First, as noted before, the optimized parameters do not exhibit the dual nature that is dictated by TO cloak design. This is due to the fact that the cost functional takes into account the difference between TM and TE impingement upon a PEC cylinder. When the cost functional is minimized, the interaction with the PEC boundary is used in conjunction with the cloak layers and material parameters to provide all angle reduction of REW. In contrast, the ideal

TO cloak operates purely through the graded material parameters due to its foundation in a coordinate transform. In this regard, the optimized structures presented here are more akin to waveguides than a TO cloak.

Furthermore, it is also noted that the optimized TM cloaks were able to cloak better than the simulated ideal TO cloaks but this was not the case for the optimized TE cloaks. This may be due to the excited azimuthal surface waves. Neither the TO method nor the optimization in this chapter take these surface waves into account when designing a cloak. As the main scattering contribution of the reflected energy is minimized, the contribution of an excited surface waves becomes more dominant. Therefore, it is possible that the differences in the simulated ideal TO cloaks in relation to the optimized cloaks can be attributed to these surface waves.

Also, the lobing nature of the bistatic REW is curious. This seems to indicate a non-negligible effect from excited azimuthal surface waves which affect the backscatter REW of a coated cylinder [47]. Furthermore, the propagation constants of excited azimuthal surface waves are highly dependent upon the stratification profile, material parameters and incident polarization [19, 23, 43, 44]. As such, further study of these waves may provide more insight into the scattering of non-ideal cloaks. It may be possible that an optimization process which takes this into account could surpass the results presented here. However, due to early success of optimizing for material parameters and layer thicknesses, research into the excited azimuthal surface waves was not pursued further and is added as a topic for future research in Chapter 8.

5.3 Summary

In this Chapter, the cost functional of Chapter 4 was validated by implementing it to optimize isotropic cylindrical cloaks for 10, 20 and 30 layers with TE and TM incidence. The optimization process resulted in TM cloaks which surpassed the simulated ideal TM cloak with as little as 10 isotropic layers of equal thickness. The results of these optimized

cloaks indicate that the inherent difference between TM and TE incidence plays a role in these non-ideal cloaks since the optimized material parameters are not duals of each other as is the case with the ideal TO cloak. Most importantly, the ability to optimize large sets of parameters allow for the design and study of optimal isotropic cloaks that can approach the performance of the simulated ideal TO cases. In the next Chapter, this Green's function based optimization approach is implemented to design and fabricate a metamaterial cloaked cylinder.

VI. Metamaterial Design Process for an Isotropic Cylindrical Cloak

The theory and expressions presented in Chapters 4 and 5 are general and as such, are not limited to implementation via metamaterials. In this research effort, metamaterials were chosen to fulfill the material parameters dictated by the optimization process for a few reasons. Primarily, the focus is to study the feasibility of a metamaterial implementation and the validity of the inherent assumptions. Secondly, metamaterials based on metal traces on a PCB substrate are relatively simple to manufacture.

Previous physical cloaks include one based on a geometry of fins of PCB metamaterials pointing radially outward from a conducting cylinder [10] and of concentric rings of PCB metamaterials surrounding a conducting cylinder [36]. Both of these geometries are challenging to fabricate. The ring structure requires spokes, and the fin structure requires the cloak layer be infused with resin so the fins are stabilized as a static structure. Also, both of these previous efforts only made use of a single type of metamaterial unit cell. Contrary to these designs, the goal of this chapter is to design a cloak that is easier to fabricate. Multiple metamaterial unit cells are used to increase the variety of achievable material parameters. Furthermore, while the previously designed physical cloaks were based on the TO method, the cloak presented in this chapter is not.

In this chapter, the design process and fabrication of a disk shaped metamaterial-on-PCB architecture for a 4-layer TE cloaked cylinder is presented. The intent is to determine an optimal cloaked cylinder design for the disk geometry with a predefined set of metamaterial unit cells. Using the design process described in Section 3.5, a set of manufacturable metamaterial material parameter solutions is enumerated. The optimization process of Chapter 5 is then implemented to optimize over this set of manufacturable solutions. The final result is a cloak layer of metamaterial disks that stack around a

70

conducting cylinder. The final structure is 8cm in height made of 14,679 individual metamaterial cells.

6.1   Metamaterial Solutions

While Chapters 5 and 6 provide a relatively unconstrained framework to find optimal cloak solutions, now constraints are required to limit the optimization search to those parameters that are manufacturable. It stands to reason that a larger and more diverse set of possible solutions has a better chance of rendering a more effective cloak. To this end, two different resonant and non-resonant metamaterial unit cells with varying geometries generate the set of possible material parameter solutions. The metal traces are centered on a 3mm x 3mm square of PCB and assume a 2mm space will exist between the metamaterial disks of the final structure. As with the simulations in Chapter 3, the simulation performed in this section assume an infinite slab of one unit cell thickness for extracting material parameters. These cells can be seen in Figure 6.1.
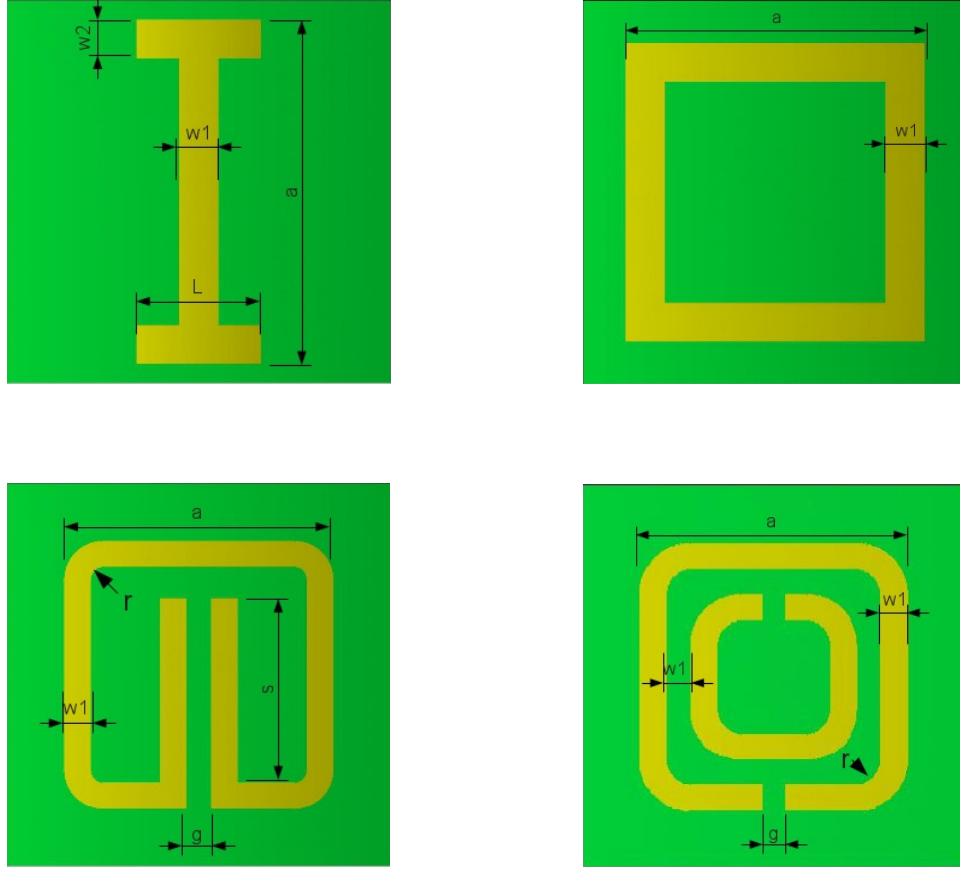
Figure 6.1: Metamaterial unit cells and corresponding geometry of an H cell (top left), square cell (top right), SSRR (bottom left) and DSRR (bottom right). Each cell is centered on a 3mm x 3mm portion of FR4 PCB material. The variables $w1 = g = .2mm$, $w2 = .3mm$ and $a_{SSRR} = 2.1mm$ are static.

A laser engraver is used to fabricate these metamaterial cells on FR4 substrate. The laser engraver burns away the unwanted copper and leaves behind the metal traces of the metamaterial cells. The maximum resolution of the laser etcher is about $40\mu m$ which is then used in the design process to enumerate the possible geometric combinations of the unit cells. This fabrication method chars the PCB material and therefore changes the material parameters of the FR4 substrate. To account for this, a sample of FR4 with the copper completely burned away was measured in a waveguide and the permittivity was measured

as $\epsilon_r = 4.8 - j.35$ at 10GHz. This measured value of permittivity is then used in the design process simulations.

The geometric combinations of the H and square unit cells are not resonant at our target frequency, so the design process for the non-resonant parameters presented in Section 3.5.2 can be used to enumerate the manufacturable material parameters. The SSRR and DSRR must use the resonant models in the design process to enumerate the manufacturable material parameters. However, the design process for the resonant SSRR and DSRR cells was not successful because of a coding error that was not identified until after fabrication. Due to this breakdown in the design process, the geometric combinations of the SSRR and DSRR unit cells were individually simulated to enumerate the manufacturable material parameters. The entire set of manufacturable parameters can be seen in Figure 6.2, where each data point represents a unique geometric combination of the associated unit cell. Although any given geometric combination renders a permeability-permittivity pair, there is no easy way to visualize all of this data in a single graph. Therefore, the plots in Figure 6.2 are useful as a visual aide only. This process resulted in 3,525 physically realizable solutions of permittivity-permeability pairs.
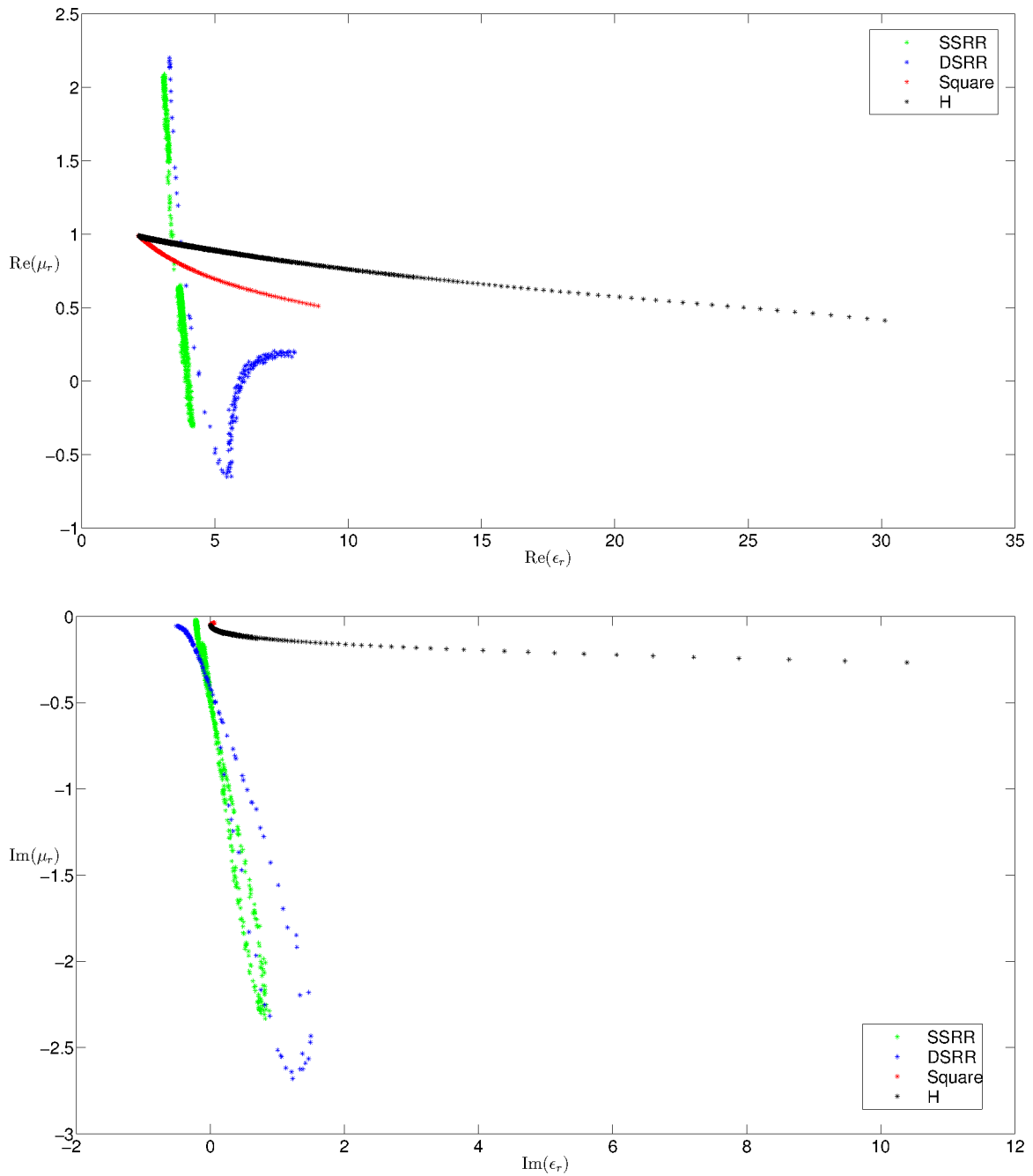
Figure 6.2: Manufacturable permittivity-permeability pairs made from different geometric combinations of the metamaterial unit cells in Figure 6.1 at 10GHz. Each data point corresponds to a unique geometric combination of the until cell.

6.2   Structure Geometry and Assumptions

The next challenge is to determine the assumptions needed to place the 3mm x 3mm unit cells along the circular paths that make up the layers of the cloak. The cloaked cylinder has a cylinder radius of $a = 1\lambda$, an outer radius if $b = 1.8\lambda$. The cloak material is made of 4 layers that are $.2\lambda$ in thickness. Each of these layers is made of 2 rows of a single metamaterial unit cell. Using a design of only 4 layers greatly decreases the time required during optimization. Also, using 2 rows of metamaterial cells for each layer allows for an outer diameter that is close to that used in Chapter 5 to allow some comparison. The final design can be seen in Figure 6.3. These disks will be stacked around a PEC cylinder core. This section discusses the assumptions that allow us to arrive at the final design.
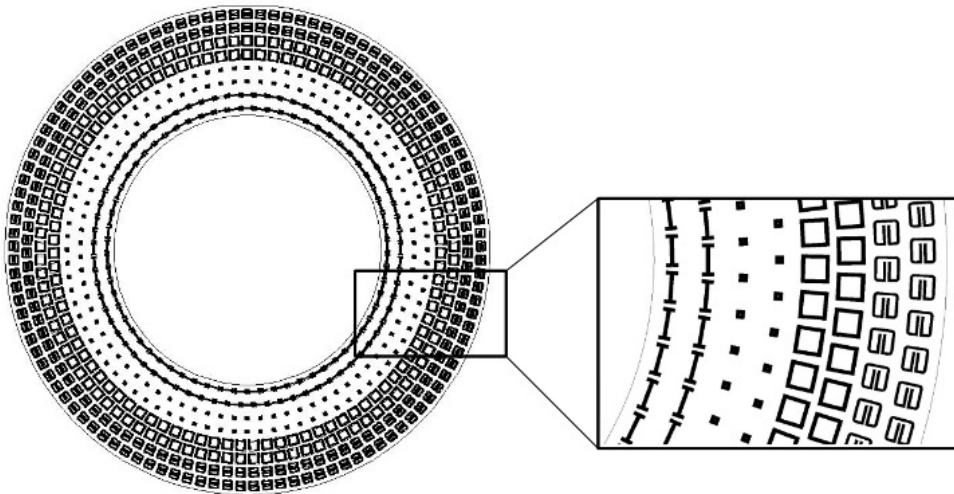
Figure 6.3: Final metamaterial cloaked cylinder design layout.

The most important assumption that will be tested is that the material parameters of an isotropic cloak design can be fulfilled by metamaterials assuming normal incidence. Since the material parameters of metamaterials are anisotropic and dependent on the orientation of the incident field, normal incidence of TE plane waves is assumed. Since the design process is based upon simulations of an infinite sheet of a metamaterial that is one cell deep,

75

coupling in the direction of propagation is not taken into consideration. This assumption will also be tested since there will be some coupling in the direction of propagation that could affect the effective material parameters.

Each of the unit cells simulated in the design process assumes a 3mm X 3mm PCB substrate. Since only an integer number of unit cells can be placed in each concentric ring, the spacing will not be the same as those used in the design process. This will have some effect on the neighbor to neighbor interaction, but the assumption here is that it will be negligible.

6.3   Optimization Process

In this section, the steps of optimization are detailed. The largest problem in optimizing a cloak over the set of manufacturable parameters is that it is difficult to constrain the optimization algorithm to search within a set that are seemingly random. It is possible to constrain an optimization algorithm to search within an upper and lower bounds, but as is seen in Figure 6.2, there are a lot of values within the bounds that are not manufacturable with our selection of metamaterials.

To address this difficulty, a two part quasi brute force optimization approach is used. First, constraints consisting of the upper/lower boundaries and the relationship between the permittivity-permeability pairs of the manufacturable solutions are employed during optimization. The second part involves matching the optimized parameters with the closest manufacturable parameters. Then, a brute force substitution of one layer is used while the other layers are held constant. For each substitution, the cost functional is calculated and the manufacturable parameter pair that results in a minimized cost functional is chosen. This process is repeated for each of the four layers and makes multiple passes until the cost functional value stabilizes. The constrained active-set optimization algorithm included in MATLAB is used in this design process with an initial guess of free space. That is, the material parameters of all four layers are set to $\epsilon_r = \mu_r = 1$ as an initial guess. Therefore,

this cloak is designed completely through the Green's function optimization process and not through the TO method.

6.3.1 Part 1: Optimizing Within Manufacturable Metamaterial Bounds.

The purpose of this portion of the optimization process is to find a set of optimal cloak material parameters within the bounds dictated by the manufacturable solutions in Figure 6.2. In this part of the optimization process, an upper bound and lower bound is used to constrain the possible real and imaginary parameter guesses made by the optimization algorithm. The optimization algorithm is further constrained with relational differences between the possible material parameter pairs. With a matrix constraint equation, the maximum and minimum differences in the material parameter pairs that the optimization algorithm can use can be dictated. As an example, the layer 1 constraint matrix can be seen in Equation (6.1).

$$
\begin{bmatrix}
1 & 0 & -1 & 0 \\
0 & 1 & 0 & -1 \\
-1 & 0 & 1 & 0 \\
0 & -1 & 0 & 1
\end{bmatrix}
\begin{bmatrix}
Re(\epsilon_{r1}) \\
Im(\epsilon_{r1}) \\
Re(\mu_{r1}) \\
Im(\mu_{r1})
\end{bmatrix}
\leq
\begin{bmatrix}
\max\left(Re(\epsilon_r^{manufacturable}) - Re(\mu_r^{manufacturable})\right) \\
\max\left(Im(\epsilon_r^{manufacturable}) - Im(\mu_r^{manufacturable})\right) \\
-\min\left(Re(\epsilon_r^{manufacturable}) - Re(\mu_r^{manufacturable})\right) \\
-\min\left(Im(\epsilon_r^{manufacturable}) - Im(\mu_r^{manufacturable})\right)
\end{bmatrix}
\tag{6.1}
$$

This results in an optimization algorithm that is constrained by the maximum and minimum values of the manufacturable material parameters in addition to the maximum and minimum difference between the manufacturable permittivity-permeability pairs. The optimization algorithm runs until the output of the cost functional changes by less than 10^{-25}. This seems like overkill but ensures the algorithm will continue to run until a minimum is found. The material parameter results of this optimization step can be seen in Table 6.1 and the simulated REW of a cloaked cylinder with these parameters can be seen in Figure 6.4. It is evident that the performance seen in Chapter 5 will not be achieved through this set of manufacturable material parameters. This can be explained by first

noting the material parameter pairs in the optimized 10 layer cloak of Chapter 5, seen in Appendix A. The layers in the optimized 10 layer cloak contained material parameter pairs that alternate which parameter is larger. In our set of manufacturable solutions, permittivity is always larger. This is addressed as an area of further research in Chapter 8.

Layer	ϵ_r	μ_r
1	6.48-j0.3643	0.29+j0.001
2	3.87+j0.7711	0.61-j0.2282
3	10.02-j0.5067	0.31+j0.0049
4	2.25+j0.2926	0.36-j0.1546

Table 6.1: Material parameter results from part 1 of the optimization process.
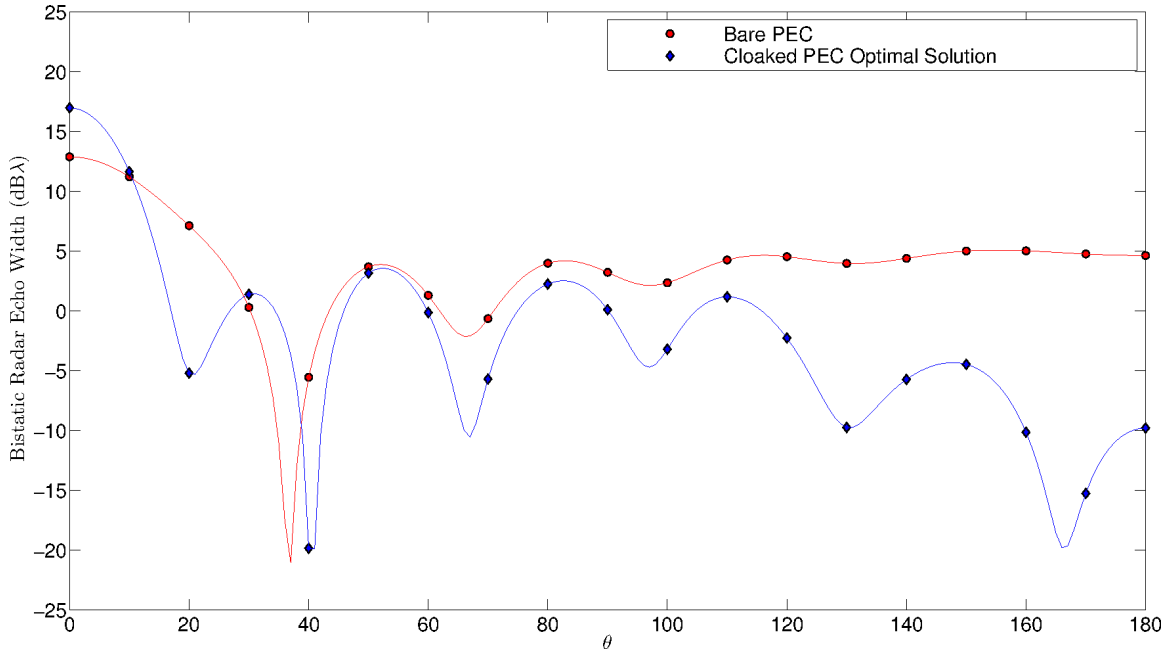
Figure 6.4: REW comparison of simulated infinite cylinder with homogeneous isotropic layer material parameters in Table 6.1.

6.3.2   *Part 2: Matching and Optimizing Individual Layers.*

Once an optimal design is identified within the prescribed constraints, the next step is to find the best material parameter match among the manufacturable material parameters. This is accomplished by comparing the distance (via Pythagorean theorem) between the desired value and all of the manufacturable values, then choose the match with the smallest difference. Once the best match for each of the layers is found, the baseline cost functional for this profile is calculated.

Even though the closest material parameter match is identified, there is no guarantee that the closest match will render a minimized cost functional simply because the closest match is still a deviation from the optimal value. In an effort to ensure the material parameter chosen for each layer renders a minimized cost functional, a brute force search is employed. Each of the possible material parameter pairs is substituted into layer 1 while

the layers 2-4 material parameters are held constant. The cost functional is calculated for every layer 1 substitution and the material parameter pair with the minimum cost functional value is chosen for layer 1. This is accomplished for each layer in turn and multiple passes through all four layers is performed until the cost functional value stabilizes. This required 8 passes which were performed within a 24 hour period using an 8-core workstation. The final values and metamaterial cell geometries can be seen in Table 6.2. It should be noted that all 4 layers of metamaterials in this table are functioning in their respective non-resonant regions which means the respective parameters will not change much as frequency changes. The REW simulation results can be seen in Figure 6.5.

Layer	ϵ_r	μ_r	Cell Type	Geometry(mm)
1	4.77+j0.0384	0.90-j0.0684	H	a=2.7, L=.97
2	2.15+j0.0005	0.99-j0.0491	Square	a=.7
3	4.69+j0.0191	0.7167-j0.0442	Square	a=2.34
4	3.72-j0.2200	0.633-j0.0277	SSRR	s=1.45, r=.1

Table 6.2: Material parameter results from part 1 of the optimization process.
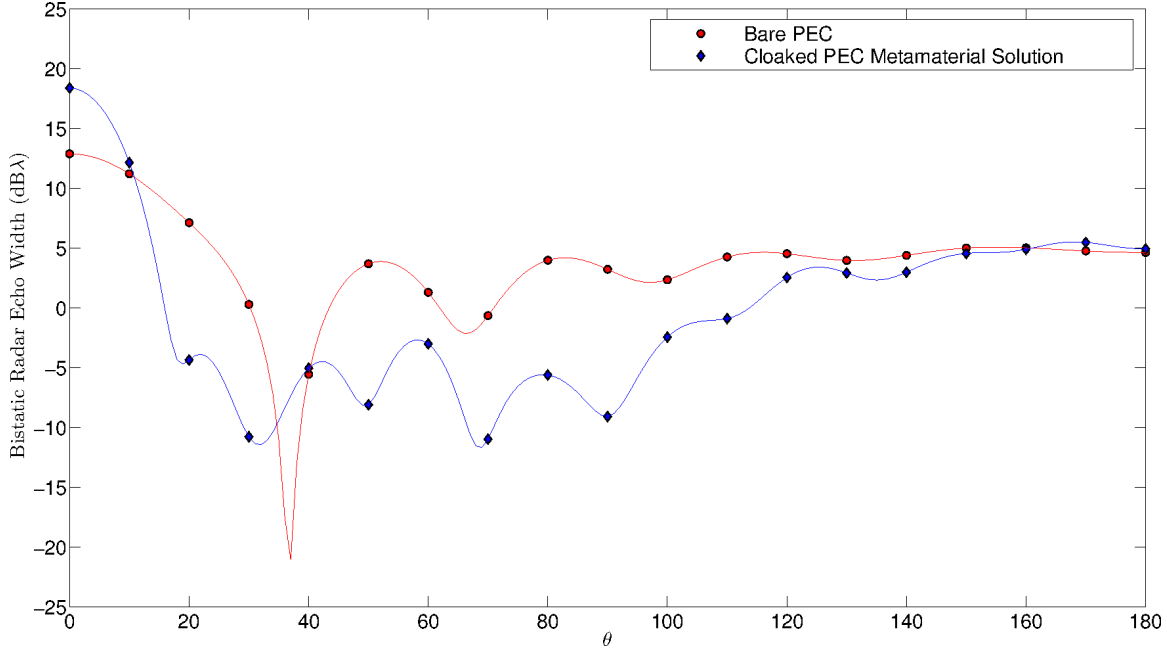
Figure 6.5: REW comparison of simulated infinite cylinder with homogeneous isotropic layer material parameters in Table 6.2.

6.3.3 *Metamaterial Cloaked Cylinder Simulation Results.*

The 2D REW simulation data in the previous section assumed homogeneous isotropic materials. However, since metamaterials are neither homogeneous nor isotropic, a simulated metamaterial cloak will show how well the 2D homogeneous isotropic simulation can predict the 3D metamaterial implementation. In terms of simulation, this is quite a bit more challenging since we are now simulating a 3D space and each metamaterial cell must be meshed, which translates to larger problem sizes and requires more time and system memory. Because of this, the simulated metamaterial cloak is assumed to be infinite in length, so only one disk (see Figure 6.3) must be meshed. We do this by applying a Perfect Magnetic Conductor (PMC) to the top and bottom of the simulation space to account for field coupling in the $\hat{z}$ direction.

The height of one disk includes the thickness of the FR4 substrate as well as the 1mm spacer on top and bottom giving this simulated cloak a height of 2.787mm. However, this was still too large of a problem, so symmetry in the y-direction is assumed. This isn't entirely true since the metamaterial cloak is not symmetric across the y=0 axis, but this should give a reasonable idea of the cloaking effectiveness. Note also that since we are examining a 3D structure we use RCS as a measure of cloaking effectiveness instead of the 2D REW. The $\hat{z}$ directed field patterns of the simulated metamaterial cloak and bare PEC can be seen in Figure 6.6.
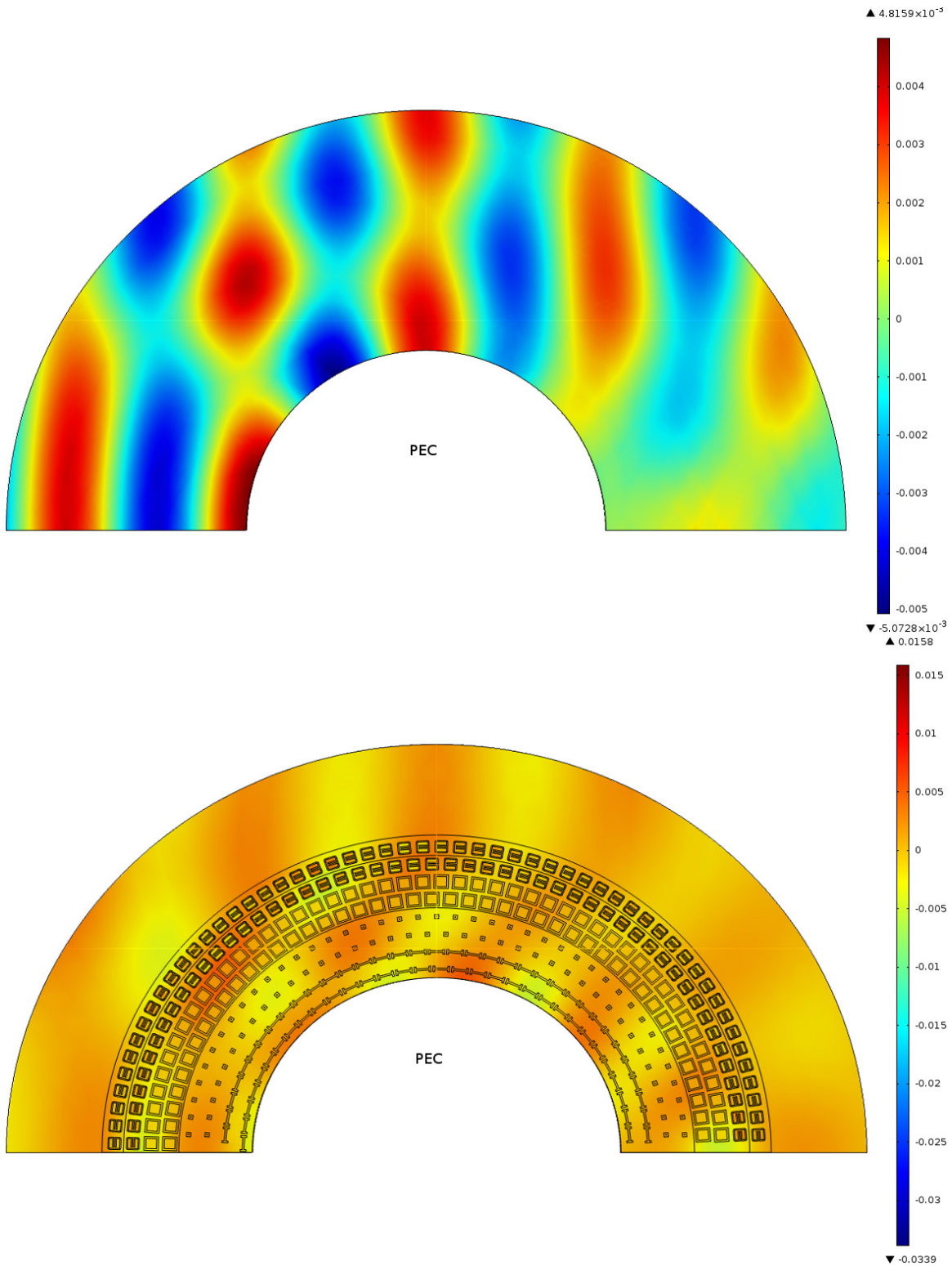
Figure 6.6: $\hat{z}$ directed magnetic field for bare PEC cylinder (top) and metamaterial cloaked cylinder (bottom) at 10GHz. Power flow is from left to right.

The field pattern of the metamaterial cloak does exhibit field bending in the cloak layer, but we must turn to the RCS characteristics to compare the scattering of the bare PEC and the metamaterial cloak which can be seen in Figure 6.7. The RCS plots of the metamaterial cloaked cylinder in Figure 6.7 show similar behavior to that of the REW of the isotropic homogeneous cloaked cylinder from Figure 6.5.
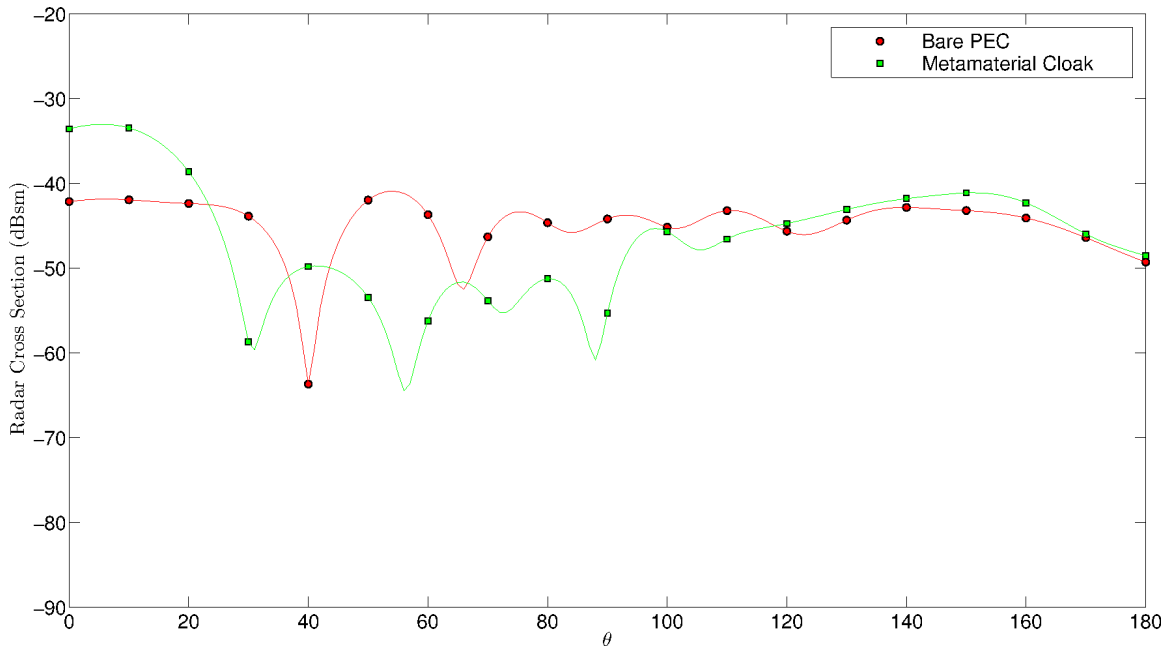
Figure 6.7: RCS of simulated metamaterial cloaked cylinder and bare PEC cylinder of 2.787mm height and at a frequency of 10GHz.

Since this structure is based on metamaterials which are dependent upon frequency, it is important to determine how this cloak performs across the frequency range. Although this cloak was designed for 10GHz, the geometry of the metamaterial cells was constrained to the maximum precision of the fabrication process. This resulted in a 'best fit' geometry for this frequency. It is certainly possible that this structure will be a more effective cloak at a different frequency since the material parameters of our 'best fit' metamaterial geometry

and overall structure size are functions of frequency (wavelength). The data in Figure 6.8 shows bistatic RCS of the bare and cloaked cylinders across the frequency range of 5GHz-15GHz. From this data, it is evident that the metamaterial cloak increases the forward scatter for every frequency in this range, but does show some frequencies where the RCS is noticeably reduced over multiple bistatic angles. In particular, the bistatic RCS near 10GHz and 8GHz stand out.
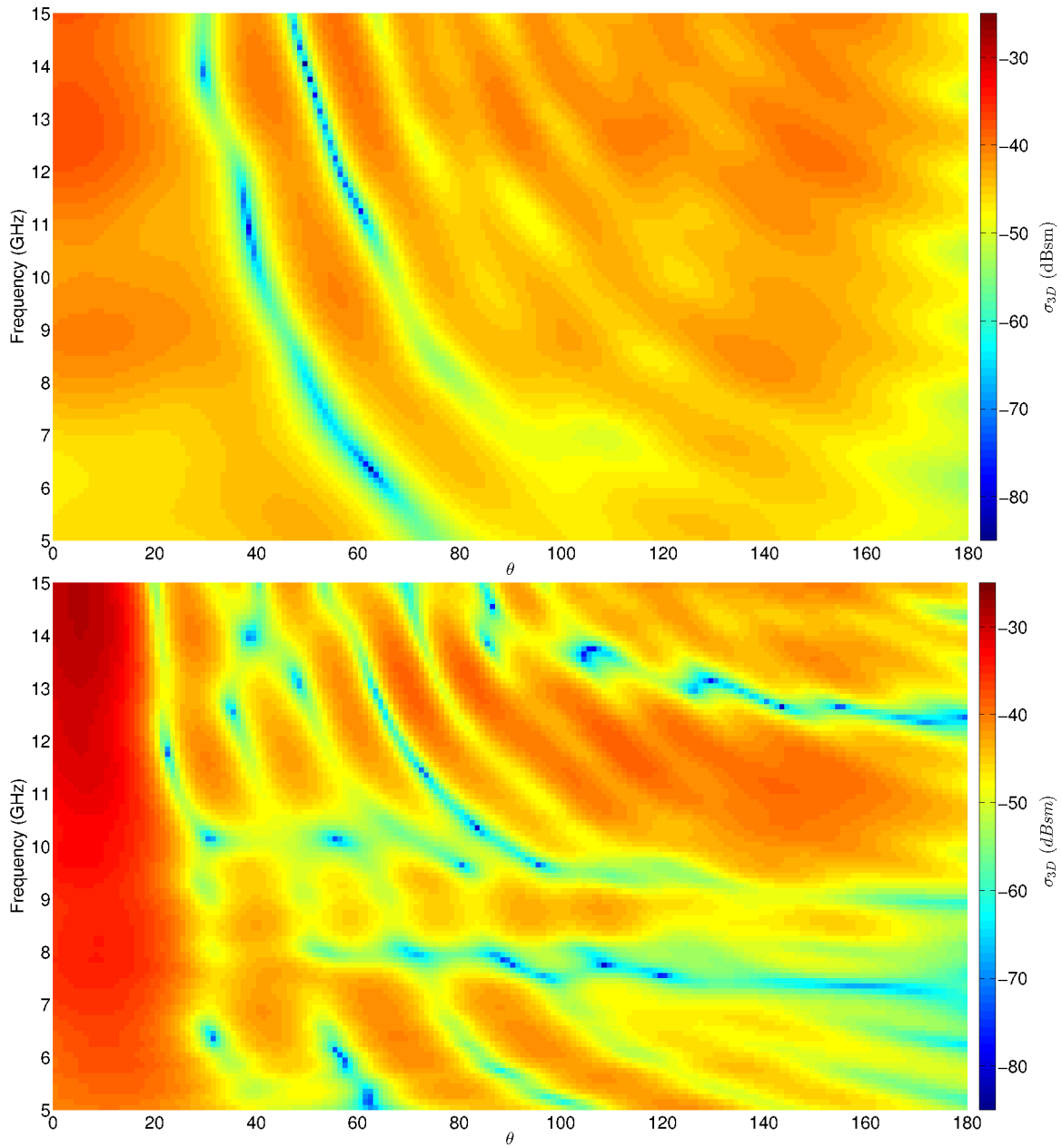
Figure 6.8: Bistatic RCS for the frequency range 5GHz-15GHz of the simulated bare PEC(top) and metamaterial cloaked cylinder(bottom) of 2.787mm height.

In the next section, the fabrication process is explained. The geometry of the final structure is then measured and simulations of the 'as fabricated' cloak are performed to give a baseline to compare with the measured experimental data presented in Chapter 7.

6.4   Structure Fabrication

The simulations of the metamaterial cloaked cylinder portray the effectiveness of an ideally manufactured metamaterial cloak. Any manufacturing process will introduce deviations from this ideal and need to be examined in order to account for any differences between the ideal simulation and real world measurements. In this section, the manufacturing process is explained and examined for possible deviation from the ideal simulation.

6.4.1   Method.

The PCB material is FR4 which is .787mm thick and has a layer of .5oz copper cladding. An EpilogLaser 30W laser engraver is used to create the metamaterial features and to cut out the cloak disks. The CAD layout of our structure is sent to the laser engraver which acts like a printer and burns away the unwanted copper. Determining the proper power/speed settings is an iterative process and these settings do affect each other. For example, a reduction of speed equates to the laser impinging a certain area for a longer amount of time which would require fine tuning of the power and frequency settings. In the end, the settings in Table 6.3 were used for both etching the metamaterials and cutting out the disks.

Etching			Cutting	
dpi	1200		dpi	1200
type	raster		type	vector
speed	10%		speed	35%
power	75%		power	90%
frequency	36		frequency	26

Table 6.3: EpilogLaser laser engraver settings for etching the metamaterials and for cutting out the disks.

With these settings, accurate features could be created but resulted in some charring to the FR4 substrate which does affect the material parameters as was stated previously. The underlying assumption here is that the charring effects of the laser etching are uniform throughout the FR4. However, this is ultimately a function of the laser focus since the amount of material removed by the laser is dependent upon the focus. To ensure the PCB is as flat as possible, it is secured to the laser engraver with tape and weights. Any manufacturing defects of the PCB or copper cladding thickness could also contribute to inconsistent laser etching properties.

Once the disks are etched and cut out, the edges are lightly sanded to make a smooth surface. The last step in this process was to wash the disks with acetone to remove any debris. After cleaning the disks, the cloak can be constructed. The foam spacers are cut out by hand using one of the disks as a template.

When constructing this cloak, it is important that the metamaterials line up in the $\hat{z}$ direction. To aid in this alignment, a flat line was designed into the outer circumference of the disk as can be seen at the top of the layout in Figure 6.3. Once the disks and foam are stacked and properly aligned, a piece of flexible copper clad PCB is cut and shaped into a

cylinder to fit within the disks. Copper tape was used to cover the joining edges of the PCB cylinder. Lastly, dielectric tape is used to secure the structure.

To ensure an accurate comparison with a bare cylinder, an identical length of flexible PCB is cut and wrapped around a foam core to simulate the PEC cylinder in the cloak structure. The joining edge in the bare cylinder is also taped with copper tape. While, this creates a reasonable comparison object, neither the bare cylinder or the cylinder in the cloak structure are perfect cylinders.

6.4.2 Results.

The final cloak structure and individual disk can be seen in Figure 6.9. A microscope was used to verify the individual metamaterial geometries and to spot any manufacturing abnormalities; this can be seen in Figure 6.10. The scalloped edges are due to the diameter of the laser and the lack of right angles is also evident in the H cell. These deviations from the ideal design are not expected to cause a significant difference.
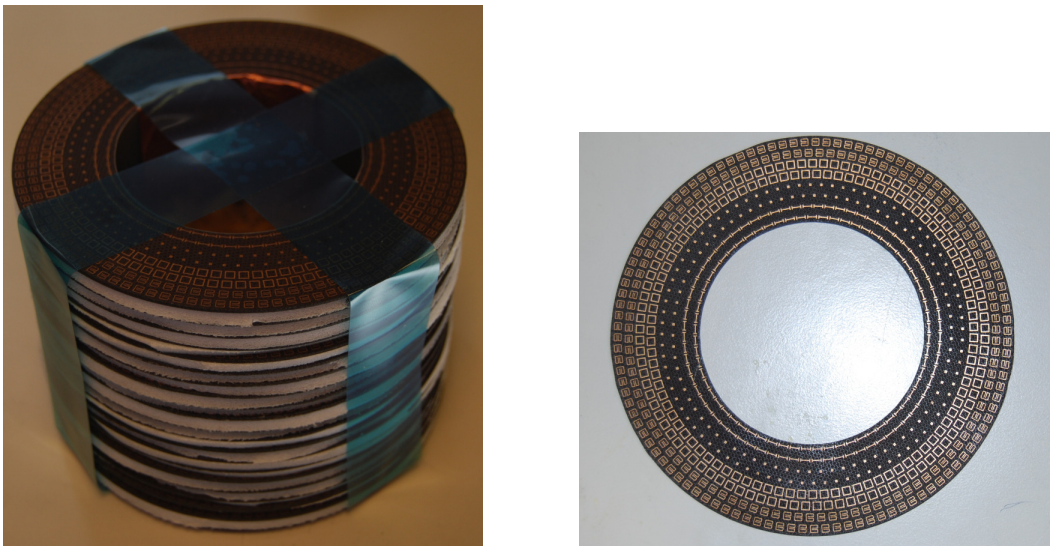
Figure 6.9: Constructed cloaked cylinder.
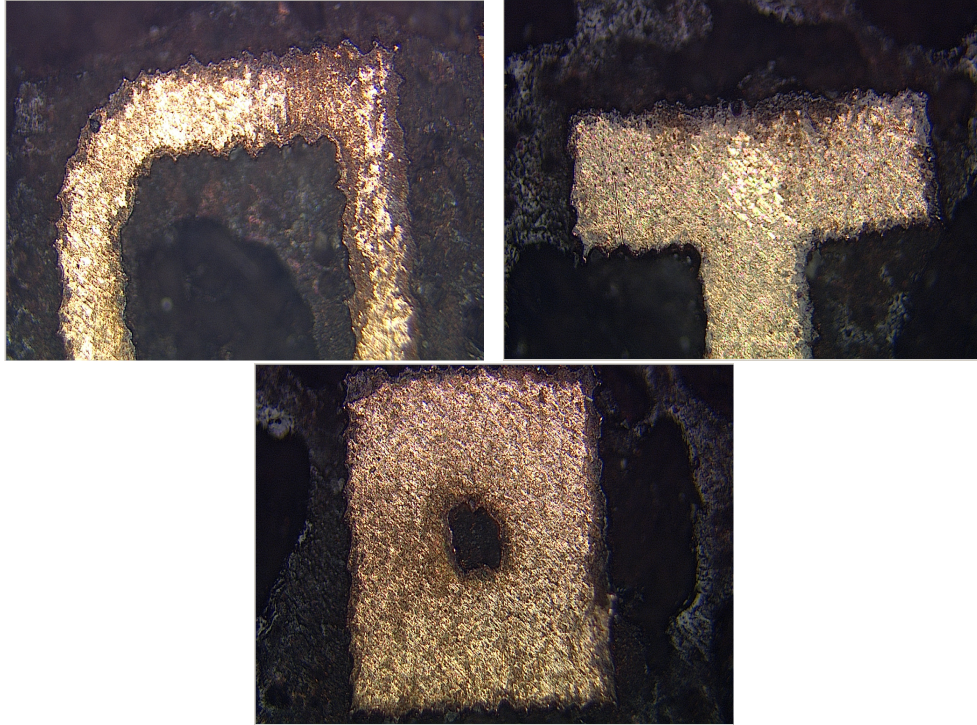
Figure 6.10: Microscope images of the metamaterial structures on the cloak disks.

6.4.3 Simulations as fabricated.

After the cloak was constructed, the foam was measured to determine the thickness. The foam implemented in this structure is thicker than the 2mm designed for, but it was unknown how much compression would occur after construction. The foam was measured to be 3.1mm which is a lot thicker than the initial design requirement. Due to this deviation, the simulated results are reaccomplished with this 'as fabricated' spacing change. The single layer metamaterial cloak is simulated and compared with the same size bare PEC cylinder. The individual metamaterial cells are also simulated to see what effect this spacing change will have on the material parameters.

The metamaterial parameters with the new 'as fabricated' spacing are presented in Table 6.4.

Layer	ϵ_r	μ_r	Cell Type	Geometry(mm)
1	3.8222 - j0.2696	0.9240 + j0.0059	H	a=2.7, L=.97
2	1.8276 - j0.0772	0.9925 + j0.0002	Square	a=.7
3	3.7167 - j0.2144	0.7761 + j0.0028	Square	a=2.34
4	2.9803 - j0.1564	0.6965 - j0.0230	SSRR	s=1.45, r=.1

Table 6.4: Metamaterial parameters with 'as fabricated' spacing.

The simulated isotropic homogeneous REW using the values in Table 6.4 can be seen in Figure 6.11. The 3D field patterns of the bare PEC and metamaterial cloak can be seen in Figure 6.12 and the associated RCS plot in Figure 6.13.
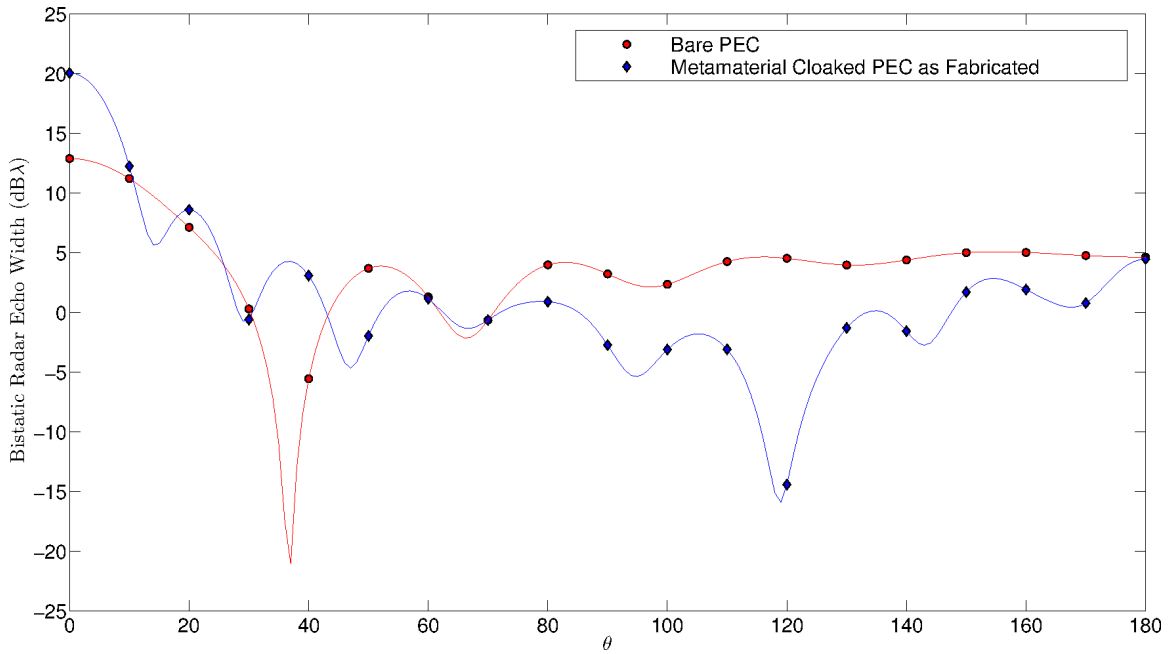
Figure 6.11: REW comparison of simulated infinite cylinder with homogeneous isotropic layer material parameters in Table 6.4.
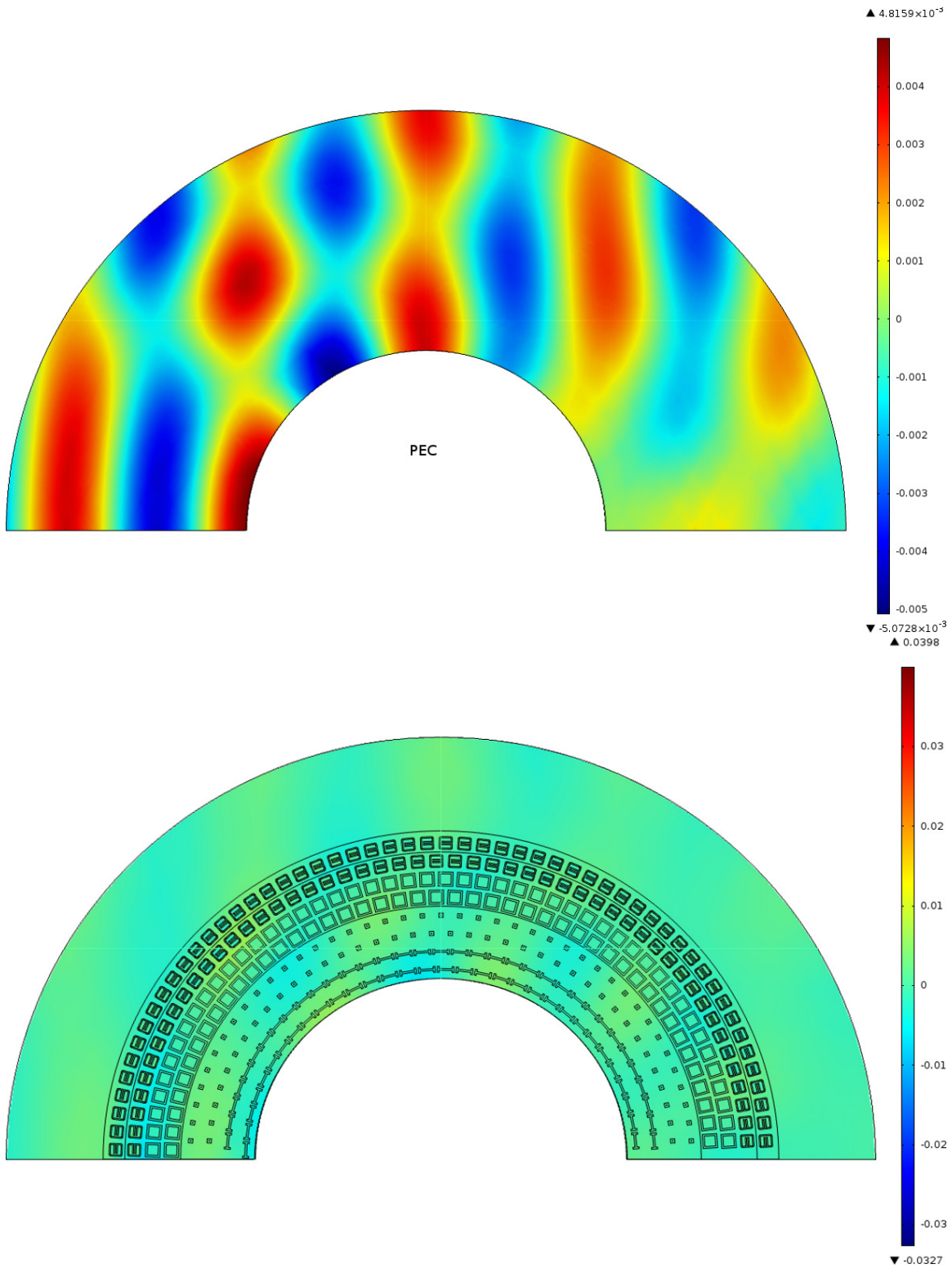
Figure 6.12: $\hat{z}$ directed magnetic field for bare PEC cylinder (top) and metamaterial cloaked cylinder as fabricated (bottom) at 10GHz. Power flow is from left to right.
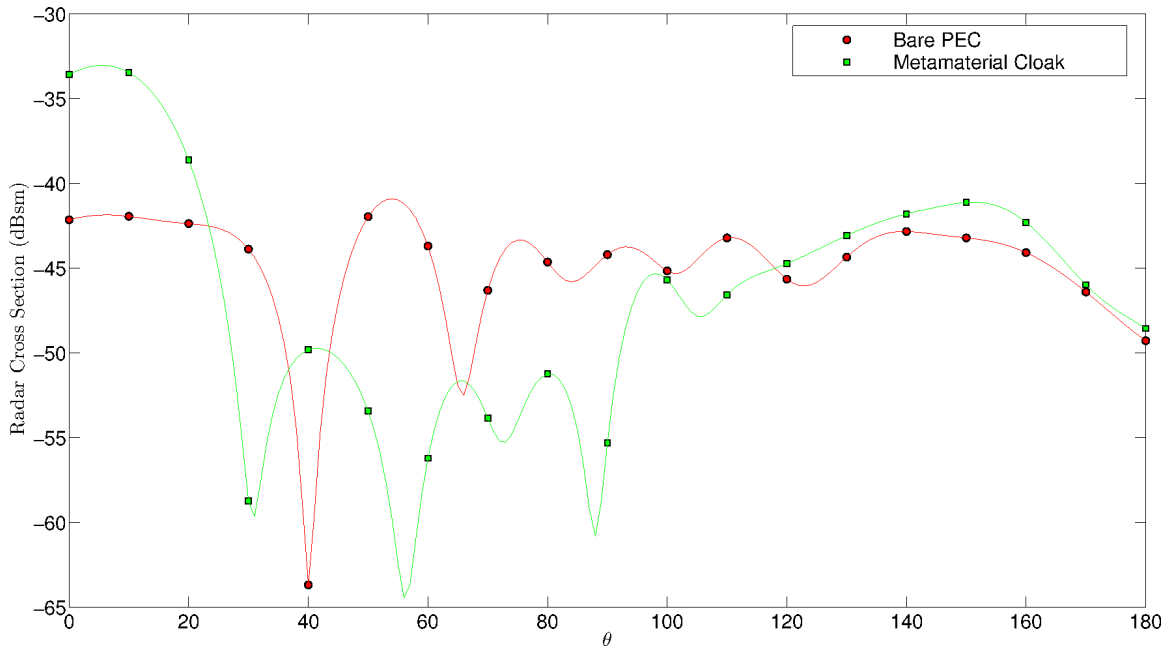
Figure 6.13: REW of simulated infinite metamaterial cloaked cylinder and bare PEC cylinder at 10GHz.

Lastly, the bistatic RCS across the frequency range 5GHz-15GHz for the bare and cloaked cylinder with the 'as fabricated' dimensions can be seen in Figure 6.14. As expected, this data shows a degradation in performance from the cloak with the original dimensions.
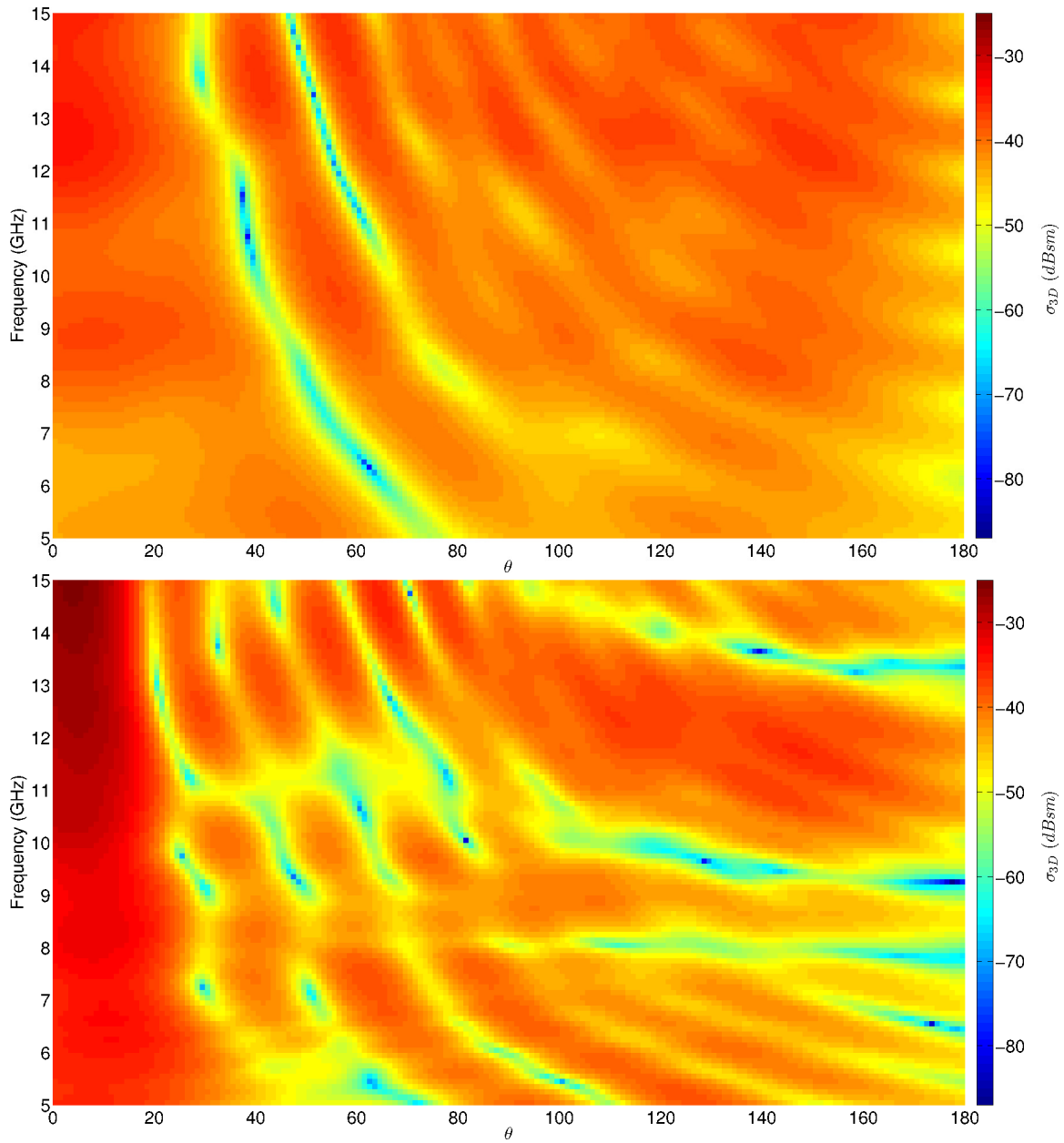
Figure 6.14: Bistatic RCS for the frequency range 5GHz-15GHz of the simulated bare PEC(top) and metamaterial cloaked cylinder(bottom) with the as fabricated height of 3.887mm.

6.5 Summary

In this chapter, the process to design and then fabricate a metamaterial cloaked cylinder was presented. The framework laid by the previous chapters was used to optimize cloaking performance over a set of manufacturable material parameters generated by a set of metamaterials. The finalized design was then fabricated, geometry was verified and simulations updated with the 'as fabricated' geometry. While data in this chapter are all based on simulations, the next chapter presents the experimental RCS measurements taken at the AFIT indoor radar range.

VII. Experimental RCS Measurements

In Chapter 6, an optimal metamaterial cloak was designed, fabricated and simulated. In this chapter, the experimental RCS measurements of the metamaterial cloak are presented. The method of calibration and error associated with both the bistatic and monostatic measurements are also described. In the end, the simulated 2D Green's function isotropic optimization results of Chapter 6 are a reasonably accurate predictor of the performance of the physical metamaterial cloaked cylinder.

7.1 Experimental Measurement Results

Measurements of the fabricated cloaked cylinder were taken at the AFIT indoor radar range as seen in Figure 7.1. This range has the ability to perform both bistatic and monostatic measurements. In this section, the method of calibration and measurements are explained. Finally, the monostatic and bistatic measurements of the metamaterial cloaked cylinder and bare PEC are presented.
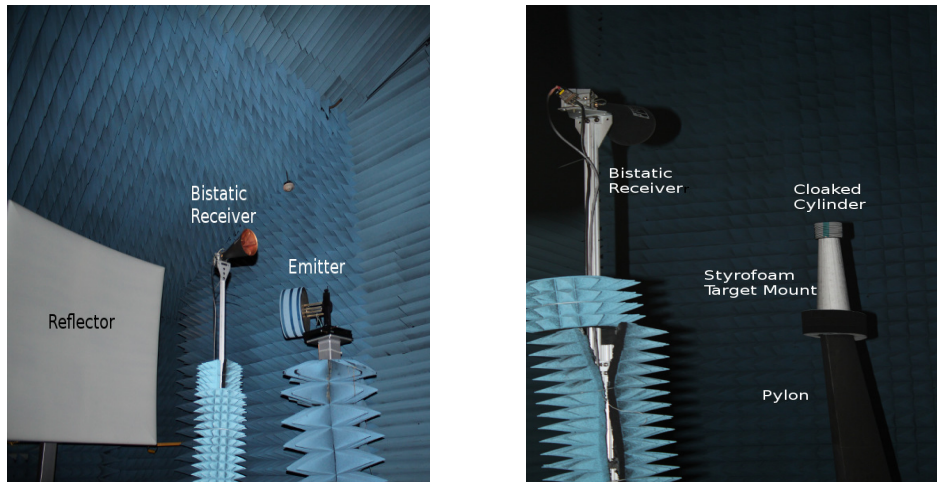
Figure 7.1: AFIT radar range setup. The energy from the emitter is reflected to create plane wave illumination. The bistatic receiver is mounted on an arm that revolves around the target pylon.

7.1.1 *Calibration and Measurement Method.*

Calibration is critical in taking accurate RCS measurements. Calibration allows for the extraction of the fields scattered by the target from the measured data and determines what post-processing correction is needed. Time delay gating is used in addition to measurement data of the empty range and two calibration cylinders to calibrate and correct the measured target data. Two calibration cylinders that are commensurate in size to the cloak are used and can be seen in Figure 7.2. This allows us to get an accurate error analysis of objects near this size. The two calibration cylinders have a 450mm radius and a 375mm radius. Throughout this chapter they are referred to as the 450 and 375 calibration cylinders.

The expression used for calibration is seen in Equation 7.1. This expression removes the background clutter, then applies a correction factor which is based on the relationship between the measured calibration cylinder data and the exact calibration cylinder solution.

Figure 7.2: In order from left to right is the cloaked cylinder (540mm radius), bare cylinder (300mm radius), 450mm radius calibration cylinder and 375mm radius calibration cylinder.

$$\sigma_{3D}^{calibrated} = \left[\frac{CalCyl_{exact}}{CalCyl_{measured} - Background_{measured}} \right] (Target_{measured} - Background_{measured})$$

(7.1)

The calibrated data can be verified by using the measurements of one calibration cylinder to calibrate the measured data of the other calibration cylinder. That is, one calibration cylinder serves as the $Target_{measured}$ and the other serves as the $CalCyl$. This calibrated measurement is then compared with the exact solution to determine the error in the measurements. This calibration must be done for each measurement because measurement data can drift over time due to external factors like temperature and movement of cables. The mean (μ) of the error is calculated along with the standard deviation (σ) and Gaussian distribution curve is overlayed to determine how close the error distribution is to a true Gaussian distribution. In a Gaussian distribution (also referred to as a normal distribution), 68% of the error is within $\mu \pm \sigma$ and 95% of the error is within $\mu \pm 2\sigma$.

In the following sections, the calibration and error are presented along with the monostatic and bistatic measurements.

7.1.2   Monostatic rotated target.

Recall in Chapter 1, a monostatic radar setup has a colocated emitter and receiver. The monostatic set of measurements are taken across a frequency range of 5GHz to 15GHz as the target object is rotated 360°. Since the distance between the emitter and target is static, the amount of time for a scattered field to travel back to the receiver is used to gate out any secondary contributions.

7.1.2.1   Calibration Analysis.

After calibration, the error for TE and TM incidence is determined and can be seen in Figure 7.3. The error in these figures is calculated by calibrating the measured 375 calibration cylinder data and comparing to the exact solution. Error analysis was also performed on the calibrated 450 data and showed similar error statistics.
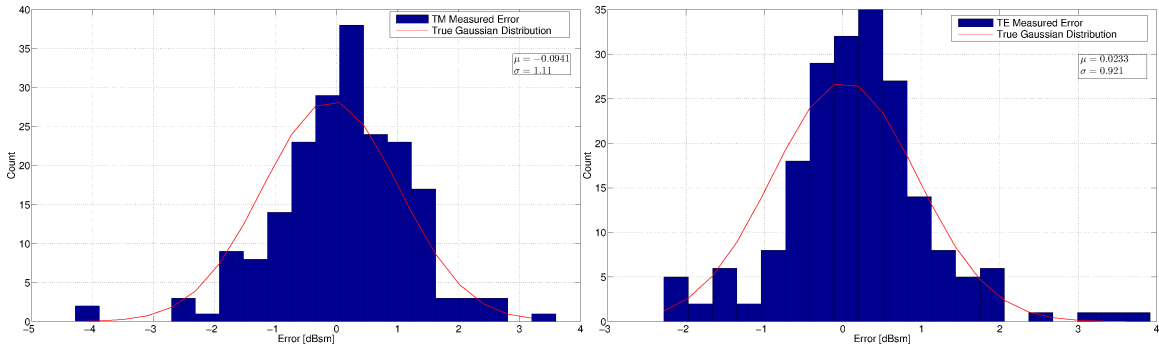
Figure 7.3: Error in the monostatic frequency sweep of the 375 calibration cylinder for TM (left) and TE(right) incidence.

7.1.2.2   Measurements.

The monostatic measurements of the rotated metamaterial cloak show the backscatter for different incident angles.   The cloak is not radially symmetric and therefore,

measurements should change somewhat as a function of incident angle. The flat edge of the fabricated cloak is referenced as 0°, see Figure 6.3. The rotation, $0^o - 360^o$, follows a counter-clockwise motion.

The calibrated measurement data for TM and TE incidence can be seen in Figure 7.4 and shows that adding the cloak to the cylinder does reduce the monostatic RCS for TE incidence. The TM case shows very little difference between the bare and cloaked cylinder. This is expected since the metamaterial constitutive parameters are dependent upon incident polarization and the metamaterials were design for TE incidence.

It is also evident that RCS reduction is realized regardless of the monostatic incident angle. The data in this figure does show some irregularities with the bare cylinder. These irregularities can be attributed to the fact that this is not a perfectly round cylinder. The bare cylinder is still a good comparison since it was manufactured in the same manner as the cylinder within the cloak.

Next, the performance of the metamaterial cloak across the frequency range is examined. Figure 7.5 shows the backscatter of the $0°$ reference angle of the cloak as a function of frequency. As seen in the previous results, the cloak impinged by TM energy does not affect the backscatter much across the frequency range. However, for the TE case, note the RCS of the cloaked cylinder is reduced for nearly every frequency in the range. In particular, the same dip in backscatter near 8-9GHz and 14GHz is seen as was exhibited in the simulated data from Figure 6.14. The calibrated measurement data also shows good agreement with the simulation data of the bare PEC cylinder, further validating the accuracy of the measurements. The wideband operation of the backscatter reduction is expected since the metamaterials are operating within their respective non-resonant region and therefore are not very dispersive.
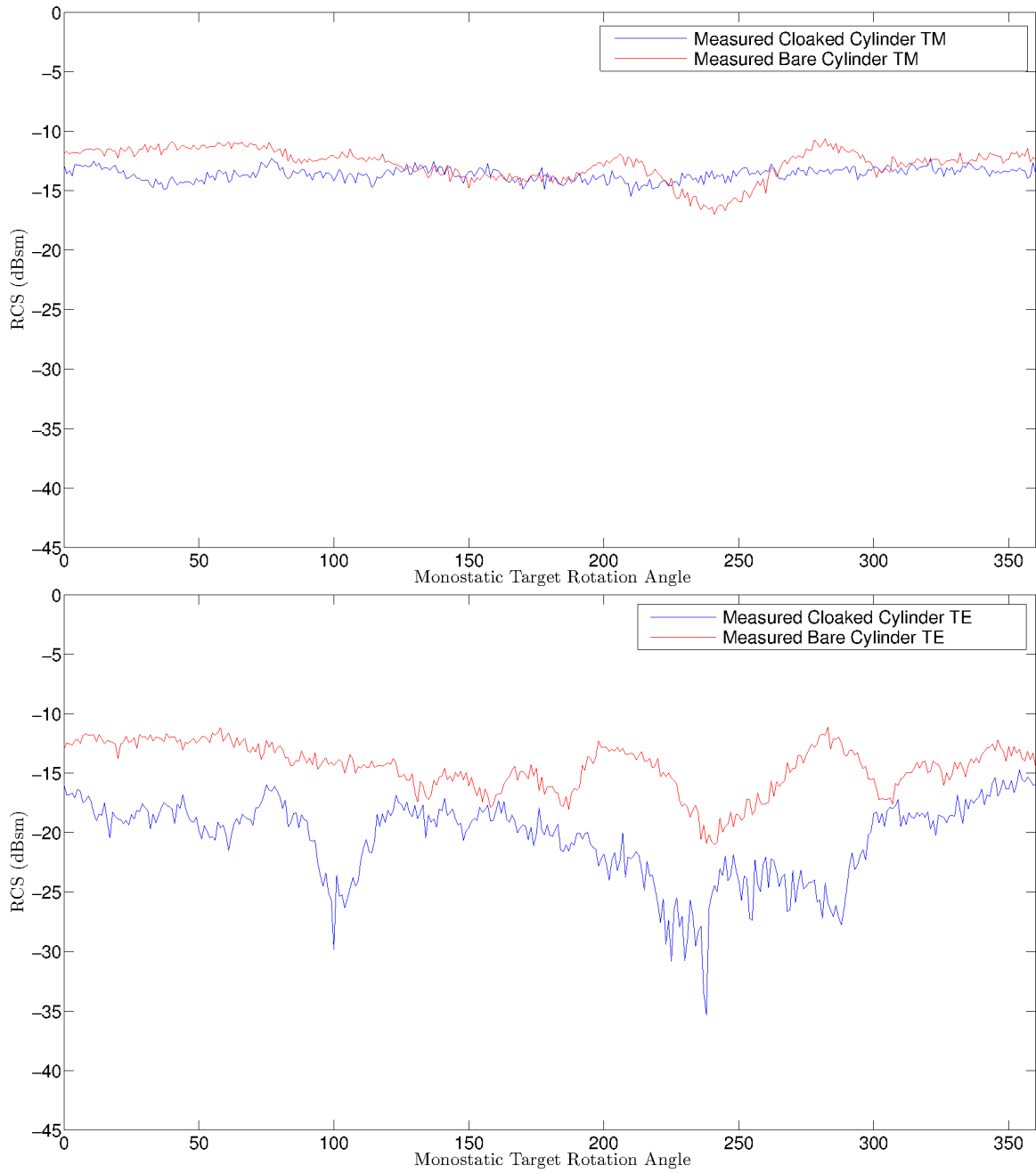
Figure 7.4: Monostatic measurements of the full 360° rotated cloak and bare cylinder for TM incidence(left) and TE incidence(right) at 10GHz.
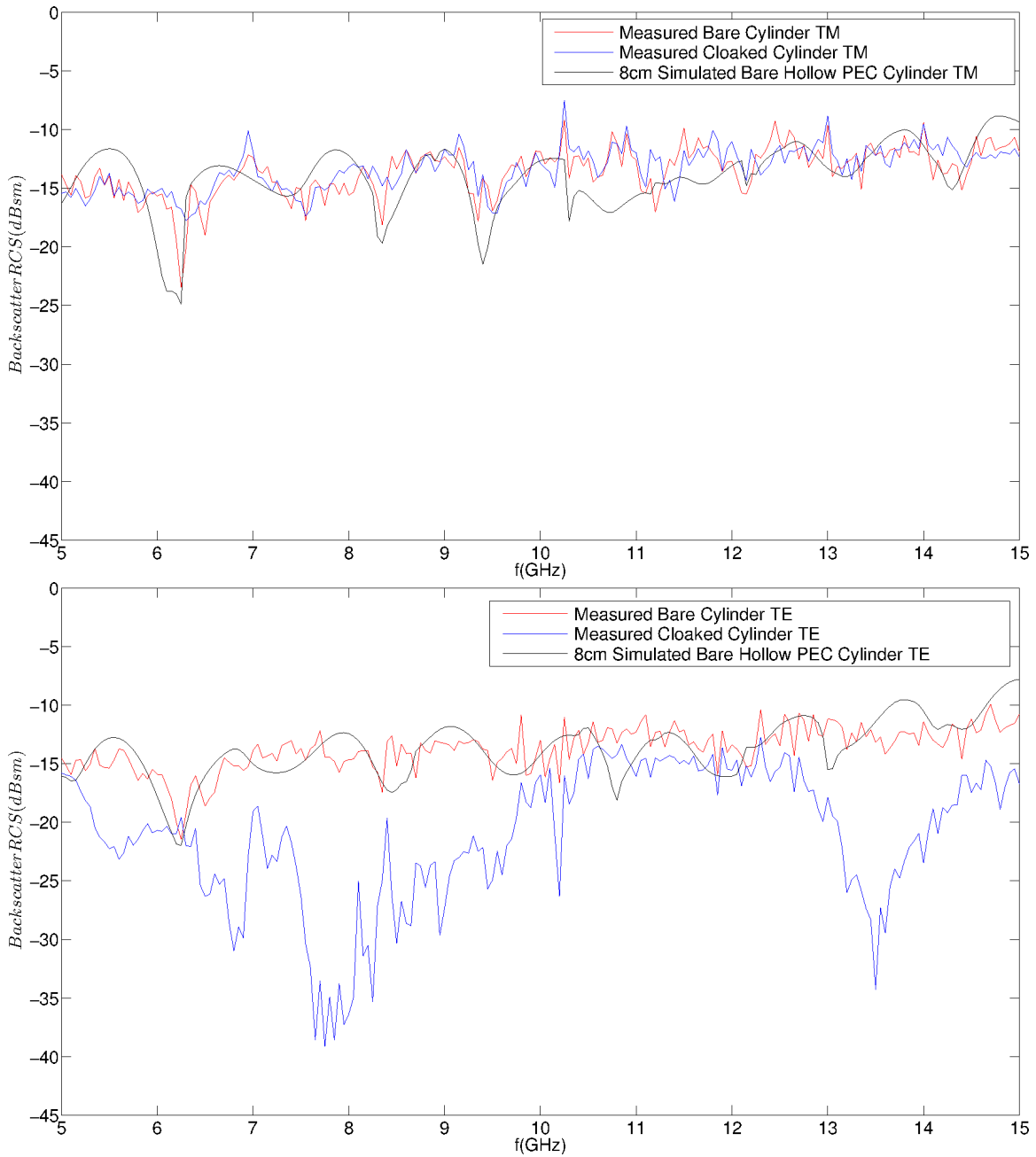
Figure 7.5: Backscatter RCS measurements across the frequency range of the cloak and bare cylinder for TM incidence(top) and TE incidence(bottom). These backscatter measurements are of the flat edge of the cloak.

102

7.1.3   Bistatic.

In this section, the method and results of the bistatic measurements for the cloaked and bare cylinders are presented. The bistatic measurements are taken for every integer angle in the range of $45° - 180°$, where $180°$ corresponds to the backscatter and $0°$ corresponds to forward scatter. One challenge with taking bistatic measurements is time delay gating. At some bistatic angle, the path of the incident energy and the scattered energy to the bistatic receiver will be close if not equal. This means, that accuracy becomes severely degraded because scattered energy cannot be isolated from the incident energy through gating. Our initial bistatic angle range will show us at what point our measurements become suspect. Once this angle is found, the bistatic angle measurements are limited to those angles in which incident energy can be gated out.

7.1.3.1   Calibration Analysis.

As with the monostatic measurements, analysis of the calibration and error is first presented. In this analysis, the bistatic angles in which the incident energy can be gated out are determined. Figure 7.6 shows the calibrated bistatic measurements of the 375 calibration cylinder across a bistatic range of $45° - 180°$.
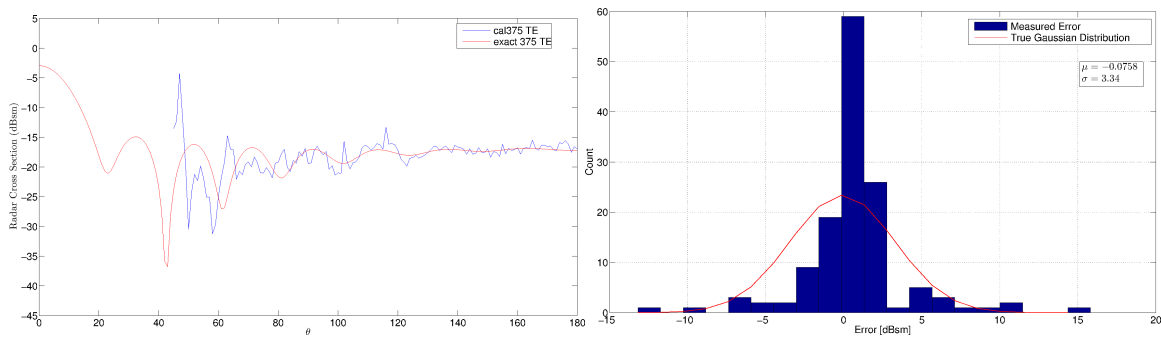
Figure 7.6: Bistatic $45° - 180°$ calibration results. Bistatic 375 calibration cylinder measurements after calibration at 10GHz (left). Error distribution of calibrated 375 calibration target at 10GHz (right).

It is evident the deviation from the exact solution begins to increase around the 85°
bistatic angle. Therefore, the bistatic measurements in this section will be conducted for
the range of 85° − 180°. The calibrated 375 cylinder and error of this new bistatic range can
be seen in Figure 7.7 for TE incidence and Figure 7.8 for TM incidence. This new bistatic
range shows a large reduction in the error distribution from the original range.
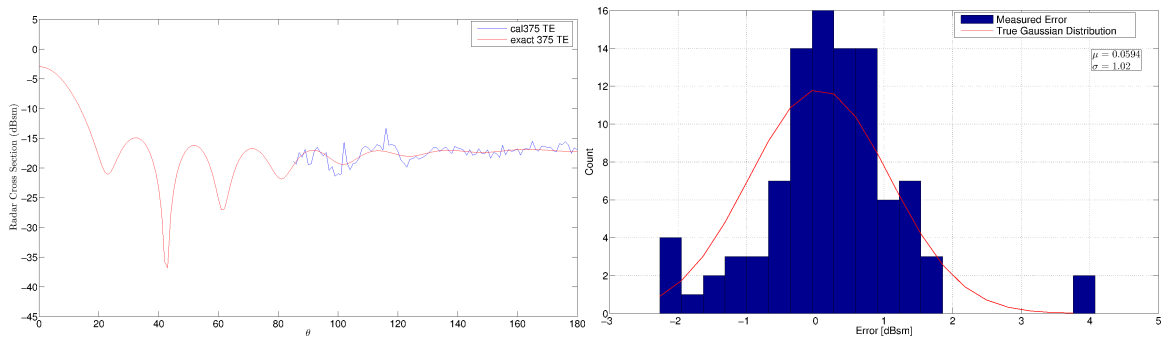
Figure 7.7: Bistatic 85° − 180° calibration results. Bistatic 375 calibration cylinder
measurements after calibration at 10GHz (left). Error distribution of calibrated 375
calibration target at 10GHz (right).
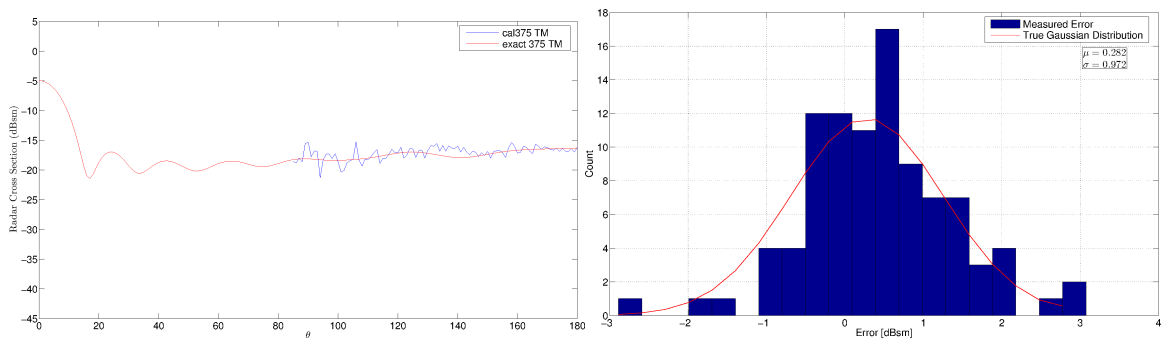
Figure 7.8: Bistatic 85° − 180° calibration results. Bistatic 375 calibration cylinder
measurements after calibration at 10GHz (left). Error distribution of calibrated 375
calibration target at 10GHz (right).

7.1.3.2 Measurements.

Next, the measurements of the metamaterial cloak and bare cylinder are presented for bistatic angles $85° - 180°$. The TM measurements can be seen in Figure 7.9. The exact solution of a bare PEC cylinder of the same height adds further credence these measurements. Even though the fabricated bare cylinder is not exact, it is evident from this data that the calibrated measurements of the bare cylinder are close to the exact solution. Figure 7.10 shows the bistatic measurements across the frequency range for the bare cylinder and cloaked cylinder. This data shows very little difference between the two cases across the frequency range and bistatic angle. Again, this is expected since this cloak is designed for TE incidence.
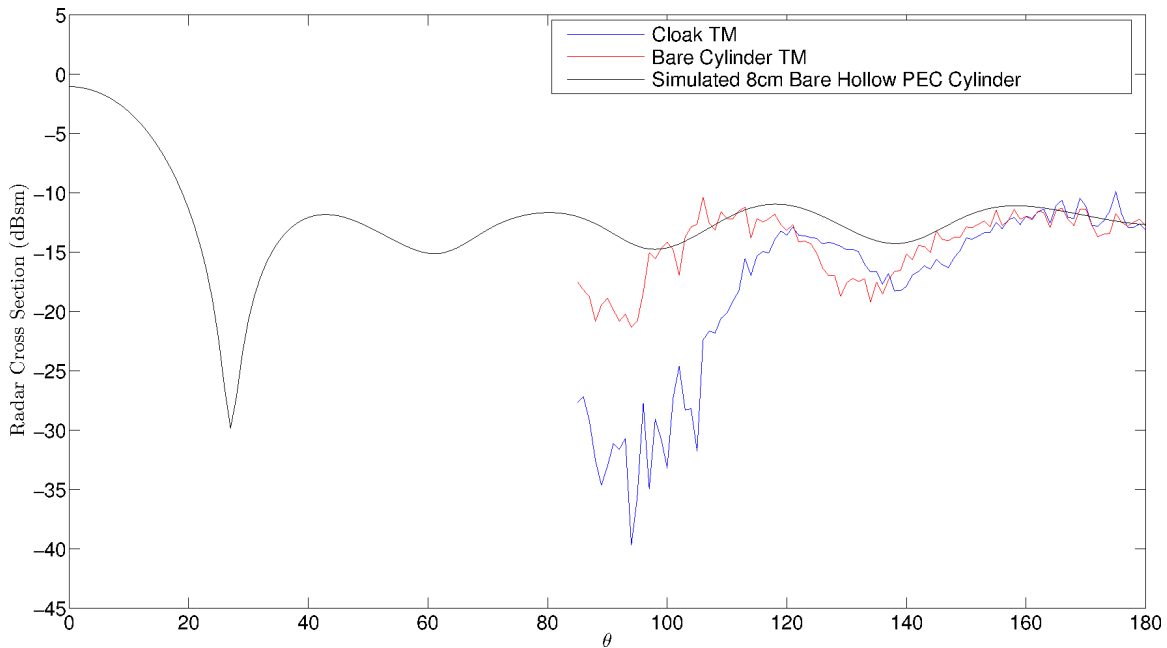
Figure 7.9: Comparison between TM bistatic experimental measurements and simulation results at 10GHz.
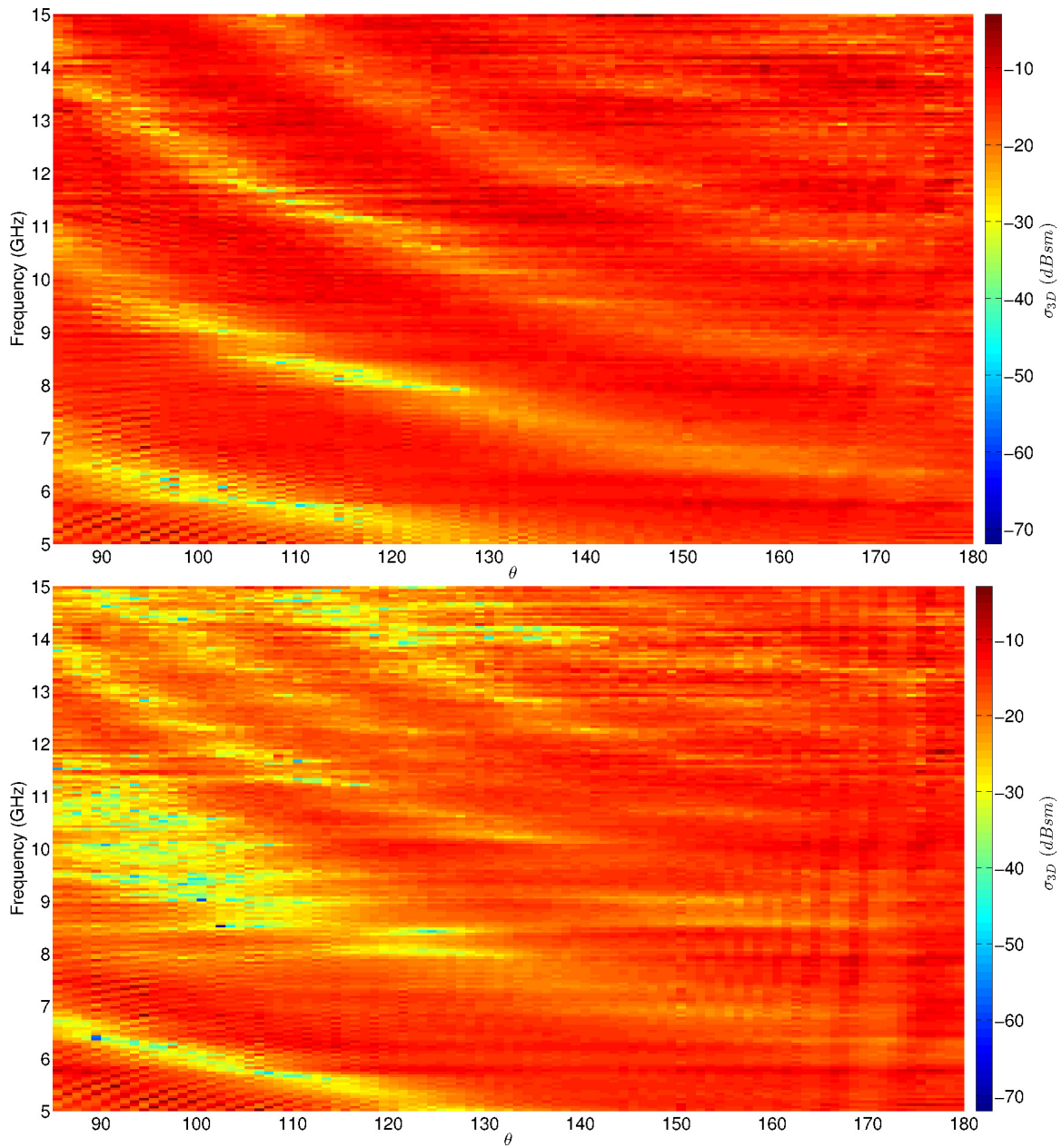
Figure 7.10: Measured TM bistatic RCS across the frequency range 5GHz-15GHz for the bare cylinder(top) and the cloaked cylinder(bottom).

The bistatic measurements for TE incidence can be seen in Figure 7.11. Like the TM case, measurement data of the bare cylinder agrees well with the simulated bare PEC cylinder. Additionally, the RCS approximation of the 2D isotropic cloak with the 'as

fabricated' metamaterial constitutive parameters from the previous chapter in Table 6.4 is plotted. The approximation is of the form

$$\sigma_{3D} = \sigma_{2D} \frac{2\ell^2}{\lambda} \tag{7.2}$$

where ℓ is the height of the fabricated cylinder [2]. This approximated RCS data tracks fairly well with the measured data and further validates the isotropic Green's function approach for designing a metamaterial cloaked cylinder.
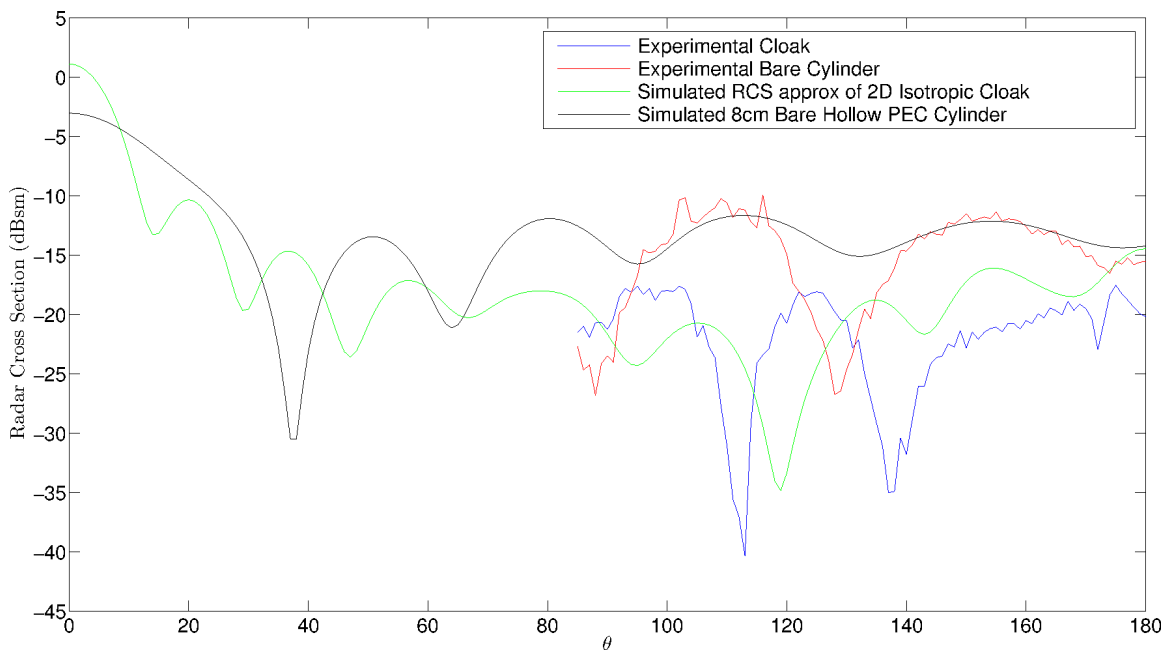
Figure 7.11: Comparison between TE bistatic experimental measurements and simulation results at 10GHz.

Figure 7.12 shows the measured bistatic RCS for the bare and cloaked cylinders across the frequency range 5GHz-15GHz. This data also shows the same behavior as the simulated data in Figure 6.14 as seen in the range 8-9GHz. Note that only the bistatic angles $85° - 180°$ were measured, so only part of the simulated data can be used for comparison.
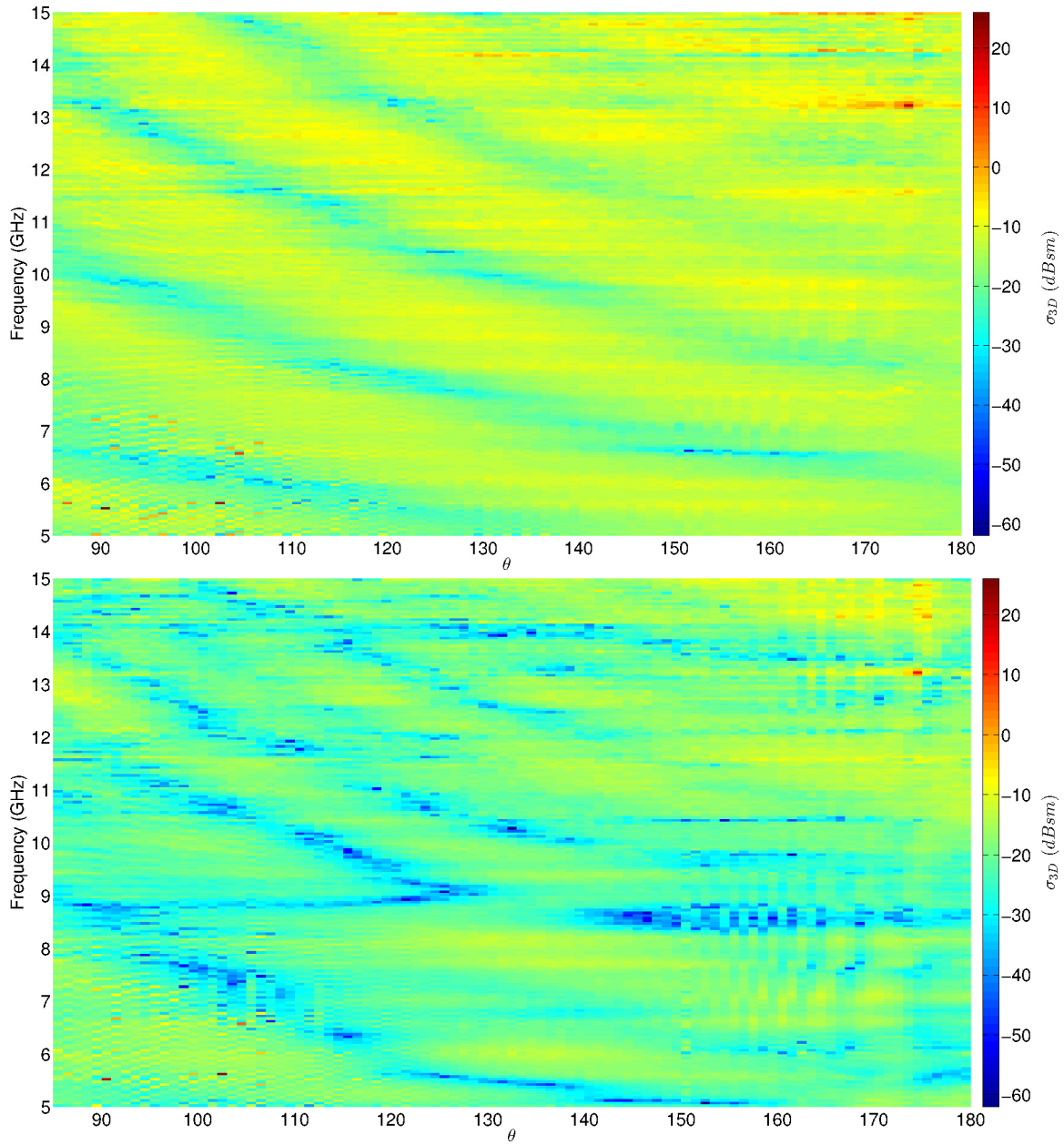
Figure 7.12: Measured TE bistatic RCS across the frequency range 5GHz-15GHz for the bare cylinder(top) and the cloaked cylinder(bottom).

7.2 Summary

In this chapter, the experimental RCS measurements of the cloaked and bare cylinders were presented. The error of both monostatic and bistatic measurements were explained

and detailed. The data presented in these measurements validates the effectiveness of using the 2D isotropic Green's function optimization approach to creating a 3D metamaterial cloaked cylinder.

VIII.   Summary of Contributions and Further Research

8.1   Research Summary

Previously, TO has been used as a foundation for designing cylindrical cloaks. The TO cloak uses the material parameter gradient to guide waves around a cylinder to reduce the RCS. The problem is that the material parameters required for the TO cloak are not physically realizable and thus must be approximated. This problem is compounded by the fact that any approximation that deviates from the ideal design will allow fields to penetrate the cloak layer and interact with the object to be cloaked. Since the TO method does not account for this interaction, approximating the ideal TO parameters is doomed to less than optimal results. The goal of this dissertation is to create a design process for an optimized cloaked cylinder which accounts for all of the physical interactions within the cloak. This effort resulted in 3 main research thrusts that culminate in a beginning to end design process for an optimized cloaked cylinder that is then fabricated with metamaterials.

The first main area of research extracted the contribution due to the scatterer in a Green's function for an n-layered cylinder. A general algebraic expression was then derived by exploiting the recursive boundary conditions. This general expression can then be used as a cost functional implemented by an optimization algorithm to minimize the contribution due to the scatterer. If the contribution due to the scatterer is 0, then the observer, regardless of position outside of the cloak, will only observe the contribution due to the source. This is the definition of a cloak. The contribution in this area of research is threefold. First, this general expression cost functional allows for the design of optimized cloaks for a large number of layers without the need of deriving new expressions. Second, the general expression cost functional is more efficient than those in literature because it is inherently angle independent since it originates from a Green's function. Third, the general expression can be used to determine the azimuthal surface wave propagation constants for an n-layered

cylinder. This last contribution resulted in [25], currently slated to be published in May 2013.

The second main area of research implemented this cost functional to study optimized isotropic cloaks of many layers. The largest optimized isotropic cloak in the literature to date consisted of 6 layers whereas the 10, 20 and 30 layer cases were studied. This study contributed 3 main points. First, by using an unconstrained optimization algorithm, it was shown that an optimized 10 layer isotropic cloak could perform better than the simulated TO ideal anisotropic cloak for nearly every angle for TM incidence but not for TE incidence. Second, it was shown that optimizing individual layer thicknesses as well as material parameters of a 10 layer cloak rendered better results than the 10, 20 and 30 layer optimized cloaks with fixed layer thicknesses for TM and TE incidence. Third, it was noted that the material parameters of the optimized isotropic cloaks did not show the dual nature between TM and TE incidence that is evident in the material parameters of the ideal TO case. This indicates that any deviation from the ideal TO parameters, and thus any physical cloak, needs to account for the difference in TM and TE interaction with the surface within the cloak. The Green's function approach accounts for this interaction. The efforts in this section are currently in the submission process to *Journal of Physics D: Applied Physics*.

The last research area combines the previous areas to create a design process for implementing an optimized isotropic cloak with metamaterials. The previously developed cost functional was used to optimize a cloak over a set of manufacturable material parameters provided by a metamaterial design process. The focus in this section was to optimize a cloak for a given geometry that is easy to fabricate and construct. The cloaks in literature are more difficult to construct and made of only one type of metamaterial unit cell whereas our design is simple to construct and made of 3 different types of metamaterial unit cells. This resulted in a metamaterial cloak which reduces the monostatic and the bistatic RCS of a bare conducting cylinder for most measured angles. In addition, a reduction in

111

monostatic RCS evident for nearly all frequencies swept (5GHz-15GHz). To date, neither bistatic nor monostatic RCS measurements of a metamaterial cloak have been presented in literature. Most importantly, this last section validates the use of an isotropic Green's function approach to designing a metamaterial cloaked cylinder. The contribution of this last section is in a draft form, tentatively targeted for *Journal of Physics D: Applied Physics*.

8.2   Recommendations for Future Research

8.2.1   *Excited Azimuthal Waves of a Cloaked Cylinder.*

In Chapter 5, the disparity between the cloaking performance of the optimized TE cloak and TM cloak was noted. Furthermore, the optimized parameters between the TE and TM cases were not duals of each other as is the case with the TO case. It was concluded that since the TO cloak does not allow fields to penetrate the cloak, the dual nature of the material parameters makes sense due to identical boundary conditions for both incident polarizations. However, in a non-ideal cloak, fields will penetrate the cloak layer and impinge upon the surface of the cloaked object which will enforce a boundary condition which is dependent on incident polarization.

Since non-ideal cloaks allow impingement of the PEC cylinder, azimuthally traveling surface waves will be excited along the cylinder. The propagation of these waves are dependent on incident polarization and the materials surrounding the cylinder. Furthermore, these excited surface waves will affect the RCS of a coated cylinder. Therefore, it is a logical next step to study how these surface waves will impact cloaking performance. The general cost functional, derived in Chapter 4, can be used to determine the azimuthal surface wave propagation constants to this end. It is quite possible that the result of this type of study could be used to augment the optimization process in this dissertation to render a more effective cloak.

8.2.2   Optimization with Loss Using Kramers-Kronig Relation.

In Chapter 5, different optimized cloaks were presented. These cloaks assumed lossless materials. It stands to reason, that this study should also be accomplished for the lossy case since any material implemented to created a physical cloak will contain some loss. The challenge is that an unconstrained optimization algorithm cannot be used because the solution could be lossy material parameters which are not causal. Therefore, constraints that implement the Kramers-Kronig relation could be used to optimize a cloak made with lossy material parameters that are causal.

8.2.3   Maximize Scatterer Contribution.

The ultimate goal in this dissertation was to create a cloaked cylinder. A cost functional was used with an optimization algorithm to find the material parameters for an optimal cloak. There are also applications for maximizing this cost functional to create a larger RCS of a coated cylinder. This could be used in the cases of designing chaff or in other instances of countermeasures where a larger RCS is beneficial.

8.2.4   Cloak design with Isotropic materials (non metamaterials).

The design process presented in this dissertation implemented metamaterials in an effort to study the inherent assumptions of using this type of material. The design process itself is not limited to metamaterials and could be used to optimize or any set of physically realizable material parameters. Furthermore, metamaterial unit cells are somewhat static which limited the manipulation of the layer thicknesses in this research effort. If materials in which layer thicknesses could be controlled are used, the thicknesses of these layers could also be a free variable which will render a more effective cloak as seen in Chapter 5. Also, a cloak using isotropic materials would create a much more robust cloaked cylinder in which the incident energy is not limited to just normal incidence.

Appendix A: Optimized Parameters for Cloaked Cylinders

In Chapter 5 10, 20 and 30 layer cloaks were optimized for TE and TM incidence. Tables A.1, A.2 and A.3 show the resulting material parameters for these optimized cloak cylinders.

Layer		1	2	3	4	5	6	7	8	9	10
TM	ϵ_r	0.01	1.15	1.02	1.06	1.60	2.51	2.56	1.10	2.10	0.72
	μ_r	5.81	0.06	7.22	0.20	4.03	0.12	3.37	0.22	3.60	0.57
TE	ϵ_r	12.76	0.10	6.35	0.12	4.43	0.19	4.20	0.33	3.30	0.54
	μ_r	0.09	0.47	0.90	1.70	1.72	1.72	1.53	1.35	1.42	1.15

Table A.1: Optimized material parameters for 10 equal thickness layer TE and TM cloaked cylinders.

Layer		1	2	3	4	5	6	7	8	9	10
TM	ϵ_r	0.21	0.32	0.54	0.64	0.84	0.63	1.03	1.34	1.26	1.19
	μ_r	29.18	0.03	12.76	0.08	10.32	0.08	6.21	0.14	5.86	0.18
TE	ϵ_r	20.90	0.04	14.40	0.09	8.51	0.12	6.50	0.15	5.17	0.17
	μ_r	0.19	0.32	0.52	0.55	0.81	0.83	1.31	1.15	1.24	1.23

Layer		11	12	13	14	15	16	17	18	19	20
TM	ϵ_r	1.23	1.46	1.58	1.65	1.79	1.95	1.75	1.85	1.89	1.93
	μ_r	6.13	0.18	4.52	0.21	5.87	0.23	6.48	0.23	4.20	0.36
TE	ϵ_r	4.72	0.20	4.16	0.22	4.85	0.24	3.58	0.26	4.09	0.35
	μ_r	1.29	1.59	1.68	1.55	1.69	1.70	1.90	2.02	1.52	2.06

Table A.2: Optimized material parameters for 20 equal thickness layer TE and TM cloaked cylinders.

Layer		1	2	3	4	5	6	7	8	9	10	11	12	13	14	15
TM	ϵ_r	0.20	0.21	0.37	0.51	0.56	0.68	0.78	0.73	0.75	0.88	1.15	1.20	1.24	1.16	1.28
	μ_r	40.67	0.03	17.15	0.04	12.38	0.04	12.47	0.07	8.63	0.13	4.94	0.14	6.82	0.14	6.13
TE	ϵ_r	29.45	0.03	17.33	0.05	12	0.07	9.70	0.10	7.65	0.13	7.03	0.14	6.21	0.16	6.05
	μ_r	0.13	0.26	0.36	0.48	0.54	0.64	0.67	0.84	0.91	1.03	1.13	1.15	1.23	1.28	1.25

Layer		16	17	18	19	20	21	22	23	24	25	26	27	28	29	30
TM	ϵ_r	1.39	1.48	1.31	1.70	1.73	1.61	1.69	1.75	1.90	1.86	1.91	1.94	2.02	1.91	1.95
	μ_r	0.16	6.33	0.18	4.60	0.20	5.81	0.22	4.43	0.20	3.58	0.23	4.00	0.25	4.44	0.34
TE	ϵ_r	0.19	5.16	0.19	4.43	0.21	4.58	0.21	4.49	0.24	3.82	0.24	3.85	0.26	4.2	0.33
	μ_r	1.34	1.45	1.57	1.56	1.60	1.58	1.62	1.72	1.80	1.92	1.92	1.75	1.92	1.94	2.02

Table A.3: Optimized material parameters for 30 equal thickness layer TE and TM cloaked cylinders.

Appendix B: Green's Function Derivation

This Green's function was originally derived in McGuirk's dissertation [17] and is presented here verbatim with added comments to clarify as needed. In [17], the bare PEC and single layer cases were derived first to serve as self validation of the n-layer case. In this appendix, we only present the derivation for the n-layer case.

B.1 Problem Setup

For the case of the TE_z cloaked cylinder comprised of n layers, we use an infinite (in $\hat{z}$) line source to illuminate the cloaked cylinder. We will only express the incident and scattered fields in terms of the $\hat{z}$ directed magnetic field, or more precisely, the $\hat{z}$ directed vector potential $\vec{F}_z$. The vector potential wave equation is given as

$$\nabla^2 F_z + k^2 F_z = -\epsilon \mathcal{M}$$

where $\mathcal{M}$ is the magnetic current of the line source. Invariance in the $\hat{z}$ direction is assumed which allows us to simplify the potential wave equation as Equation B.1

$$\nabla_t^2 F_z + k^2 F_z = -\epsilon \mathcal{M} \tag{B.1}$$

where ∇_t^2 is the transverse Laplacian which can be expressed in cylindrical coordinates as Equation B.2.

$$\nabla_t^2 = \frac{1}{\rho}\frac{\partial}{\partial \rho}\left(\rho\frac{\partial}{\partial \rho}\right) + \frac{1}{\rho^2}\frac{\partial^2}{\partial \theta^2} \tag{B.2}$$

We can express the potential wave equation as Equation B.3 for an n-layered geometry.

$$\left(\nabla_t^2 + k\right) F_z = -\epsilon \mathcal{M}_z \qquad k = \begin{cases} k_1 = \omega \sqrt{\mu_r \epsilon_r \mu_0 \epsilon_0} & a < \rho < \rho_i \\ k_i = \omega \sqrt{\mu_{r_i} \epsilon_{r_i} \mu_0 \epsilon_0} & \rho_i < \rho < \rho_{i+1} \\ k_0 = \omega \sqrt{\mu_0 \epsilon_0} & \rho > \rho_n \end{cases} \tag{B.3}$$

B.1.1   Boundary Conditions.

Next, the boundary conditions are enumerated. The boundary conditions for the PEC interface, angular continuity and far field can be seen in Equation B.4.

$$-\frac{1}{\epsilon}\frac{\partial}{\partial \rho} F_z\left(\rho, \theta; \rho', \theta'\right)\bigg|_{\rho=a} = 0$$

$$F_z\left(\rho, \theta; \rho', \theta'\right) = F_z\left(\rho, \theta + 2\pi; \rho', \theta'\right)$$

$$\frac{\partial}{\partial \rho} F_z\left(\rho, \theta; \rho', \theta'\right)\bigg|_{\rho=\infty} = -jk\frac{\partial}{\partial \rho} F_z\left(\rho, \theta; \rho', \theta'\right)\bigg|_{\rho=\infty} \tag{B.4}$$

We also must enforce continuity of the tangential fields at every layer interface as

$$F_z\bigg|_{\rho=\rho_i^-} = F_z\bigg|_{\rho=\rho_i^+}$$

$$\frac{1}{\epsilon^-}\frac{\partial}{\partial \rho} F_z\bigg|_{\rho=\rho_i^-} = \frac{1}{\epsilon^+}\frac{\partial}{\partial \rho} F_z\bigg|_{\rho=\rho_i^+} \tag{B.5}$$

where $i = 1, 2 \ldots n$.

B.2   Green's Function

The Green's function we wish to derive will solve is

$$\left(\nabla_t^2 + k_0\right) G\left(\rho, \rho'\right) = -\frac{\delta\left(\rho - \rho'\right)\delta\left(\theta - \theta'\right)}{\rho}. \tag{B.6}$$

From [7], the solution of Equation B.6 is of the form seen in Equation B.7

$$G\left(\rho, \theta; \rho', \theta'\right) = \sum_{\nu=0}^{\infty} \tilde{u}_\nu\left(\theta\right) \tilde{u}_\nu^*\left(\theta'\right) G_\rho\left(\rho, \rho'; \lambda_\nu\right) \tag{B.7}$$

where $\tilde{u}_\nu$ are the orthonormal eigenfunctions that satisfy

$$\left[\frac{d^2}{d\theta^2} + \lambda_\nu\right]\tilde{u}_\nu = 0 \tag{B.8}$$

and

$$\tilde{u}_\nu\left(\theta\right) = \tilde{u}_\nu\left(\theta + 2\pi\right). \tag{B.9}$$

Also note that G_ρ satisfies Equation B.10.

$$\frac{1}{\rho}\frac{d}{d\rho}\left(\rho\frac{dG_\rho}{d\rho}\right) + \left(k^2 - \frac{\lambda_\nu}{\rho^2}\right)G_\rho = -\frac{\delta\left(\rho - \rho'\right)}{\rho} \tag{B.10}$$

B.2.1 Solving for the orthonormal eigenfunctions $\tilde{u}_\nu$.

A general solution for $\tilde{u}_\nu$ is

$$\tilde{u}_\nu = A\cos\left(\sqrt{\lambda_\nu}\theta\right) + B\sin\left(\sqrt{\lambda_\nu}\theta\right)$$

and applying Equation B.9 we arrive at

$$A\cos\left(\sqrt{\lambda_\nu}\theta\right) + B\sin\left(\sqrt{\lambda_\nu}\theta\right) = A\cos\left(\sqrt{\lambda_\nu}\left(\theta + 2\pi\right)\right) + B\sin\left(\sqrt{\lambda_\nu}\left(\theta + 2\pi\right)\right). \tag{B.11}$$

Equation B.11 can be solved if $\sqrt{\lambda_\nu} = \nu$ where $\nu = 0, 1, 2\ldots$ and therefore

$$\sqrt{\lambda_\nu} = \nu, \qquad \nu = 0, 1, 2\ldots,$$

$$\lambda_\nu = \nu^2, \qquad \nu = 0, 1, 2\ldots$$

which allows us to write the general solution as

$$\tilde{u}_\nu = A\cos\left(\nu\theta\right) + B\sin\left(\nu\theta\right).$$

Since $A\cos\left(\nu\theta\right)$ is orthogonal to $B\sin\left(\nu\theta\right)$, then both of these terms are part of the solution of eigenvectors.

119

It is possible to calculate A and B by using the fact that

$$\int_0^{2\pi} A^2 \cos^2(v\theta)\,d\theta = 1 \tag{B.12}$$

$$\int_0^{2\pi} B^2 \sin^2(v\theta)\,d\theta = 1 \tag{B.13}$$

in combination with the trigonometric identities

$$\cos^2(v\theta) = \frac{1}{2} + \frac{1}{2}\cos(2v\theta) \tag{B.14}$$

$$\sin^2(v\theta) = \frac{1}{2} + \frac{1}{2}\sin(2v\theta) \tag{B.15}$$

results in

$$\int_0^{2\pi} A^2 \cos^2(v\theta)\,d\theta = \frac{A^2}{2}\left[\int_0^{2\pi} d\theta + \int_0^{2\pi} \cos(2v\theta)\,d\theta\right] = 1. \tag{B.16}$$

Equation B.16can then be simplified to

$$A = \sqrt{\frac{1}{\pi}}. \tag{B.17}$$

However, this is only valid if $v \neq 0$. This is not the case for the variable B, since $v = 0$ results in a trivial solution. In light of this, A and B are expressed as

$$A, B = \sqrt{\frac{\epsilon_v}{2\pi}} \tag{B.18}$$

where ϵ_v is the Neumann number as seen in Equation B.19.

$$\epsilon_v = \begin{cases} 1 & v = 0 \\ 2 & v = 1, 2, 3 \dots \end{cases} \tag{B.19}$$

120

Note that Equation B.18 states that when $v = 0$, then $B = \sqrt{\frac{1}{2\pi}}$. This isn't necessarily true, but is irrelevant since the $\sin^2(v\theta)$ make the product zero regardless of the value of B. This results in the expression of the orthonormal eigenfunctions seen in Equation B.20.

$$\sum_{v=0}^{\infty} \tilde{u}_v(\theta)\, \tilde{u}_v^*(\theta') = \frac{1}{2\pi} \sum_{v=0}^{\infty} \epsilon_v \left[\cos(v\theta)\cos(v\theta') + \sin(v\theta)\sin(v\theta') \right] \tag{B.20}$$

After using the trigonometric identity

$$\cos x \cos y + \sin x \sin y = \cos(x - y) \tag{B.21}$$

we get

$$\sum_{v=0}^{\infty} \tilde{u}_v(\theta)\, \tilde{u}_v^*(\theta') = \frac{1}{2\pi} \sum_{v=0}^{\infty} \epsilon_v \cos\left[v(\theta - \theta') \right]. \tag{B.22}$$

B.2.2 Solving for G_ρ.

The next step is to solve for G_ρ. Recall G_ρ solves the equation

$$\frac{1}{\rho} \frac{d}{d\rho}\left(\rho \frac{d}{d\rho} G_\rho \right) + \left(k^2 - \frac{\lambda_v}{\rho^2} \right) G_\rho = -\frac{\delta(\rho - \rho')}{\rho}$$

which after multiplying by ρ results in

$$\frac{d}{d\rho}\left(\rho \frac{d}{d\rho} G_\rho \right) + \left(k^2 \rho - \frac{\lambda_v}{\rho} \right) G_\rho = -\delta(\rho - \rho'). \tag{B.23}$$

We can solve this equation using the U-T method, where $U(\rho), T(\rho)$ satisfies the boundary conditions at $\rho = a, b, \rho_i$ and $\rho \to \infty$ respectively as seen below.

$$\frac{d}{d\rho}\left(\rho \frac{d}{d\rho} \right) + \left(k^2 \rho - \frac{\lambda_v}{\rho} \right) \Bigg|_{T(\rho)}^{U(\rho)} = 0$$

The Green's function will have the form

$$G_\rho = \frac{U(\rho_<) T(\rho_>)}{c}$$

121

where c is the conjunct as given below

$$c = \rho\left[TU' - T'U\right] \tag{B.24}$$

The variables $U(\rho), T(\rho)$ have the form:

$$U(\rho) = \begin{cases} A_\nu^1 J_\nu(k_1\rho) - B_\nu^1 H_\nu^{(2)}(k_1\rho) & a < \rho < \rho_1 \\ A J_\nu^i(k_i\rho) + B_\nu^i H_\nu^{(2)}(k_i\rho) & \rho_{i-1} < \rho < \rho_i \end{cases}$$

Since there are multiple regions, we must solve for each region, using the applicable boundary conditions. Note the first equation must satisfy the boundary condition at the PEC interface, $\rho = a$. This results in

$$B_\nu^1 = -A_\nu^1 \frac{J_\nu'(k_1a)}{H_\nu^{(2)}(k_1a)}. \tag{B.25}$$

A similar process is used for the T expressions, which for the various regions are

$$T(\rho) = \begin{cases} C_\nu^1 J_\nu(k_1\rho) + D_\nu^1 H_\nu^{(2)}(k_1\rho) & a < \rho < \rho_1 \\ C_\nu^i J_\nu(k_i\rho) + D_\nu^i H_\nu^{(2)}(k_i\rho) & \rho > b \end{cases}.$$

In the case of the T expressions, $C_\nu^{n+1} = 0$ and $D_\nu^{n+1} = 1$ which is due to the radiation condition (ie there will be no standing waves). The conjunct is then found to be

$$c = \frac{j2A_\nu^{n+1}}{\pi}. \tag{B.26}$$

This results in a final Green's function where both observer and source are outside of the structure and can be seen in Equation B.27.

$$G\left(\rho, \theta; \rho', \theta'\right) = -j\frac{\pi}{2A_\nu^{n+1}} \cos\left[\nu\left(\theta - \theta'\right)\right]\left[A_\nu^{n+1} J_\nu(k_0\rho_<) + B_\nu^{n+1} H_\nu^{(2)}(k_0\rho_<)\right] H_\nu^{(2)}(k_0\rho_>)$$

$$\tag{B.27}$$

Additionally, due to the PEC boundary condition and the radiation boundary condition,

$$A_\nu^{n+1} = 1 \tag{B.28}$$

$$B_\nu^1 = -A_\nu^1 \frac{J_\nu'(k_1 a)}{H_\nu^{(2)}(k_1 a)} \tag{B.29}$$

and the continuity boundary conditions at each layer interface as seen in Equation B.5.

$$A_\nu^1\left(J_\nu(k_1\rho_1) - K_\nu H_\nu^{(2)}(k_1\rho_1)\right) = A_\nu^2 J_\nu(k_2\rho_1) + B_\nu^2 H_\nu^{(2)}(k_2\rho_1)$$

$$A_\nu^1 \frac{\epsilon_{r2}}{k_1}\left(J_\nu'(k_1\rho_1) - K_\nu H_\nu^{'(2)}(k_1\rho_1)\right) = \frac{\epsilon_{r1}}{k_2}\left(A_\nu^2 J_\nu'(k_2\rho_1) + B_\nu^2 H_\nu^{'(2)}(k_2\rho_1)\right)$$

$$A_\nu^2 J_\nu(k_2\rho_2) + B_\nu^2 H_\nu^{(2)}(k_2\rho_2) = A_\nu^3 J_\nu(k_3\rho_2) + B_\nu^3 H_\nu^{(2)}(k_3\rho_2)$$

$$\frac{\epsilon_{r3}}{k_2}\left(A_\nu^2 J_\nu'(k_2\rho_2) + B_\nu^2 H_\nu^{'(2)}(k_2\rho_2)\right) = \frac{\epsilon_{r2}}{k_3}\left(A_\nu^3 J_\nu'(k_3\rho_2) + B_\nu^3 H_\nu^{'(2)}(k_3\rho_2)\right)$$

$$\vdots$$

$$A_\nu^n J_\nu(k_n\rho_n) + B_\nu^n H_\nu^{(2)}(k_n\rho_n) = J_\nu(k_0\rho_n) + B_\nu^{n+1} H_\nu^{(2)}(k_0\rho_n)$$

$$\frac{1}{k_n}\left(A_\nu^n J_\nu'(k_n\rho_n) + B_\nu^n H_\nu^{'(2)}(k_n\rho_n)\right) = \frac{\epsilon_{rn}}{k_0}\left(J_\nu'(k_0\rho_n) + B_\nu^{n+1} H_\nu^{'(2)}(k_0\rho_n)\right) \tag{B.30}$$

Through Equations B.28, B.29 and B.30, we can solve for the coefficients A^i, B^i and ultimately B^{n+1}. This creates a system of equations that can be solved as a matrix [17] or algabraically as seen in Chapter 4.

Appendix C: Transformation Optics Cylindrical Cloak

This appendix details how the TO approach is used to derive the material parameters requirements for the cylindrical cloak. Essentially, this method uses the fact that Maxwell's equations are invariant to coordinate transforms in free space but not within a material [30]. Due to this, fields can be controlled by manipulating the coordinate system. This warping of the coordinate system is manifested through material parameter requirements.

While Ward and Pendry [48]did not use this specific method of deriving the equations for the material parameters, the results are identical. References [30, 42] were used for this derivation along with the examples found in [33, 38].

C.1 Background

We begin the process with Maxwell's equations expressed in Minkowski 4-dimension space time tensor format. These can be dervied from the curl and divergence equations as seen below

$$\nabla \times H - \frac{\partial D}{\partial t} = J \qquad \nabla \cdot D = q \tag{C.1}$$

$$
\begin{aligned}
0 + \frac{\partial H_z}{\partial y} - \frac{\partial H_y}{\partial z} - jc\frac{\partial D_x}{\partial t} &= J_x \\
-\frac{\partial H_z}{\partial x} + 0 + \frac{\partial H_x}{\partial z} - jc\frac{\partial D_y}{\partial t} &= J_y \\
\frac{\partial H_y}{\partial x} - \frac{\partial H_x}{\partial y} + 0 - jc\frac{\partial D_z}{\partial t} &= J_z \\
jc\frac{\partial D_x}{\partial x} + jc\frac{\partial D_y}{\partial y} + jc\frac{\partial D_z}{\partial z} + 0 &= jcq
\end{aligned}
\tag{C.2}
$$

where c is the speed of light in free space and q is electric charge density [42]. This formulation then leads to the tensor G as seen in Equation C.3.

$$G = \begin{bmatrix} 0 & H_z & -H_y & -jcD_x \\ -H_z & 0 & H_x & -jcD_y \\ H_y & -H_x & 0 & -jcD_z \\ jcD_x & jcD_y & jcD_z & 0 \end{bmatrix}$$ (C.3)

Likewise, the curl and divergence expressions in Equation C.4 can be expressed as the tensor F in Equation C.5.

$$\nabla \times E - \frac{\partial B}{\partial t} = 0 \qquad \nabla \cdot B = 0$$ (C.4)

$$F = \begin{bmatrix} 0 & B_z & -B_y & -\frac{j}{c}E_x \\ -B_z & 0 & B_x & -\frac{j}{c}E_y \\ B_y & -B_x & 0 & -\frac{j}{c}E_z \\ -\frac{j}{c}E_x & -\frac{j}{c}E_y & -\frac{j}{c}E_z & 0 \end{bmatrix}$$ (C.5)

As seen in [30], the G and F tensors are related to the constitutive parameter tensor χ by Equation C.6.

$$G = \frac{1}{2}\chi F$$ (C.6)

Assuming time invariance, we can change the coordinate system of the tensors in Equation C.6 by using the Jacobian transform

$$J = \begin{bmatrix} \frac{\partial x}{\partial q_1} & \frac{\partial x}{\partial q_2} & \frac{\partial x}{\partial q_3} \\ \frac{\partial y}{\partial q_1} & \frac{\partial y}{\partial q_2} & \frac{\partial y}{\partial q_3} \\ \frac{\partial z}{\partial q_1} & \frac{\partial z}{\partial q_2} & \frac{\partial z}{\partial q_3} \end{bmatrix}$$ (C.7)

where (q_1, q_2, q_3) are the coordinates in a general coordinate system. Specifically, the consititutive parameter tensor can be transformed with the Jacobian as seen in Equation C.8 [30]

125

$$
\begin{bmatrix} \epsilon' \\ \mu' \end{bmatrix} = \left| J^{-1} \right| J J^T \begin{bmatrix} \epsilon \\ \mu \end{bmatrix} \tag{C.8}
$$

where $'$ denotes the parameter in the new coordinate system. Now that we have the foundation for the TO method, the next section derives the material parameters for the cylindrical cloak from [36].

C.2 Deriving Parameters for Cylindrical Cloak

As seen in the G and F tensors above, the cartesian coordinate system is used, but our final coordinate system will be a warped cylindrical coordinate system and therefore a Jacobian trasnform matrix from cartesian to the warped cylindrical coordinates is needed.

Starting with the cartesian to cylindrical coordinate system transformation. This is dictated by Equation C.9.

$$
\begin{aligned}
x &= \rho \cos \theta \\
y &= \rho \sin \theta \\
z &= z
\end{aligned} \tag{C.9}
$$

Next, we define the warped cylindrical coordinates as Equation C.10

$$
\begin{aligned}
\rho' &= \left(\frac{b-a}{b} \right) \rho + a \\
\theta' &= \theta \\
z' &= z
\end{aligned} \tag{C.10}
$$

where $'$ denotes the new warped coordinate system. This leads to the final expressions describing the transform seen in Equation C.11.

$$x = (\rho' - a)\left(\frac{b}{b-a}\right)\cos\theta'$$

$$y = (\rho' - a)\left(\frac{b}{b-a}\right)\sin\theta'$$

$$z = z' \tag{C.11}$$

Using Equation C.11, the Jacobian transformation matrix is

$$J = \begin{vmatrix} \frac{\partial\rho'}{\partial x} & \frac{\partial\rho'}{\partial y} & \frac{\partial\rho'}{\partial z} \\ \frac{\partial\theta'}{\partial x} & \frac{\partial\theta'}{\partial y} & \frac{\partial\theta'}{\partial z} \\ \frac{\partial z'}{\partial x} & \frac{\partial z'}{\partial y} & \frac{\partial z'}{\partial z} \end{vmatrix} = \begin{vmatrix} \frac{b-a}{b}\cos\theta' & \frac{b-a}{b}\sin\theta' & 0 \\ -\frac{b-a}{b}\frac{\sin\theta'}{(\rho'-a)} & \frac{b-a}{b}\frac{\cos\theta'}{(\rho'-a)} & 0 \\ 0 & 0 & 1 \end{vmatrix} \tag{C.12}$$

and the inverse is

$$J^{-1} = \begin{vmatrix} \frac{\partial x}{\partial\rho'} & \frac{\partial x}{\partial\theta'} & \frac{\partial x}{\partial z'} \\ \frac{\partial y}{\partial\rho'} & \frac{\partial y}{\partial\theta'} & \frac{\partial y}{\partial z'} \\ \frac{\partial z}{\partial\rho'} & \frac{\partial z}{\partial\theta'} & \frac{\partial z}{\partial z'} \end{vmatrix} = \begin{vmatrix} \frac{b}{b-a}\cos\theta' & -(\rho'-a)\frac{b}{b-a}\sin\theta' & 0 \\ \frac{b}{b-a}\sin\theta' & (\rho'-a)\frac{b}{b-a}\cos\theta' & 0 \\ 0 & 0 & 1 \end{vmatrix}. \tag{C.13}$$

Next, the determinant can be seen in Equation C.14.

$$\left|J^{-1}\right| = \left(\frac{b}{b-a}\right)^2 (\rho' - a) \tag{C.14}$$

Using Equation C.8, the material parameter requirements are calculated in Equation C.15.

$$\left\{\begin{matrix} \epsilon' \\ \mu' \end{matrix}\right\} = \left|J^{-1}\right| J J^T \left\{\begin{matrix} \epsilon \\ \mu \end{matrix}\right\}$$

$$
\left\{ \begin{array}{c} \epsilon' \\ \mu' \end{array} \right\} = \left(\frac{b}{b-a} \right)^2 (\rho' - a) \begin{bmatrix} \frac{b-a}{b}\cos\theta' & \frac{b-a}{b}\sin\theta' & 0 \\ -\frac{b-a}{b}\frac{\sin\theta'}{(\rho'-a)} & \frac{b-a}{b}\frac{\cos\theta'}{(\rho'-a)} & 0 \\ 0 & 0 & 1 \end{bmatrix} \begin{bmatrix} \frac{b-a}{b}\cos\theta' & -\frac{b-a}{b}\frac{\sin\theta'}{(\rho'-a)} & 0 \\ \frac{b-a}{b}\sin\theta' & \frac{b-a}{b}\frac{\cos\theta'}{(\rho'-a)} & 0 \\ 0 & 0 & 1 \end{bmatrix} \left\{ \begin{array}{c} \epsilon \\ \mu \end{array} \right\}
$$

$$
\left\{ \begin{array}{c} \epsilon' \\ \mu' \end{array} \right\} = \begin{bmatrix} \rho'-a & 0 & 0 \\ 0 & \frac{1}{\rho'-a} & 0 \\ 0 & 0 & \left(\frac{b}{b-a}\right)^2 (\rho'-a) \end{bmatrix} \left\{ \begin{array}{c} \epsilon \\ \mu \end{array} \right\} \tag{C.15}
$$

Since, the coordinate transform assumes free space to begin with, ϵ_0, μ_0 take the form of the identity matrix in cartesian coordinates, but this is not the case in cylindrical coordinates. Using the same process as above, the cartesian to cylindrical transform can be applied to the free space parameters. The result is seen in Equation C.16.

$$
\left\{ \begin{array}{c} \epsilon_0^{cyl} \\ \mu_0^{cyl} \end{array} \right\} = \begin{bmatrix} \rho' & 0 & 0 \\ 0 & \frac{1}{\rho'} & 0 \\ 0 & 0 & \rho' \end{bmatrix} \tag{C.16}
$$

In order to keep an identity matrix formulation to express free space in cylindrical coordinates, a normalization term is applied to the relative material parameters as seen in Equation C.17.

$$
\left\{ \begin{array}{c} \epsilon' \\ \mu' \end{array} \right\} = \begin{bmatrix} \rho'-a & 0 & 0 \\ 0 & \frac{1}{\rho'-a} & 0 \\ 0 & 0 & \left(\frac{b}{b-a}\right)^2 (\rho'-a) \end{bmatrix} \begin{bmatrix} \frac{1}{\rho'} & 0 & 0 \\ 0 & \rho' & 0 \\ 0 & 0 & \frac{1}{\rho'} \end{bmatrix} \left\{ \begin{array}{c} \epsilon_0^{cyl} \\ \mu_0^{cyl} \end{array} \right\}
$$

$$
\left\{ \begin{array}{c} \epsilon_r' \\ \mu_r' \end{array} \right\} = \begin{bmatrix} \frac{\rho'-a}{\rho'} & 0 & 0 \\ 0 & \frac{\rho'}{\rho'-a} & 0 \\ 0 & 0 & \left(\frac{b}{b-a}\right)^2 \frac{(\rho'-a)}{\rho'} \end{bmatrix} \tag{C.17}
$$

The results are the material parameter requirements for a TO cloak as presented in [36] as seen below.

$$
\begin{aligned}
\mu_\rho, \epsilon_\rho &= \frac{\rho' - a}{\rho'} \\
\mu_\theta, \epsilon_\theta &= \frac{\rho'}{\rho' - a} \\
\mu_z, \epsilon_z &= \frac{\rho' - a}{\rho'} \left(\frac{b}{b - a} \right)^2
\end{aligned}
\tag{C.18}
$$

Bibliography

[1] Albertsen, N.C. "Creeping Wave Modes for a Dielectric Coated Cylinder". *IEEE Trans. Antennas Propag.*, 37(12):1642–1644, Dec 1989.

[2] Balanis, Constatine A. *Advanced Engineering Electromagnetics*. John Wiley & Sons, Inc, Hoboken, New Jersey, 1989.

[3] Chen, X, T.M. Grzegorczyk, and J.A. Kong. "Optimization approach to the retrieval of the constitutive parameters of a slab of general bianisotropic medium". *PIER*, 60(1-18), 2006.

[4] Chen, Xudong, Tomasz M. Grzegorczyk, Bae-Ian Wu, Joe Pacheco, and Jin Au Kong. "Robust method to retrieve the constitutive effective parameters of metamaterials". *Phys. Rev. E*, 70(1):016608, Jul 2004.

[5] Chew, Weng Cho. *Waves and Fields in Inhomogeneous Media*. Van Nostran Reinhold, New York, 1990.

[6] Collins, Peter and Jeffrey McGuirk. "A Novel Methodology for Deriving Improved Material Parameter Sets for Simplified Cylindrical Cloaks". *J Opt.*, 11(015104), 2009.

[7] Collins, Peter J. "EENG 725 Class Notes", 2009.

[8] Cummer, Steven A., Bogdan-Ioan Popa, David Schurig, David R. Smith, and John Pendry. "Full-wave simulations of electromagnetic cloaking structures". *Physical Review E (Statistical, Nonlinear, and Soft Matter Physics)*, 74(3):036621, 2006. URL http://link.aps.org/abstract/PRE/v74/e036621.

[9] Huang, Ying, Yijun Feng, and Tian Jiang. "Electromagnetic cloaking by layered structure of homogeneous isotropic materials". *Opt. Express*, 15(18):11133–11141, 2007. URL http://www.opticsexpress.org/abstract.cfm?URI=oe-15-18-11133.

[10] Kante, Boubacar, Dylan Germain, and Andre Lustrc. "Experimental demonstration of a nonmagnetic metamaterial cloak at microwave frequencies". *Physical Review B*, 80(201104(R)), 2009.

[11] Knott, E. F. *Radar Cross Section Measurements*. Scitech Publishing, Inc, Raleigh, North Carolina, 2006.

[12] Kock, W.E. "Metal-Lens Antennas". *Proceedings of the IRE*, 34(11):828–836, Nov. 1946. ISSN 0096-8390.

[13] Kodama, Masao. "Algorithm 912: A Module for Calculating Cylindrical Functions of Complex Order and Complex Argument". *ACM Trans. on Mathematical Software*, 37(4), Feb 2011.

[14] Li, Zhaofeng, Koray Aydin, and Ekmel Ozbay. "Determination of the Effective Constitutive Parameters of Bianisotropic Metamaterials from Reflection and Transmission Coefficients". *Phys. Rev. E*, 79(026610), Feb 2009.

[15] Liu, Ruopeng, Tie Jun Cui, Da Huang, Bo Zhao, and David R. Smith. "Description and Explanation of Electromagnetic Behaviors in Artificial Metamaterials Based on Effective Medium Theory". *Phys. Review E*, 76:206606, 2007.

[16] Markos, Peter and Costas Soukoulis. "Transmission properties and effective electromagnetic parameters of double negative metamaterials". *Opt. Express*, 11(7):649–661, 2003. URL http://www.opticsexpress.org/abstract.cfm?URI=oe-11-7-649.

[17] McGuirk, Jeffrey. *Electromagnetic Field Control and Optimization using Metamaterials*. (ADA506707). Air Force Institute of Technology(AU), Wright-Patterson AFB, OH, 2009.

[18] McGuirk, Jeffrey, Peter Collins, Michael Havrilla, and Aihua Wood. "A Green's Function Approach to Calculate Scattering Width for Cylindrical Cloaks". *Journal of the Applied Computational Electromagnetics Society*, 25(2), 2010.

[19] Naishadham, Krishna and Leopold Felsen. "Dispersion of Waves Guided Along a Cylindrical Substrate-Superstrate Layered Medium". *IEEE Trans. Antennas Propag.*, 41(3):304–313, Mar 1993.

[20] Nicolson, A. M. and G. F. Ross. "Measurement of the Intrinsic Properties of Materials by Time-Domain Techniques". *Instrumentation and Measurement, IEEE Transactions on*, 19(4):377–382, Nov. 1970. ISSN 0018-9456.

[21] Paknys, Robert. "Evaluation of Hankel Functions with Complex Argument and Complex Order". *IEEE Trans. Antennas Propag.*, 40(5):569–578, May 1992.

[22] Paknys, Robert and David R. Jackson. "The Relation Between Creeping Waves, Leaky Waves, and Surface Waves". *IEEE Trans. Antennas Propag.*, 53(3):898–907, Mar 2005.

[23] Paknys, Robert and Nan Wang. "Creeping Wave Propagation Constants and Modal Impedance for a Dielectric Coated Cylinder". *IEEE Trans. Antennas Propag.*, 34(5):674–680, Dec 1986.

[24] Paknys, Robert and Nan Wang. "Excitation of Creeping Waves on a Circular Cylinder with a Thick Dielectric Coating". *IEEE Trans. Antennas Propag.*, 35(12):1487–1489, Dec 1987.

[25] Paul, Jason V., Peter J. Collins, and Ronald A. Coutu Jr. "A New Look at Azimuthal Wave Propagation Constants of an n-Layered Dielectric Coated PEC Cylinder". *IEEE Trans. Antennas Propag.*, 61(5), 2013.

[26] Pendry, A.J.; Robbins D.J.; Stewart W.J., J.B.; Holden. "Magnetism from conductors and enhanced nonlinear phenomena". *Microwave Theory and Techniques, IEEE Transactions on*, 47(11):2075–2084, Nov 1999. ISSN 0018-9480.

[27] Pendry, J. B., A. J. Holden, W. J. Stewart, and I. Youngs. "Extremely Low Frequency Plasmons in Metallic Mesostructures". *Phys. Rev. Lett.*, 76(25):4773–4776, Jun 1996.

[28] Pendry, J.B., D. Schurig, and D.R. Smith. "Controlling electromagnetic fields". *Science*, 312(5781):1780–1782, 2006. URL http://www.sciencemag.org/cgi/content/abstract/312/5781/1780.

[29] Popa, Bogdan-Ioan and Steven A. Cummer. "Cloaking with Optimized Homogeneous Anisotropic Layers". *Physical Review A*, 79(023806), 2009.

[30] Post, E. J. *Formal Structure of Electromagnetics*. North-Holland Publishing Co, Amsterdam, 1962.

[31] Qiu, Cheng-Wei, Li Hu, Xu Xiaofei, and Yijun Feng. "Speherical cloaking with homogeneous isotropic multilayered strucutures". *Physical Review E*, 79(047602), 2009.

[32] Qui, C. W., L. Hu, and S. Zouhdi. "Isotropic non-ideal cloaks providing improved invisibility by adaptive segmentation and optimal refractive index profile from ordering isotropic materials". *Optics Express*, 18(14):14950–14959, 2010.

[33] Rahm, M., D. Schurig, D. A. Roberts, S.A. Cummer, D. R. Smith, and J. B. Pendry. "Design of electromagnetic cloaks and concentrators using form-invariant

coordinate transformations of Maxwell's equations". *Photonics and Nanostructures: Fundamentals and Applications*, 2007.

[34] Rotman, W. "Plasma simulation by artificial dielectrics and parallel-plate media". *Antennas and Propagation, IEEE Transactions on [legacy, pre - 1988]*, 10(1):82–95, Jan 1962. ISSN 0096-1973.

[35] Ruan, Zhichao, Min Yan, Curtis W. Neff, and Min Qiu. "Ideal Cylindrical Cloak: Perfect but Sensitive to Tiny Perturbations". *Physical Review Letters*, 99(11):113903, 2007. URL http://link.aps.org/abstract/PRL/v99/e113903.

[36] Schurig, D., J. J. Mock, B. J. Justice, S. A. Cummer, J. B. Pendry, A. F. Starr, and D. R. Smith. "Metamaterial Electromagnetic Cloak at Microwave Frequencies". *Science*, 314(5801):977–980, 2006. URL http://www.sciencemag.org/cgi/content/abstract/314/5801/977.

[37] Schurig, D., J. J. Mock, and D. R. Smith. "Electric-field-coupled Resonators for Negative Permittivity Metamaterials". *Appl. Phys. Lett.*, 88(041109).

[38] Schurig, D., J. B. Pendry, and D. R. Smith. "Calculation of material properties and ray tracing in transformation media". *Optics Express*, 14(21):9794–9804, 2006. URL http://www.opticsexpress.org/abstract.cfm?URI=oe-14-21-9794.

[39] Simovski, C. R. "On Electromagnetic Characterization and Homogenization of Nanostructured Metamaterials". *J Opt.*, 13(013001), 2011.

[40] Simovski, Sergei A., Constantin R.and Tretyakov. "Local Constitutive Parameters of Metamaterials from an Effectiv-Medium Perspective". *Phys. Review B*, 75:19511, 2007.

[41] Smith, D. R., S. Schultz, P. Markoš, and C. M. Soukoulis. "Determination of effective permittivity and permeability of metamaterials from reflection and transmission coefficients". *Phys. Rev. B*, 65(19):195104, Apr 2002.

[42] Stratton, Julius Adams. *Electromagnetic Theory*. McGraw-Hill, New York and London, 1941.

[43] Sun, Jin and Le-Wei Li. "Dispersion of Waves Over a PEC Cylinder Coated With Two-Layer Lossy Dielectric Materials". *IEEE Trans. Antennas Propag.*, 55(3):877–881, Mar 2007.

[44] Sun, Jin, Chao-Fu Wang, Le Wei Li, and Mook-Seng Leong. "Creeping Waves Along a Perfectly Conducting Cylinder with a Lossy Magnetic Coating". *IEEE Trans. Antennas Propag. Ltrs*, 2, 2003.

[45] Szabo, Zsolt, Gi-Ho Park, Ravi Hedge, and Er-Ping Li. "A Unique Extraction of Metamaterial Parameters Based on Kramers-Kronig Relationship". *IEEE Trans. Microw. Theory Tech.*, 58(10):2646–2653, Oct 2010.

[46] Tie Jun Cui, Ruopeng Liu, David R. Smith. *Metmaterials Theory, Design and Applications*. Springer, New York, Dordrecht, Heidelberg, London, 2009.

[47] Wang, Nan. "Electromagnetic Scattering From a Dielectric Coated Circular Cylinder". *IEEE Trans. Antennas Propag.*, 33(9):960–963, Sep 1985.

[48] Ward, A.J. and J.B. Pendry. "Refraction and geometry in Maxwell's Equations". *Journal of Modern Optics*, 43(4):773–793, 1996. URL http://www.informaworld.com/10.1080/09500349608232782.

[49] Weir, W.B. "Automatic measurement of complex dielectric constant and permeability at microwave frequencies". *Proceedings of the IEEE*, 62(1):33–36, Jan. 1974. ISSN 0018-9219.

[50] Wood, B., J. B. Pendry, and D. P. Tsai. "Directed subwavelength imaging using a layered metal-dielectric system". *Physical Review B (Condensed Matter and Materials Physics)*, 74(11):115116, 2006. URL http://link.aps.org/abstract/PRB/v74/e115116.

[51] Xi, Sheng, Hongshen Chen, Baile Zhang, Bae-Ian Wu, and Jin Au Kong. "Route to low-scattering cylindrical cloaks with finite permittivity and permeability". *Physical Review B*, 79(155122), 2009.

[52] Yan, Min, Zhichao Ruan, and Min Qiu. "Cylindrical Invisibility Cloak with Simplified Material Parameters is Inherently Visible". *Physical Review Letters*, 99(23):233901, 2007. URL http://link.aps.org/abstract/PRL/v99/e233901.

[53] Yan, Min, Zhichao Ruan, and Min Qiu. "Scattering characteristics of simplified cylindrical invisibility cloaks". *Opt. Express*, 15(26):17772–17782, 2007. URL http://www.opticsexpress.org/abstract.cfm?URI=oe-15-26-17772.

[54] Zhenzhong, Yu, Yijun Feng, Xiaofei Xu, Jumming Zhao, and Tian Jiang. "Optimized Cylindrical Invisibility Cloak with Minimum Layers of Non-Magnetic Isotropic Materials". *J. Phys. D. Appl. Phys*, 44(185102), 2011.

1. REPORT DATE *(DD–MM–YYYY)*	2. REPORT TYPE	3. DATES COVERED *(From — To)*
21–03–2013	Doctoral Dissertation	Oct 2009–Mar 2013

4. TITLE AND SUBTITLE

Metamaterial Structure Design Optimization: A Study of the Cylindrical Cloak

5a. CONTRACT NUMBER

5b. GRANT NUMBER

5c. PROGRAM ELEMENT NUMBER

6. AUTHOR(S)

Paul, Jason V., Maj, USAF

5d. PROJECT NUMBER

5e. TASK NUMBER

5f. WORK UNIT NUMBER

7. PERFORMING ORGANIZATION NAME(S) AND ADDRESS(ES)

Air Force Institute of Technology
Graduate School of Engineering and Management (AFIT/EN)
2950 Hobson Way
WPAFB, OH 45433-7765

8. PERFORMING ORGANIZATION REPORT NUMBER

AFIT-ENG-DS-13-M-04

9. SPONSORING / MONITORING AGENCY NAME(S) AND ADDRESS(ES)

David J. Winebrener,LtCol,USAF
National RCS Test Facility
871 DeZonia Road
Holloman AFB NM 88330
575-679-3323, David.Winebrener@holloman.af.mil

10. SPONSOR/MONITOR'S ACRONYM(S)

11. SPONSOR/MONITOR'S REPORT NUMBER(S)

12. DISTRIBUTION / AVAILABILITY STATEMENT

DISTRIBUTION STATEMENT A:
APPROVED FOR PUBLIC RELEASE; DISTRIBUTION UNLIMITED

13. SUPPLEMENTARY NOTES

This work is declared a work of the U.S. Government and is not subject to copyright protection in the United States.

14. ABSTRACT

Previously, Transformational Optics (TO) has been used as a foundation for designing cylindrical cloaks. The TO method uses a coordinate transform to dictate an anisotropic material parameter gradient in a cylinder coating that guides waves around the cylinder to reduce the Radar Cross Section (RCS). The problem is that the material parameters required for the TO cloak are not physically realizable and thus must be approximated. This problem is compounded by the fact that any approximation deviates from the ideal design and will allow fields to penetrate the cloak layer and interact with the object to be cloaked. Since the TO method does not account for this interaction, approximating the ideal TO parameters is doomed to suboptimal results.
However, through the use of a Green's function, an optimized isotropic cloaked cylinder can be designed in which all of the physics are accounted for. If the contribution due to the scatterer is 0, then the observer, regardless of position, will only observe the contribution due to the source and thus the object is cloaked from observation. The contribution due to the scatterer is then used as a cost functional with an optimization algorithm to find the optimal parameters of an isotropic cloaked cylinder. Although the material parameters in this design method can be fulfilled by any material, metamaterials are used to study their viability and assumptions in this application. This process culminates in the design, fabrication and measurements of a cloaked cylinder made of metamaterials that operate outside of their resonant bands. We show bistatic RCS reduction for nearly every angle along with monostatic RCS reduction for nearly every frequency in the range of 5GHz-15GHz. Most importantly, the experimental results validate the use of a Green's function based design approach and the implementation of metamaterials for normally incident energy.

15. SUBJECT TERMS

Metamaterial, Cloak, RCS Reduction

16. SECURITY CLASSIFICATION OF:			17. LIMITATION OF ABSTRACT	18. NUMBER OF PAGES	19a. NAME OF RESPONSIBLE PERSON
a. REPORT	b. ABSTRACT	c. THIS PAGE			Dr. Peter Collins, AFIT/ENG
U	U	U	UU	154	19b. TELEPHONE NUMBER *(include area code)* (937) 255-3636 ext. 7256